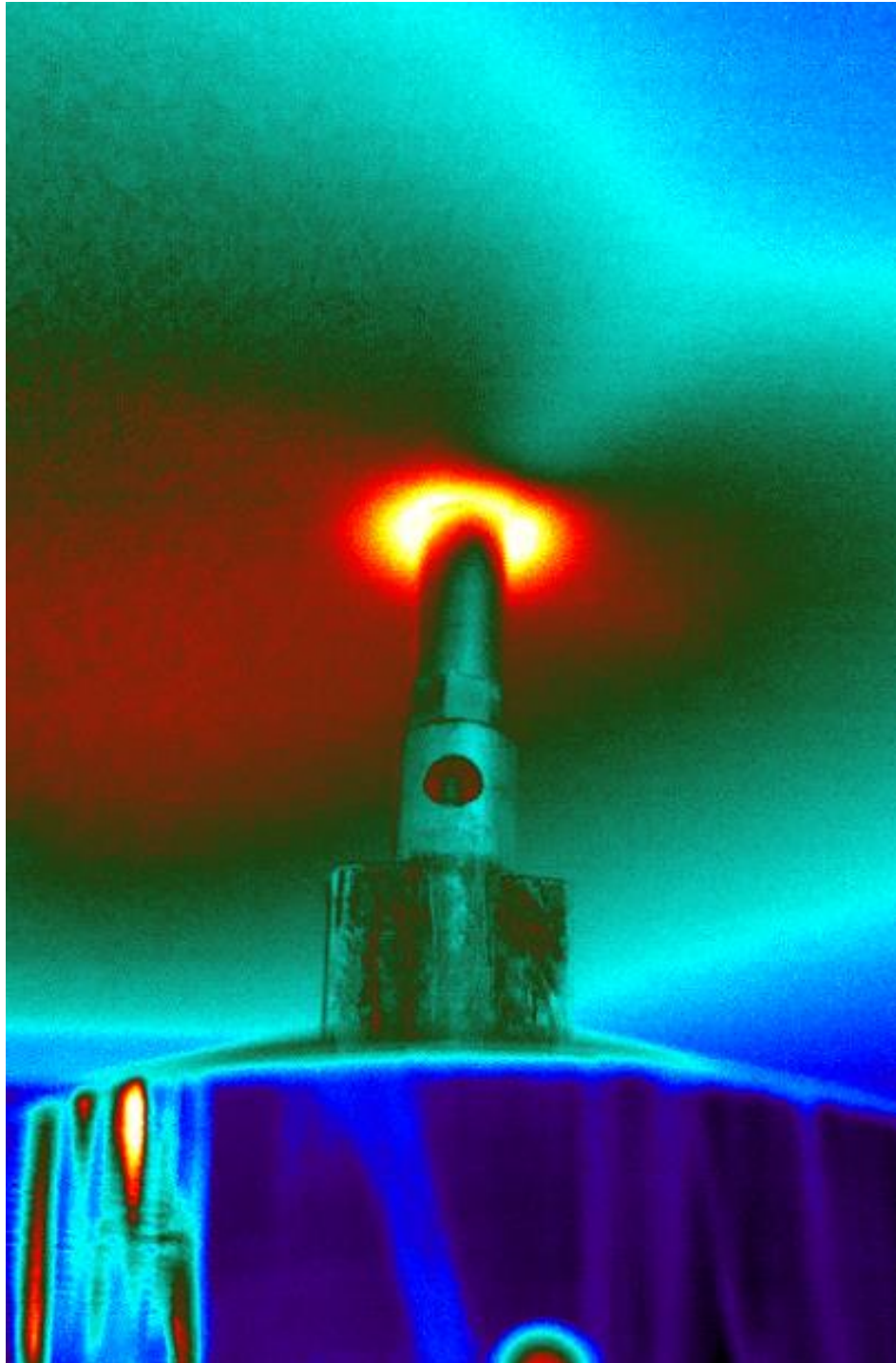H.J. den Ouden

Investigating Planar Delamination Behavior in Carbon Fiber Reinforced Polymer Panels

An evaluation of delamination criteria

TUDelft

Investigating Planar Delamination Behavior in Carbon Fiber Reinforced Polymer Panels

An evaluation of delamination criteria

By

H.J. den Ouden

in partial fulfilment of the requirements for the degree of

Master of Science
in Aerospace Engineering

at the Delft University of Technology,
to be defended publicly on Friday 24th of July 2020 at 9:30 AM.

Supervisor:	Dr. Ir. R.C. Alderliesten	
Thesis committee:	Dr. Ir. J.A. Pascoe,	TU Delft
	Dr. Ir. F.P. van der Meer,	TU Delft
	Msc. N.K. Karna,	TU Delft

An electronic version of this thesis is available at http://repository.tudelft.nl/.

TUDelft

ABSTRACT

The relation between planar delamination growth, induced by transverse quasi-static load case, and the coupon delamination validation tests was investigated by evaluating the delamination criteria. The delamination criterion that allowed to describe planar delamination growth was the strain energy density criterion. An analytical study was performed to relate the elliptical delamination growth in planar delamination growth with the material properties through the strain energy density criterion. Following to this study, an experimental setup was designed to measure the delamination boundary during the transverse load induction of a planar specimen. With this new experimental setup both quasi-static and fatigue tests were performed with quasi-isotropic planar specimen which have artificial delaminations. For the fatigue tests that were performed on this experimental setup, a methodology was proposed on determining the strain energy release rate. The outcomes of the quasi static tests were then compared with a numerical model based on mode-partitioning virtual crack closure technique. All the different studies demonstrated that the physical strain energy release rate was the metric to asses the delamination behavior in a planar fatigue experiment. The delamination criterion that was applicable for planar delamination problems is the strain energy density criterion which measured and predicted the delamination size.

ACKNOWLEDGMENTS

Nomenclature

u In-plane Displacement x-direction [m]

v In-plane Displacement y-direction [m]

w Out-of-plane Displacement [m]

w_0 Center Out-of-Plane Displacement [m]

ε_i In-plane strain [-/-]

κ_i Bending Curvature [-/-]

σ_i Stress [Pa]

$G_{I,II}$ Strain Energy Release Rate for delamination mode I and II [J/m^2]

E_i Young's Modulus [Pa]

G_{ij} Shear Modulus [Pa]

ν Poisson's Ratio [-/-]

r_e Radius of the Ellipse [m]

r_c Radius of the clamp [m]

θ Angle orientation ellipse from center [rad]

K_i Stress Intensity Factor for delamination mode I,II or III [-]

M Mode Mixity factor of delamination mode I and II [-]

ϕ Mode mixity angle of delamination mode I and II [rad]

U Strain Energy [J]

W Applied Work [J]

Π Potential Energy [J]

u_ρ Strain Energy Density [J/m^3]

CONTENTS

LIST OF FIGURES

LIST OF TABLES

1

INTRODUCTION

Every year composite structures are more applied in mobility products [16] due to their lightweight properties while retaining structural integrity. A greater number of civilians will use a mode of transport that uses composites, making it more relevant to improve the understanding of damage tolerance assessment. Due to the poor interlaminar strength of composite materials [17], the most common damage that causes failure within structural composites is delamination [18]. Delaminations can be induced in a structure in different manners like impact damage, manufacturing defects, or straight edges[17]. The current standards measure the SERR of the independent delamination modes to characterize the delamination resistance of Fiber Reinforced Polymer (FRP). The delamination modes (figure 1.1) for which the standards describe the measurement for mode I [1, 19], mode II [20, 21], and mixed-mode I/II delamination resistance [2]. All the standard test methods characterize the delamination resistance of the unidirectional coupon specimen. The benefits of using a unidirectional coupon specimen are that tests are easily measurable, since the delamination propagates in a single direction, and the delamination propagates with a clean fracture surface. Issues arise when the delamination resistance of more complicated structures is characterized. To gain more insight into more complicated delamination behavior, researchers create experiments that test semi-complex structures and layups. An example of such an experiment would be the transverse out-of-plane load opening experiment in which a Glass Fiber Reinforced Polymer (GFRP) plate structure with a central delamination is separated by an out-of-plane load [6] to estimate how the delamination resistance differs in a structure without free edges.

This research aims to investigate how the delamination can be measured in a CFRP plate, to iterate on the previous plate structure investigation[6]. The difficulty of measuring the delamination in a CFRP planar test specimen is that the delamination growth is not visible to the naked eye. Innovative tools and methods are required that can measure the delamination growth in the process. Such tools might already exist like the lock-in thermography method, which has been applied to measure delamination growth in CFRP composites in a Charpy impact test [22]. The delamination growth can also be measured by tracking a delamination
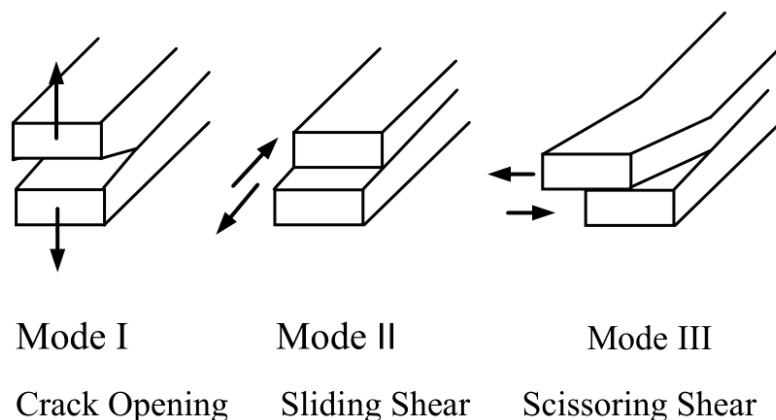
Figure 1.1: The three various delamination modes

criterion in the experiment. A suitable delamination criterion that can be measured in the planar delamination is the SED criterion. The SED of a material requires insights into the constitutive properties and the strains of the specimen. The strains of specimen while being tested can be measured with DIC.

The SED criterion recently received renewed interest by Amaral and Daneshjoo [3, 23] as a methodology to explain the differences between the onset SERR's of different loading modes. The SED criterion is the principle that there is a critical amount of energy required at the delamination front for propagation. The researchers have tested this criterion with specimens of all the different delamination resistance characterization tests [1, 2, 20]. The result of their experiment is that the SED criterion could explain the relationship between the mode I and mode II fracture toughness of FRP specimen. Since the critical SED is not dependent on the loading condition, it should be a material property that is the same for coupon and planar test specimens.

1.1. GOAL OF THIS WORK

This research investigated the methods to measure planar delamination growth in CFRP plates. The methods that have been investigated to measure planar delamination growth are lock-in thermography and bond state mapping through the SED criterion measured with DIC. The bond state mapping method did require more insight since this was a newly developed method. First knowledge was created on how the SED behaves during planar crack growth by simulating the transverse load opening experiment [6]. These simulations demonstrated how the SED balances during delamination growth, allowing for stable propagation. The result delamination shapes of the models did match the experiment. The experiment was designed and performed to measure both the heat and strains on the surface of the CFRP plate specimens. The quasi-static experiments experienced limited delamination but did demonstrate the repeatability of the experimental setup. The fatigue experiments did experience planar delamination, for which an analyzing methodology was developed. The methodology applies the physical SERR to retrieve a quantitative insight into the delamination resistance of the CFRP plate throughout the fatigue experiment. The last study of the research is to test the applicability of the SERR mode partitioning criterion (B-K law) for planar delamination problems.

2

LITERATURE STUDY

2.1. INTRODUCTION

This literature study gives an overview of the current state of the art of delamination test methods. Current test methods for measure delamination behavior in a single direction and are limited to a specific size. These limitations were described in the currently standardized methods, which is the initial focus of the literature review. These test methods were developed through a fracture mechanics framework, which is the second part the literature review initially investigates. The current test methods fix independent variables to vary a limited number of dependent variables. The influence of the dependent variables was investigated. Lastly the experiment is limited by the available measurement methods. In the last part of the literature study the limitations that these available measurement methods bear was investigated.

2.2. FIELDS OF INTEREST

The main fields of interest that explore planar delamination are low-velocity impact studies, buckling delamination studies, and composite sandwich disbond studies. These study fields have their individual methods of describing planar delamination behavior and their own set of assumptions. This subsection explores these assumptions and current developments.

2.2.1. LOW-VELOCITY IMPACT DELAMINATION

One of the earliest experimental studies that investigated the relation between delamination shapes and the impact load, measured both with peak load and impact energy, was by Lagace and Williamson[24]. Lagace and Williamson determined that the peak load and indent velocity are directly related to one other. Lagrace and Williamson's study also demonstrated similarity between the planar delamination behavior of quasi-static indentation tests and impact tests. The subsequent developments on the experimental impact studies to capture delamination behavior were by Davies and Zang [9, 25], who performed an initial numerical study and experimental study to measure the threshold damage criterion of low-velocity impact tests. Based on the experiment, Davies and Zang simplified the problem by assuming circular delamination shapes upon impact. Davies and Zang then identified a critical onset load for impact based on the SERR, assuming that circular delamination is opened by a pure shear load [9]. To test the numerical outcomes by Davies [25], Schoeppner [26] setup an experiment to derive the threshold load for impact delamination and discovered that the delamination behavior of low velocity impact tests is similar to that of indentation tests. Schoeppner also demonstrates in the study that the circular approximation for the delamination shape is not satisfactory. The next major experimental work that is used for numerical studies is Aymerich's ultra-sonic scans after impact [27]. The C-scans demonstrate the final state of the material after the load is induced. However, it did not deliver insight regarding the delamination process. Meola et al's [22] approach to impact tests investigated the energy dissipation in four different composite materials (two thermoset and two thermoplastic) through thermographic measurements. The research demonstrated the tortuous paths that delamination travels through when impact occurs. These tortuous paths are the path of least resistance. In recent works [28] it has been possible to capture delamination behavior with a Proper Generalized Decomposition (PGD) model of planar delamination induced by low-velocity impact. The study applies a set of boundary value problems to a numerical model which iterated to a singular solution. The study applies a mode-mixed critical SERR measured

through a power-law to determine the delamination onset growth. The simulation is then compared to the results given by Aymerich's experiment [27]. The critical SERR, in the PGD study, was determined through the DCB and End Notch Flexure (ENF) Test. The mode III critical SERR was assumed to be equal to the mode II SERR, which demonstrates how the current SERR criterion is applied with intuition. Concluding to their work Aymerich, Davies and Zang assume self-similar growth of circular delaminations in orthotropic laminates.

2.2.2. Buckling Delamination

The first analytical research on buckling planar delamination studies was performed Chai et al.[29]. Chai's study delivers an extensive analytical investigation on how delamination onset and growth would behave when a buckling load is applied. Chai proposed the delamination growth criterion to be the SERR of the material, which is measured with the DCB test. To determine the growth paths of the delamination, Chai assumes that the material will deliver the greatest resistance possible to delaminations. The greatest resistance assumption, in combination with planar growth, implies that the SERR at the boundary of the delamination will be homogeneous. To achieve equal SERR at the delamination border, the delamination is bound to become elliptical. This elliptical delamination shape will be in equilibrium once the SERR is homogeneous at the delamination boundary, which means that the elliptical shape will grow in a self-similar manner.

Subsequent studies elaborate on this SERR approach, decoupling the critical SERR with separate delamination modes. Storaker et al.'s investigation [30] assumes that different delamination modes act independently of one other. Yin and Jane's [31, 32] study explored planar delamination growth by developing an analytical model that describes the relation between the point-wise SERR and buckling delamination load. This study stated that the buckling delamination is greatly influenced by transverse shear behavior, which behavior is included in present numerical studies. The quasi-brittle fracture behavior, with a maximum SERR, is still applied in current numerical and analytical buckling delamination studies.

The research by Koellner [33] determined the onset point from which delamination grows. An analytical boundary condition problem is solved with classic laminate theory, allowing the delamination to grow only in a single direction at a time. In Wang's study [34] elliptical delamination can grow in both the longitudinal and transversal directions subsequently. The delamination behavior in Wang's study is governed by a mixed-mode SERR delamination criterion. The mode-mixity parameter is fitted to experimental data, which was not further elaborated upon in this study. Wang's study showed the relation between the criterion and the delamination growth in a quasi-static test.

2.2.3. Composite Sandwich Face Disbonds

Disbonds in composite sandwich structures is one of the primary reasons that stopped the development of Lockheed Martin's VentureStar program. The structural failure was disbonds in the cryogenic fuel tank that started to leak due to disbonds in the X33-program [35]. To gain a better understanding of delamination problem, NASA was performed multiple studies to investigate the planar delamination in Sandwich panel[36, 37]. Both Chen and Rinker developed numerical studies that estimate the delamination effects based on the damage reports of the VentureStar pressure tank. Due to the pressurization in the studies, the SERR at the crack growth does not remain constant. Calculating the delamination behavior of curved panels with a fixed SERR would not capture the delamination behavior accurately.

To further investigate why the SERR does not remain constant in a planar test Cameselle-Molares developed an experimental studies [6, 38, 39] and numerical [40, 41] studies. The outcome of the complete set of work is that planar delamination is influenced by an increasing fracture process zone. The resulting proposal from this study is to calculate a planar SERR value through numerical simulation based on the experimental outcomes. From this numerical simulation, a linear scaling law can be identified to find the planar SERR value with the measured load-displacement slopes.

2.3. Test Standards

For either Mode I delamination [1, 19] , Mode II delamination [20, 21] and Mixed Mode (I/II) delamination [2] ASTM and ISO have created test methods to derive useful engineering parameters. While these tests standards give insight in delamination resistance, the standards also describe the limitation of the applicability of the test.
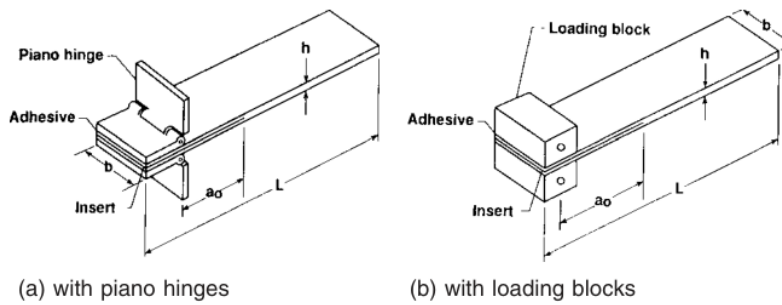
Figure 2.1: Schematic of DCB test [1]

2.3.1. MODE I DELAMINATION: DOUBLE CANTILEVER BEAM

The current standardized method for the measurement of mode I delamination behavior is the DCB test. A standard set up of such a test is given in figure 2.1. A slender beam with a pre-crack is loaded on its edges with an out-of-plane load. When the beam is loaded it will split, and the double cantilever shape appears. This splitting is the crack extension which occurs in a stable manner. With the derivation of the energy required for splitting and the measured crack extension surface, the SERR, of the mode I delamination, can easily be derived. While the DCB test does give a comprehensive method for determining the delamination behavior of a beam, it does have its limits. The current method only works for linear deformation. This limits the specimen size. The current standard can only test 0° unidirectional plies. At the 0//0 interface more extreme fiber bridging occurs which clutters the measured SERR. This layup limitation is set in in-place to prevent anticlastic bending effects and nonuniform delamination growth in the test specimen.

2.3.2. MODE II DELAMINATION: END-NOTCHED FLEXURE AND END LOADED SPLIT

The current standardized method for the measurement of mode II delamination behavior is the ENF test for American Society for Testing and Materials (ASTM) while for International Organization for Standardization (ISO) this is the End Loaded Split ELS test.

A standard set up of for the ENF test is given in figure 2.2a. The process allows for an isolated insight into the mode II delamination behavior of a composite material. A slender beam with a pre-crack, at an end of the beam, is loaded into a three-point bending test. When the beam is loaded, the bending of the beam will cause a stress difference between the top part of the beam and the bottom part of the beam. This will result into a shear load, that causes an extension of the pre-crack in a stable manner. With the derivation of the energy required, by the load induction, for splitting and the measured crack extension surface, the SERR of the mode II delamination can easily be derived. The standard set up for the ELS test is given in figure 2.2b.

(a) The ENF Test Fixture and Specimen Nomenclature [20]

(b) ELS Test Fixture and Specimen [42]
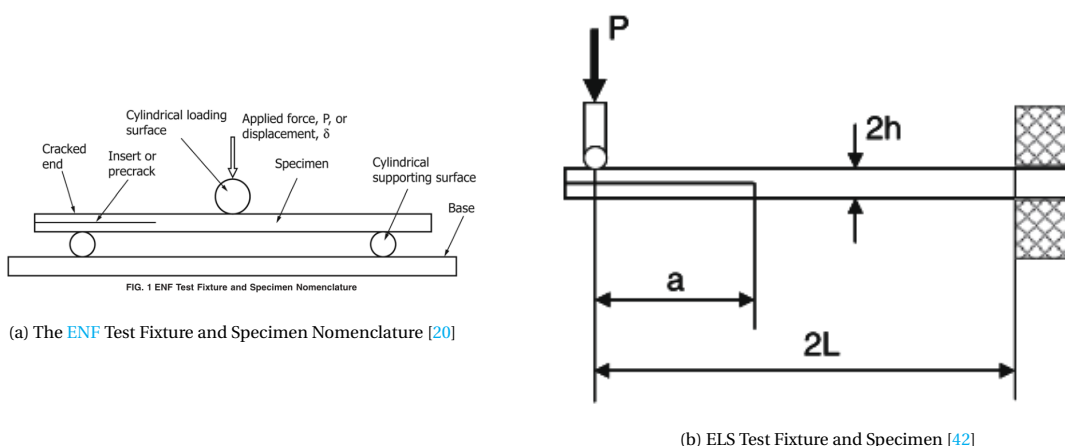
Figure 2.2: Mode II standard test methods

The process is a clamped in specimen that is pressed on its outer edge. This pressing induces a bending load, which will induce a shear load at the pre-crack layer.Since the specimen is fixed in this method, measuring
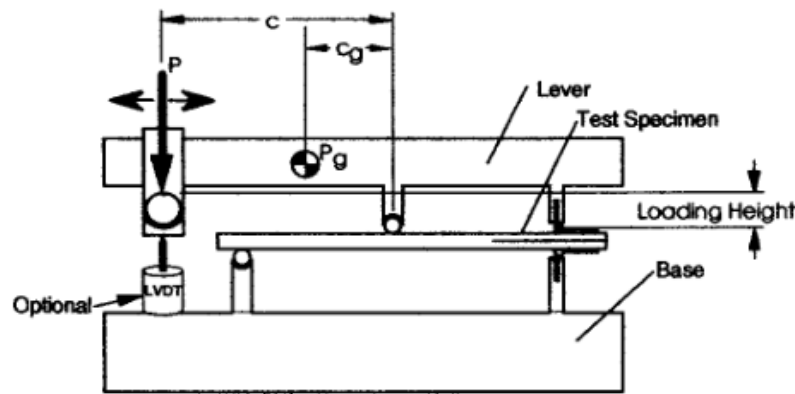
Figure 2.3: The Mixed Mode Bending apparatus [2]

the crack expansion when loading the specimen is comparatively easier than the ENF test. The ENF and the ELS test have limitations for describing the delamination behavior of a composite material. Either test is developed for linear elastic behavior, which limit the test for large deformations. This also means that very tough composites should be avoided when applying these tests. Lastly, the current Mode II tests solely describes the toughness of 0//0 interfaces, while the value does differ for other layups.

2.3.3. MIXED MODE DELAMINATION (I/II): MIXED-MODE BENDING

For the understanding of mode mixing during delamination, MMB is the standard. A standard set up of this test is given in figure 2.3. The process of the MMB test is like a combination of the DCB test with the ENF test. A slender beam with a pre-crack, at an end of the beam, is loaded into a three point bending test while being pulled apart. This combination of loads is achieved with a cantilever beam that presses at the center of the beam, while opening the end of the beam. This means the mode I behavior is defined by the distance of the beam lever, to the center of gravity, while the mode II behavior is defined by the sum of loads. This allows a determination of mixed-mode delamination behavior through a linear elastic model. Since linear deformation theory is applied, only small deformations can be tested. This limits the test to thin beams with weak interfaces.

It can be noted that the current testing methods do mainly have issues with either thicker laminates, that are applied in practice. The test is not suitable for multidirectional laminates.

2.3.4. DISCUSSION STANDARDS

The primary discussion of the current test standards is the determination of the onset SERR of the mode II delamination test [17], which is greater than the mode I onset SERR. O'Brien et al. discovered during the study that in fatigue load cases, the onset SERR of a mode II specimen will transform into a cyclic SERR similar to the mode I SERR at a large number of cycles. O'Brien mentioned that this could be due to the initial onset sensitivities, like the matrix stiffness, meaning that the current SERR method is a conservative estimation of the delamination behavior. To quantify why this change of delamination resistance occurs in a fatigue test, Amaral et al. [3] performed a set of MMB tests to test a criterion that is independent of the mode-mixity. This criterion is the SED criterion [43] which is energy required at a crack front to propagate the delamination. Amaral et al. [10] also created an experiment to measure the developments at the crack front in a mode II test. The outcome of this experiment is that in mode II loading not all energy was dissipated to the crack front. Instead some energy dissipated into cusp forming beyond the crack front, see figure 2.4.

2.4. FRACTURE MECHANICS APPROACHES

All the present standards are based on a fracture mechanics approach, which in turn deliver on a criterion that can estimate the delamination resistance of a laminate. The reason for the application of these methods is because of their theoretical background that can be combined with empirical test methods. Since any experimental method should be in line with a supporting theoretical framework, the main fracture mechanic frameworks are investigated. The various fracture criteria which are the commonly used SERR, the SIF and the SED were explored. All these criteria are related but approach the delamination problem differently.
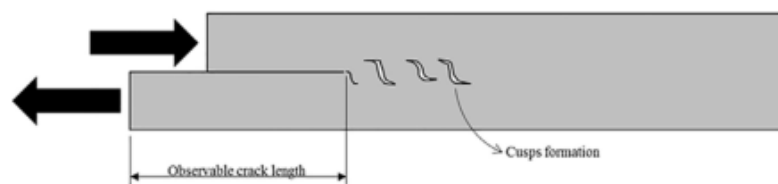
Figure 2.4: Cusps Formation in Foam [3]

2.4.1. Strain Energy Release Rate (SERR)

The first mention of SERR that limits the crack growth behavior is described by Griffith's theory [44]. In Griffith's Fracture theory it is mentioned that the potential energy exists out of the induced strain energy and the available energy applied by the forces. This "energy applied by the forces in the material" are the described delamination forces which in turn gives the SERR. In his works Griffith measured the delamination of isotropic solids, both brittle materials (thin Hard English glass plate and glass fibers) and ductile materials (various metals),through a hydro-static load that was slowly increased. After Griffith more advanced methods have been developed to describe the delamination behavior. The current standards of the double cantilever beam, the ENF and the mixed-mode bending tests are described in chapter 2.3, since these are the current test methods.

2.4.2. Stress Intensity Factor (SIF)

The first method that aimed to explain crack growth behavior was developed by Irwin [45]. The reason that Irwin described the sharp notch crack behavior, is since the methods at that time mainly could describe blunt notch problems. The blunt notch model would give infinite stresses at sharp corners, which is not a realistic description. Based on Griffith's SERR model, the stress behavior could be captured for either plane-stress and plane-strain behavior. The method made by Irwin describes the plane strain stress distributions in an isotropic material, based on the induced crack loading mode. When a certain maximum stress is developed through the crack itself, brittle failure will occur in the material. The stress intensity factor theory was further expanded by Sih [43] for orthotropic materials. This model allows the SIF method to be applied for composite materials. This is also the first time that the loading modes were separated and that influence of mode-mixity is mentioned. The method given in either Irwin's and Sih's work are simply measured with the application of strain gauges. A strain map was developed through which insights were provided on the crack growth. The limitations of this method is that it solely focuses on crack growth in a brittle plastic manner through a solid. This does not accurately portray the interlaminar delamination behavior of a composite, which is why the current standard is described with the SERR.

2.4.3. Strain Energy Density (SED)

As mentioned by Pascoe [46], the current methods for fatigue delamination are not focused on the further understanding the physics of the problem and instead extend existing empirical calculation methods with more experimental data. To gain new insights on fatigue delamination Amaral [3] and Daneshjoo [23] have been working with the SED fracture mechanics application. The method defines that the crack will extend when a certain critical energy is reached at the crack front instead of a general critical SERR. To define the further development of the crack path, the method describes the stresses at the crack tip with functions defined by Sih [43]. The product of these stresses with its strains at the crack tip defines the SED field at the tip. The SED is negative counterpart of the potential energy. The maximum potential energy defines the direction of crack development. This implies that the crack path is also determined by minimum SED. This research described the difference in critical SERR between mode I and mode II loads, which correlates with the fatigue behavior measured by O'Brien [17]. The major benefit of the SED approach compared to the mixed-mode SERR approach is that the SED depends on the current energetic state of the material while the mixed-mode SERR approach depends on the change of energetic states. While the method does explain the current behaviors of the separated standardized delamination tests, it still has complications to describe the mode mixity of the delamination problem in a proper manner.

2.4.4. Mode mixity

In the test methods it is possible to isolate the problem to a single mode of delamination. Most load cases applied to composite structures cause a mix of the delamination modes. To give insight in the manner that mode-mixity occur in the material, it is important to highlight the two most important parameters to describe mode-mixity. These are for the induced load (the phase angle) and the resulting SERR modes (Mixed Mode Ratio) which are described as following:

Phase Angle

The phase angle describes the relation of the mixed-mode loading's, this gives insights regarding the experimental setup.

$$\phi = \arctan\left(\frac{K_{II}}{K_I}\right) \tag{2.1}$$

Where K_i describes the separated induced delamination mode load. It is common practice to vary the phase angle within an experimental setup to see the orientation dependent load response of a material. **Mixed Mode Ratio**

To describe how the resulting SERRs mix resulting from a delamination test it is a common method to apply a mixed mode ratio. The equation for the mixed mode is given as following:

$$M = \frac{G_{II}}{G} = \frac{G_{II}}{G_I + G_{II}} \tag{2.2}$$

Where G_i describes the individual mode SERR's. The mixed mode ratio is a linear scaling function between the mode I and mode II delamination. It is a common measure to compare the validity of a mode mixing criteria or theory to an experiment.

2.4.5. Delamination Criteria

As mentioned in the section 2.4.3, different criteria were derived with various methods of analyzing empirical data, however certain delamination criterion are based on a more fundamental theoretical background. Most of these criteria are evaluated in Reeder's study [47]. These are highlighted in the following paragraph:

Single Mode Criteria

The single mode criteria is applied in the SERR delamination model. In this criteria method it is assumed that the mode I delamination and mode II delamination operate independently from one other. Next to that the method also states that a general critical SERR will be the same in the laminate even when the loading changes. Demonstrated by the significant difference between critical SERR values and the other mechanism occurring, like the cusps forming for mode II delamination, it can quickly be pointed out that this criteria does not reflect the actual delamination behavior.

B-K Criterion

The B-K criterion is developed by Benzeggagh and Kenane [48]:

$$G_{TC} = G_{IC} + (G_{IIC} - G_{IC})\left(\frac{G_{II}}{G_T}\right)^m \tag{2.3}$$

Where m is a semi-empirical factor that makes the criteria fit with the found test data. The critical strain energy varies with the induced mode-mixing. This criterion is an applicable tool for engineers to calculate and measure the varying critical SERR with the MMB test. However, it does not explain why the SERR is varying with a shifting phase angle. Lastly the semi-empirical fitting factor does show that the process is defined by a power-law but does not explain why the effects are modeled with a power-law.

Bilinear Delamination Criterion

In Reeder's later work [49], delamination criteria is proposed where interaction is included between the mode I and mode II SERR's as following:

$$G_{Ic}^m = \zeta G_{IIc}^m + G_{Ic} \tag{2.4}$$

$$G_{Ic}^m = \xi G_{IIc}^m - G_{IIc}^m \tag{2.5}$$

Where ξ and ζ are material parameters that are determined experimentally. The method mainly assumes that failure of the layers occurs linearly in the extremes of either SERR region, based on the singular mode tests. Also this method is created based on any physical phenomenon.

2.5. VARIABLES THAT INFLUENCE THE DELAMINATION TESTING

For the one dimensional tests, many different studies have been performed to determine the influence of the geometric properties of the test specimen. The geometric measurements are normally performed by investigating the aspect ratios (width over length) of either laminate side in a delamination test, or by varying the thickness of the test specimens. A short description on the one dimensional research performed with either test is given in the following subsections.

2.5.1. INFLUENCE OF THE FINITE WIDTH

Davidson et al. [50] investigated the influence of the finite width on the SERR. In this study an analytical model was created and compared with a Finite Element (FE) counterpart. These models demonstrated that transverse coupling behavior was apparent in wider test specimens. This was further investigated by testing two different layups with various width's: the commonly used pure $[0]_n$ laminate and the orthotropic $[\pm 45]_n$ laminate. A factor to determine the severity of transverse shear coupling with the following coupling factor:

$$D_c = \frac{D_{12}^2}{D_{11}D_{22}} \tag{2.6}$$

At significant widths, a more severe response to coupling was found to the $[\pm 45]_n$ compared to the unidirectional laminates. A worst case estimated was a reduction of critical SERR of 9%. There was no experimental data given to support this statement by the author. This finite width problem demonstrates the limits of the 1 dimensional DCB test, where the width of has an influence on the data.

2.5.2. INFLUENCE OF THICKNESS

In more recent research, the influence of thickness of the test specimen on the critical SERR. One of the earlier major works is by Manshadi [51] who investigated the cohesive law with a semi-experimental optic method. Through a stash of optical fibers, Bragg gratings, Manshadi measured the local strains at the delamination front. The outcomes were translated in an averaged traction load versus displacement graph, which is the cohesive law of the material, which is given in figure 2.5 This cohesive law can then be combined with mea-
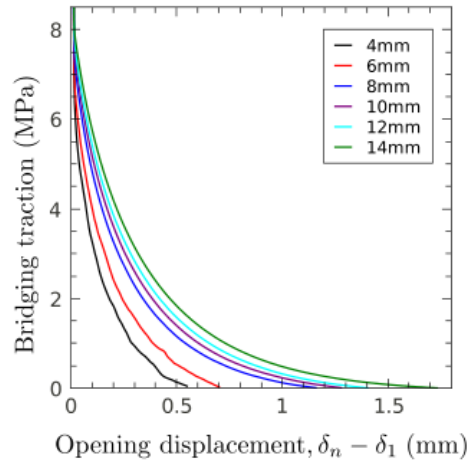
Figure 2.5: Cohesive Law in relation to the thickness of the specimen [4]

sured the compliance behavior to derive the resistance curve. The cohesive law demonstrates that thicker laminates do have a greater critical SERR (this is the integral traction stress and displacement). The cause for this significant difference in critical SERR was given by Manshadi[51] to be the smearing of stress near the crack front. This smearing of stress, the option to spread stress in the fracture zone before the delamination, is caused a greater fiber bridging zone. Fiber bridging offers more resistance to delamination, since the delaminated fibers obstruct further delamination, which enhanced the critical SERR.

2.5.3. INFLUENCE OF LAYUP

Aside from the geometric properties, the stacking sequence can cause coupling which affect the SERR. This effect is mainly captured with the transverse shear coupling factor D_c. Davidson [52], tested five differ-

ent layups in his work: isotropic, unidirectional laminate, [±15], [±30] and [±45]. All the laminates are orthotropic to cancel out the D_{16} and D_{26}.

The curvature effects caused by the layups, do spread out the SERR at which greater transverse shear coupling factor induces a greater spread of shear energy release rate. These conclusions were further supported by Davidson's newer model [53].

As mentioned in the geometric subsection, a wider spread of shear energy release rate will cause a greater critical SERR. This does comply with the experimental data of both Choi [54], O'Brien [55] and Polaha [5]. Especially in the later work, a clear investigation is done to find the relations between the layup sequence and the mix mode delamination. The results of this investigation is given in figure 2.6. These results link the
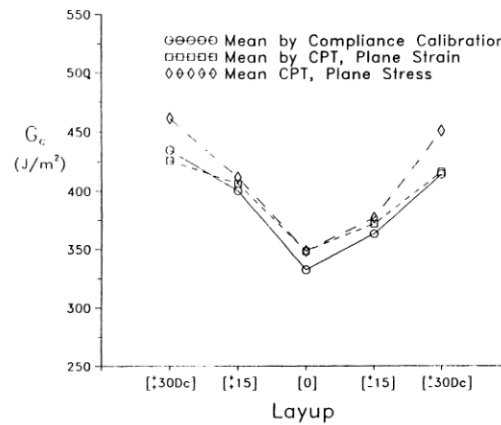
Figure 2.6: The critical ENF SERR versus the layup [5]

off-axis laminates, the varying of SERR with a varying phase angle and the general hypothesis on the smearing of SERR together. It is therefore worthwhile to investigate such effects in a planar test setting. As measured by Cameselle-Molares [6], different delamination patterns are found when non-isotropic laminate mats are used, see figure 2.7.

2.6. BOUNDARY CONDITIONS AND LOAD INDUCTION

The planar delamination test of composites is fairly new in its method to determine the fracture toughness of a plate. Two dimensional delamination of membrane structures have already been explored through multiple studies. One of the common methods to test fracture toughness of membranes is the William's blister test. This type of testing connects a thin elastic membrane to a rigid body, after which the membrane layer is delaminated through a load. The type of loading can be varied. The most common methods of loading are the pressurized blister and the shaft-loaded blister, seen in figure 2.8. While the blister test investigates isotropic membrane structures, which are thin plates with a small bending stiffness, composite laminates are plate-like structures with a significant bending stiffness. The load induction and choice for boundary conditions can give relevant insights to start further development of a planar delamination test.

The first work that tests the applicability of William's blister tests for the determination of delamination toughness was performed by Storaker [30]. Storaker's work is further investigating the claims by Williams [56], that
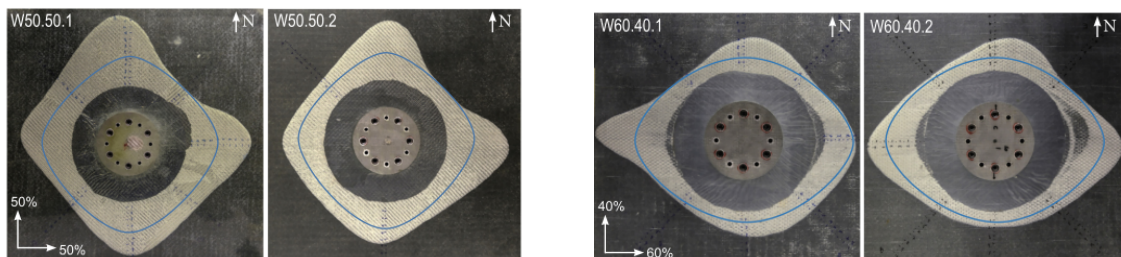
Figure 2.7: Delamination of a fiber mat with various stiffness over the principal axis:(*a*) 50%/50% (*b*) 60%/40% [6]
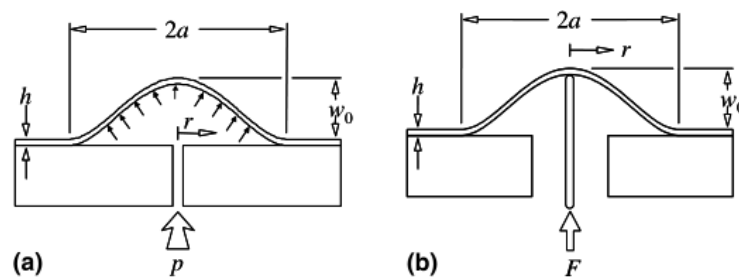
Figure 2.8: Schematics of the loading configurations for (a) pressurized blister, (b) shaft-loaded blister [7]

states the adhesive toughness is not a material property, but instead is reliant on global variables. It should be noted that William's work, did not investigate the SERR.

Storaker does work out an energy relation to describe the mechanics of delamination of membranes. Two extreme energy release rates are described, one for pure bending and one for pure stretching. These release rates scale with the induced load (pressure in this experiment) and the maximum displacement in the center. Since the maximum displacement is depending on material properties,this model does provide new insights regarding the displacement behavior.

The next step in further developing the blister test is analyzing the mode mixity of the layups. The fundamental research that defined mode mixity of isotropic materials is presented by Suo [57]. The study develops a generalist mechanical model that describes mode mixity for two elastic materials delaminating. This analysis gives a complex description of the crack stress intensity factor. The mode mixity is firstly described by the phase-angle. This model is further developed by Jensen [58], which compares the Suo model and in turn gives an understanding between the geometric and constituent properties. To make the mixity more measurable, Jensen continued his work [59] by drawing a relation of the mode-mixity that can describe a relation between bending stiffness and a normalized displacement (displacement over material thickness). While this specific solution only works for isotropic materials, it does demonstrate options to describe mode characteristics. Likewise solutions have been produced by Guo [7] and Jin [60]. Later works that finalize the blister test analysis are focused on non-linearity [61] and initial blister radius [62].

2.7. MEASUREMENT METHODS NON-TRANSPARENT LAMINATES

Many different measurement methods offer the opportunity to measuring delamination front within a composite material, however few methods can do so without being in contact with the test specimen. This mainly pushes the method of thermography, a method that indirectly measures irreversible damage mechanisms through the heat caused by thermal-elastic loading. This method usually comes paired with other techniques like DIC and Accoustic Emission (AE) during testing, or X-ray scanning after testing to validate the initial results. These methods will be briefly highlighted in this section.

2.7.1. THERMOGRAPHY

A promising methodology for this type of measurement is passive thermography, which has been a topic thoroughly explored by Lahuerta [63, 64] regarding lock-in thermo-elastic thermography. The approach by Lahuerta measures the released energy that occurs at the delamination front. This type of thermographic measurement is clearly explained in the work of Green [65] and has been tested before by Narayana Swamy [66] with a FLIR 315 infrared camera (with a sensitivity of 50 mK). While the method still meets it limits regarding accumulative error (10% in the worst case), these errors occurred due to the lack of synchronization, and the bit of mismatching data. This should be a major focus point for setting up any experiment. Next to that, the test performed by Narayana Swamy tested GFRP's, which is a poor thermal conductor. The current tests will be performed on CFRP's, which conduct heat better. The thermal conductivity does make it easier to measure heat patterns from the surface, so heat easily moves through the material. The heat conductivity also causes more clutter in the measurements to the more apparent dissipation of heat.

2.7.2. ACOUSTIC EMISSION

While thermography is a method that can locate irreversible damage induced in the material, it cannot measure which damage is induced. Other test methods are required to describe a more complete measurement. A measurement technique that describes the type of damage is that of acoustic emissions. This is a method that measures the elastic waves that traverse through material. A combination of these methods has been tested by Munoz [67]. This study combined with a model that could link the received acoustic signals with events that were spotted through a heat map on the test specimen. The results gave a clear insight on which damages were occurring in the specimen, at which location and at which point in time. The method tested by Munoz delivered only qualitative insights but is lacking on quantifying the damages.

2.7.3. DIFFERENTIAL IMAGE CORRELATION

DIC measures the strains on the surface of a specimen. DIC can do such measurements with the support of a speckle pattern that is applied on a test specimen. Through the displacements of separate individual speckles, displacements can be deduced from which strains can be derived. When a delamination occurs in a laminate, the stiffness of a laminate reduces locally. It should therefore be possible to locate a delamination through the detection of largely deforming sections with DIC. This behavior is what Venkatachalam [68] attempted to capture. By measuring the transverse strain, Venkatachalam was able to locate delamination spots, through post-processing. A similar method was applied by Cameselle-Molares [6] in which a DIC camera was able to follow a crack path that was predetermined through numerical analysis see figure 2.9. It
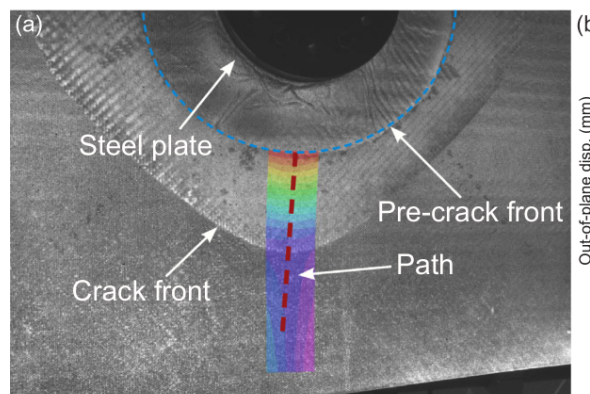
Figure 2.9: DIC measurements of plate W50.50.1; example image of area and path of interest[6]

is worthwhile to investigate the stress and strain effects, separately as well as combined for either the DIC measurement method or the thermography measurement method.

2.8. FURTHER RESEARCH

The literature study aimed to understand the general delamination behavior in a problem where a central delamination is growing in multiple directions. All the studies mentioned in this literature study that apply a mode-mixity criterion showed that it is complicated to determine the right critical SERR in a planar delamination problem. A set of studies apply either the mode II or the mode I critical SERR as onset delamination problem. Amaral and Danesjoo propose a method that works irrespective of the problem, while delivering a method to determine the delamination growth criterion. The current studies on delamination growth behavior in a planar setting are in conflict Kollner [29, 33, 34]. Where Chai and Wang do allow planar growth, Kollner allows only stable delamination growth in a single direction. There is an agreement regarding the elliptical delamination shape that occurs in different fields of studies [6, 26, 33]. There are no in-process measurements of the delamination behavior available in the literature. It is demonstrated that there is a lack of knowledge on delamination criterion and delamination growth behavior that requires new innovative measurement techniques.

3

ANALYTICAL INTERPRETATION OF THE PLANAR DELAMINATION PROBLEM

3.1. INTRODUCTION

As mentioned in chapter 1, semi-complex structures are tested to gain insight on more complex delamination behavior. When analyzing such semi-complex structures, it is important to have a firm understanding of the problem so that undesired effects can be avoided. For this reason, an analytical mechanical model is developed for this research. The most recent attempts to encapsulate planar delamination behavior are made by Yang [69] and Chen [70]. Yang describes the membrane delamination behavior of an isotropic membrane loaded in a similar manner to the transverse planar delamination experiment [6]. Yang's model only investigates isotropic materials and does not account for bending stiffness. Chen's [71] model describes an indentation test delamination behavior of a clamped laminate similar to numerical model by Davies [12]. The model proposed by Chen [71] simplifies the delamination growth to purely circular expansion, while circular expansion was not measured by Davies. An analytical model was developed, since no model investigates how the delamination growth occurs in a planar specimen. The analytical model proposed in this chapter will apply Classical Laminate Theory (CLT) for the constitutive material behavior in combination with the SED criterion to understand effects that are demonstrated in of transverse out-of-plane load opening planar delamination experiment [6]. The model will describe how delamination growth behavior develops the final delamination shape. The outcomes of the model are then compared with the experiment.

3.2. EFFECTS TO BE STUDIED

In chapter 2 it was mentioned that different discussions are still ongoing on the planar delamination growth. The main discussion that this analytical model will analyze is how the delamination grows from an initial circular delamination to an elliptical delamination. This effect has been described for planar buckling delamination behavior [29, 34] with the assumption that the material will offer the greatest delamination resistance (maximum SERR) it can possibly offer. Based on this assumption different theories for growth exist. Chai's research [29] states that delamination growth occurs in a stable (transverse) manner until the top layer of the laminate fails after which unstable (planar) delamination grows in a self-similar manner. The descriptions of this research do give insight on when planar delamination occurs, but not why it is happening. It is therefore the goal of this model to give an explanation when the delamination behavior turns from stable to unstable. Wang's research [34] made a model that can describe the onset delamination growth for through-width buckling delamination experiment with an initial elliptical delamination. While this study does describe the onset delamination point accurately, it cannot estimate the delamination propagation. It is therefore also a goal of this analytical model to give an understanding on how delamination propagation occurs in a planar delamination problem.

The current hypothesis is also that there is a direct relation between the SED and SERR. The investigated transverse planar delamination experiment used composite mats with various degrees of orthotropy which have different SERR's. The model can therefore test this hypothesis by applying SED values as criterion measured at the onset delamination versus a simulation where the SED values are equal between the composite mats.

Table 3.1: The constitutive properties of the investigated composite mats [6]

Plate	E_1 (GPa)	E_2 (GPa)	E_3 (GPa)	G_{12} (GPa)	ν_{12}	ν_{13}	ν_{23}	(l x w x t) mm
50/50	17.79	17.79	7.25	2.62	0.19	0.33	0.33	470 x 470 x 3.43
60/40	22.30	14.86	7.57	1.73	0.23	0.32	0.33	410 x 410 x 3.055
70/30	24.28	10.41	7.07	1.58	0.27	0.32	0.34	400 x 400 x3.355
80/20	27.03	6.76	6.90	1.48	0.31	0.31	0.34	410 x 410 x 3.555
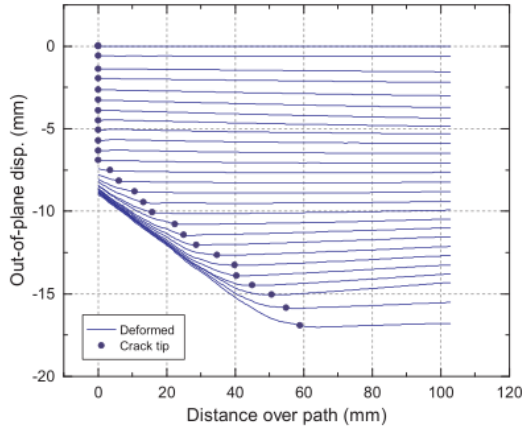
(a) Out of Plane Displacement of the composite mat delamination experiment [6]
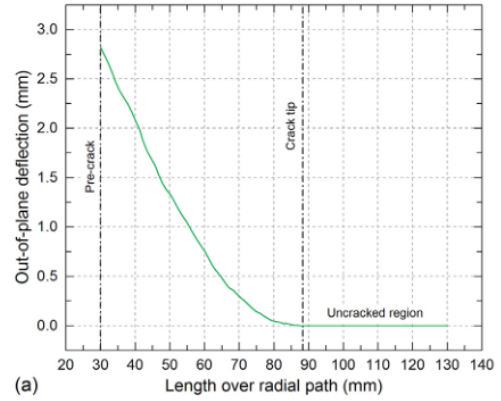
(b) Out of Plane Displacement of the composite mat, sandwich delamination experiment [38]

Figure 3.1: The out-of-plane displacement measurements used for the assumptions

3.3. Experimental Program

The transverse load-opening planar delamination experiment [6] that is being investigated tests a set of composite mats with various constitutive properties, see table 3.1. The experiment loaded the laminates until the delamination crack front lost its symmetric properties. This loss of symmetry is caused by matrix failure of the material. Figure 3.1 shows the out-of-plane displacement behavior that was measured during the experiments. The out-of-plane displacement only occurs within the delaminated area. The experiments have been performed with a displacement-controlled load induction, which means that the input of the model should also be a centrally induced displacement. Lastly the delaminations were measured as ellipses which have a major axis and minor axis, see figure 3.2.
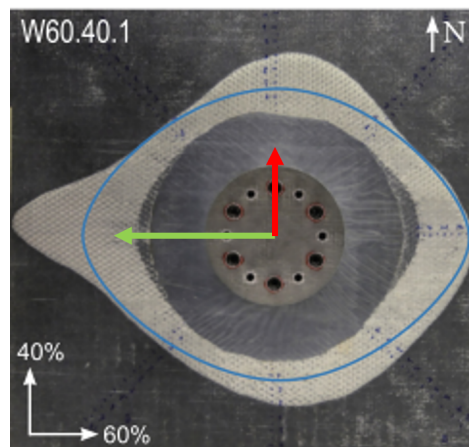
Figure 3.2: Delamination Shape Axes, green is the major direction and red is the minor direction [6]

3.4. ASSUMPTIONS

In this analytical model a set of assumptions are applied to model the planar delamination behavior in the most efficient manner. The thin-plate assumption is applied since the span over thickness ratio is large. The rule of thumb for the application thin-plate assumption is that it can only be used for plates that have an aspect ratio of $w/t > 20$ [72]. For the investigated experiment this aspect ratio is about 200, so the thin plate assumption is valid. To simplify the problem further, symmetry over the crack interface plane was assumed, which means that only one side of the mats was modeled. The next assumption, based on the out-of-plane displacement profiles, is that no out-of-plane displacement occurs outside of the delaminated region relative to the thickness center of the plate. Since major displacement behavior at the delamination boundary was out-of-plane displacement, it was assumed that bending strain energy will be the major contributor to SED at the delamination boundary. For the simplicity of this analytical model, in-plane stretching effects were ignored. Excluding in-plane stretching effects causes a more uneven distribution of SED at the delamination boundary. It was assumed that the SED will be constant throughout the whole delamination process. Since there are currently no measurements on the development of the SED during crack propagation this can neither be proven or disproven. Interface effects, like fiber-bridging, were not included in this model.

3.5. DISPLACEMENT FIELD

The planar out-of-plane delamination problem is quite complicated since it combines non-linear mechanics with orthotropic materials. With the out-of-plane displacement only occurred in the delaminated area, this model approached the delamination behavior as a moving boundary conditions problem. During the experiments the circular initial delamination turned into an elliptical delamination. Therefore the outer boundary was described as an elliptical delamination, since a circle is a special type of ellipse. To encapsulate continuous displacement behaviour, the model simplifies the boundary condition at the clamp radius and assumes a central displacement (w_0) in the center of the delaminated plate. The boundary conditions were defined as following:

$$w(S_{elips}) = 0 \tag{3.1a}$$

$$\frac{\partial w(S_{elips})}{\partial n} = 0 \tag{3.1b}$$

$$w(0,0) = w_0 \tag{3.1c}$$

$$dw(0,0) = 0 \tag{3.1d}$$

Where $w(S_{elips})$ is the displacement field and n is the normal direction of the delamination boundary. To simplify the solution to this boundary condition problem, the problem is first solved in a one-dimensional manner.

$$w(a,0) = 0 \tag{3.2a}$$

$$\frac{\partial w(a,0)}{\partial x} = 0 \tag{3.2b}$$

$$w(0,0) = w_0 \tag{3.2c}$$

$$\frac{\partial w(0,0)}{\partial x} = 0 \tag{3.2d}$$

Where a is the delamination length in the x-direction. A third order polynomial would be able solve this set of boundary conditions.

$$w(x) = A + Bx + Cx^2 + Dx^3 \tag{3.3}$$

Implementing this third-order polynomial in the set of equations results in the following set of equations.

$$0 = A + Ba + Ca^2 + Da^3 \tag{3.4a}$$

$$0 = B + 2Ca + 3Da^2 \tag{3.4b}$$

$$w_0 = A \tag{3.4c}$$

$$0 = B \tag{3.4d}$$

The solutions of this equation set is the one-dimensional displacement equation.

$$w(x) = w_0 \left(1 - 3\left(\frac{x}{a}\right)^2 + 2\left(\frac{x}{a}\right)^3 \right) \tag{3.5}$$
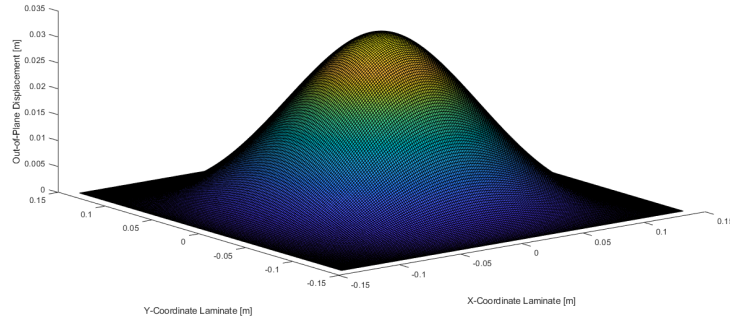
Figure 3.3: Central Delamination Displacement Model for the 50/50 GFRP Composite Mat

The ratio of crack length and the x-coordinate is central to the one-dimensional solution. To translate this one-dimensional solution to a two-dimensional solution this ratio can be interchanged with the ratio of the delamination ellipse radius and the corresponding x- and y-coordinate. The two-dimensional displacement field is therefore as following:

$$w(x,y) = w_0 \left(1 - 3\left(\frac{x}{r_e(\theta)}\right)^2 + 2\left(\frac{x}{r_e(\theta)}\right)^3\right)\left(1 - 3\left(\frac{y}{r_e(\theta)}\right)^2 + 2\left(\frac{y}{r_e(\theta)}\right)^3\right) \tag{3.6}$$

In this formula r_e is the radius of the ellipse which is as following:

$$r_e(\theta) = \frac{ab}{\sqrt{b^2\cos^2(\theta) + a^2\sin^2(\theta)}} \tag{3.7}$$

Where b describes the delamination length in the minor semi-axis, and θ describes the angle of the displacement field location with respect to center of the coordinator system.

$$\theta = \arctan(\frac{y}{x}) \tag{3.8}$$

The displacement field is illustrated in figure 3.3. To reintroduce the clamp was used to induce the load in the transverse planar delamination experiment the displacement field was altered. The displacement field was cut off at the radius of the clamp. The out-of-plane displacement at the clamp radius was matched to the central out-of-plane displacement in the experiment. This transformation is the following:

$$w_{0T} = \frac{w_0}{1 - 3\left(\frac{r_c}{r_{avg}}\right)^2 + 2\left(\frac{r_c}{r_{avg}}\right)^3} \tag{3.9}$$

In equation 3.9 r_c is the cut-off radius, and r_{avg} is the average ellipse minor semi-axis and major semi-axis. The resulting displacement field is illustrated in figure 3.4.

3.6. APPLYING THE STRAIN ENERGY DENSITY CRITERION

The SED is the product of the second derivatives if the displacement fields and the laminate bending stiffness. The second derivatives of the displacement are calculated as following:

$$w_{xx} = \frac{\partial^2 w}{\partial x^2} \tag{3.10a}$$

$$w_{yy} = \frac{\partial^2 w}{\partial y^2} \tag{3.10b}$$

$$w_{xy} = \frac{\partial^2 w}{\partial x \partial y} \tag{3.10c}$$
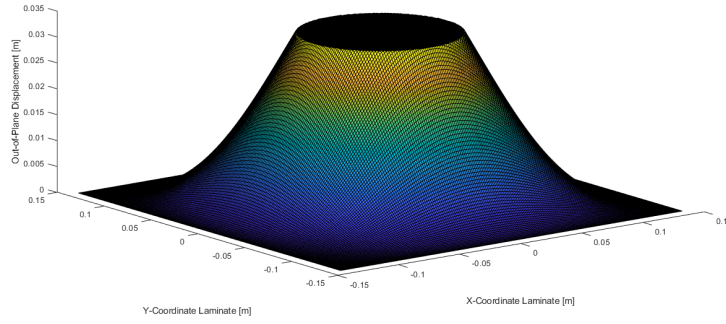
Figure 3.4: Clamped Central Delamination Displacement Model for the 50/50 GFRP Composite Mat

The laminate bending stiffness is determined with CLT to be as following:

$$\begin{Bmatrix} M_x \\ M_y \\ M_{xy} \end{Bmatrix} = \begin{bmatrix} D_{11} & D_{12} & D_{16} \\ D_{12} & D_{22} & D_{26} \\ D_{16} & D_{26} & D_{66} \end{bmatrix} \begin{Bmatrix} \kappa_x \\ \kappa_y \\ \kappa_{xy} \end{Bmatrix} \tag{3.11}$$

Where $kappa$ describes the curvature and M describes the moment in the respective axis. The SED of the laminate can be determined as following:

$$\frac{dU}{dV} = \frac{1}{t_{lam}} \left(w_{xx} D_{11} w_{xx} + 2 w_{xx} D_{12} w_{xy} + 4 w_{xx} D_{16} w_{xy} + w_{yy} D_{22} w_{yy} + 4 w_{yy} D_{26} w_{xy} + 4 w_{xy} D_{66} w_{xy} \right) \tag{3.12}$$

Where the t_{lam} is the thickness of the laminate. The total potential energy of the delaminated area can be described as following.

$$\Pi = U - W \tag{3.13}$$

Where U is the strain energy available in the delaminated area.

$$U = t_{lam} \int_{-a}^{a} \int_{-(b/a)\sqrt{a^2 - x^2}}^{(b/a)\sqrt{a^2 - x^2}} dU(x, y) \, dy \, dx \tag{3.14}$$

Whereas W describes the work applied to the laminate.

$$W = w_0 P_z \tag{3.15}$$

In the work equation 3.15 the variable P_z describes the transverse center load. The radius of the ellipse function, x-and y-coordinates can be transformed into cylindrical coordinates with a radius that depends on the angle.

$$x = r_e(\theta) \cos(\theta) \tag{3.16a}$$
$$y = r_e(\theta) \sin(\theta) \tag{3.16b}$$

Assuming a constant SED criterion the development of the SED can be well demonstrated by figure 3.5. The development of a critical SED at one angle to two angles show how the stable transverse crack growth develops into unstable planar crack growth, when an equal SED is available at both crack growth directions.

3.7. SIMULATION OF THE EXPANDING DELAMINATION

To apply the SED criterion in a simulation, a simple model has been setup according to the scheme presented in figure 3.6 .The inputs that are required for the model are the material properties of the test specimen, the initial delamination radius, the maximum applied displacement, the radius of the load induction clamp in the experiment and the amount of calculation increments that should be performed. The outputs of the
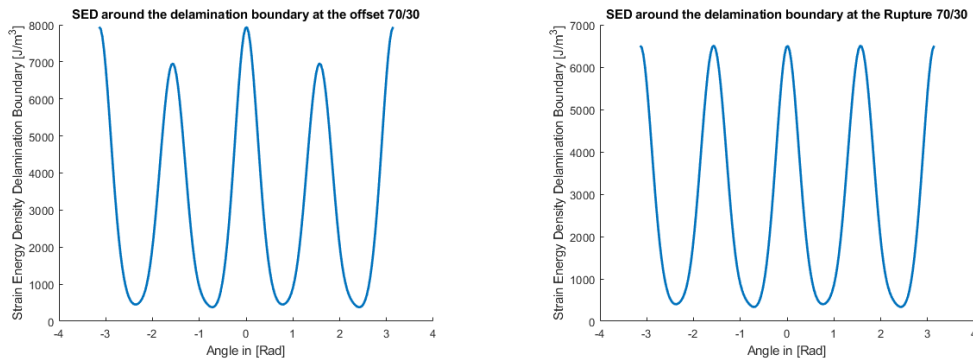
Figure 3.5: The SED around the boundary of the delamination for the 70/30 Composite Mat: a) at the offset b) at the rupture

model are the delamination size vectors in the primary and secondary delamination direction. The model will perform a CLT analysis and calculate the SED function. This SED function is then inserted in a calculation scheme with the initial delamination size and the maximum displacement. The displacement will be incremented with the set increment step. The code will then determine the maximum SED at the delamination boundary. When the SED is greater than the critical SED, the code starts expanding the delamination until the SED at the boundary is below the critical value. This expansion effect is the exchange of work for delamination area, which is bound by the law of conservation of energy. The model will therefore always demonstrate stable behavior. When the delamination expands in the stiffest direction, the stiffness in that
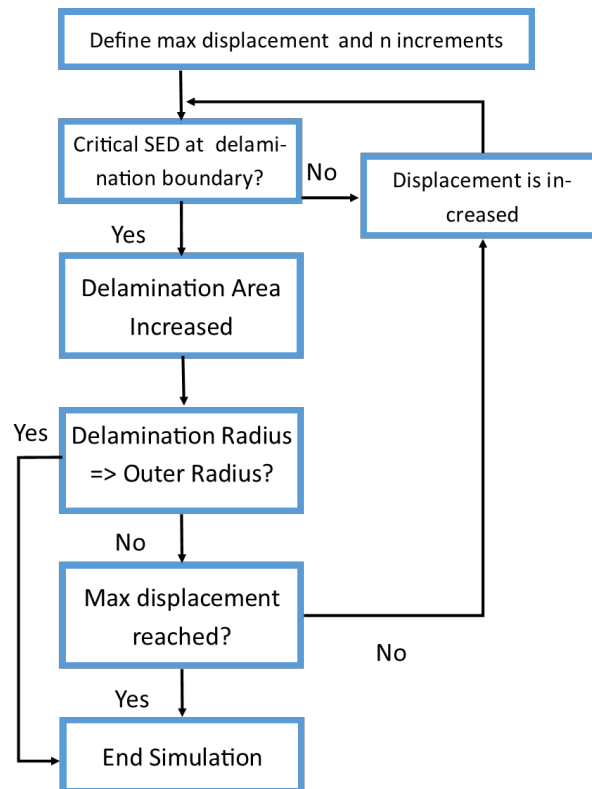
Figure 3.6: The Analytical Model Solver Scheme

direction will be reduced. This also means that the SED will decrease in that direction. Figure 3.5 shows how the SED varied around the delamination boundary before and after the expansion of the delamination, to demonstrate this effect. This stability resulted into a delamination equilibrium shape, after which the delamination developed in a self-similar manner. This equilibrium shape is the ellipse that was measured in the experiment. The comparison of the equilibrium ellipse of the model and experiment is documented in table

Table 3.2: Comparison Ellipse Shapes Experiment and Model with the equilibrium Strain Energy Density

Plate	$w_0 (mm)$	$\frac{a}{b}{}_{exp}$	$\frac{a}{b}{}_{mod}$	SED $\frac{kJ}{m^3}$
50/50	32.8	1.0000 (140/140)	1.0000	3.301
60/40	26	1.2857 (135/105)	1.1182	2.71
70/30	17.5	1.1967 (110/92)	1.2361	6.52
80/20	12	1.3043 (120/92)	1.4119	2.1

3.2.

3.7.1. CALCULATION OF THE STRAIN ENERGY RELEASE RATE WITH DELAMINATION VECTORS

The outcomes of the simulation were the delamination growth vectors. A Matlab script (documented in appendix C) calculated the SERR for each instance in which the delamination size was increased. The SERR was calculated by applying equation 3.21. By removing the parts of the data where delamination was not occurring, the data was analyzed with a 3rd order polynomial curve fit, through Matlab's curve fitting toolbox.
 The resulting SERR plots (figure 3.7) demonstrate that the SERR converges to a singular value. After the first

(a) Mat 50-50

(b) Mat 60-40

(c) Mat 70-30

(d) Mat 80-20
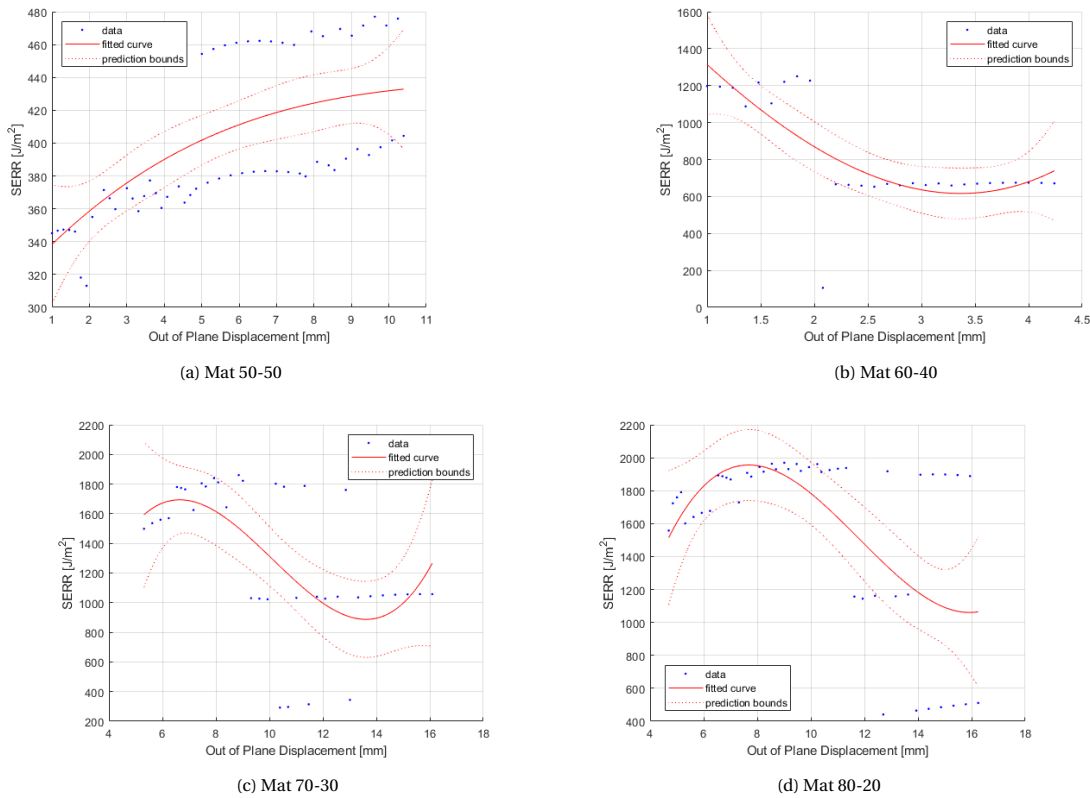
Figure 3.7: The SERR of the various composite mats calculated with the SED's given in table 3.2 fitted with a 3rd order polynomial

set of simulations were run without the SED's derived from the rupture experimental data, a second set of simulations were where the SED was all equal to that of the 70-30 rupture SED. The SERR of the second simulation 3.8 also converge to a singular value. After investigating the aspect ratios during the test, figure 3.9, it was concluded that the point at which the SERR converges, seems to be when the equilibrium shape is fully developed.

(a) Mat 50-50

(b) Mat 60-40

(c) Mat 70-30

(d) Mat 80-20
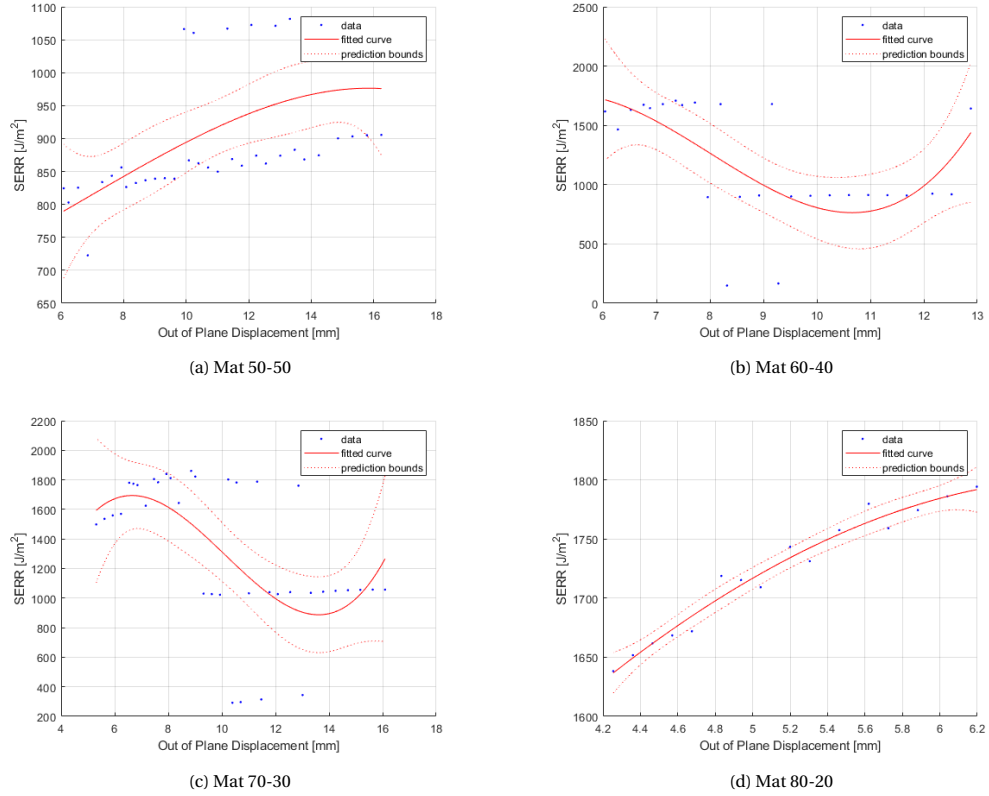
Figure 3.8: All the SERR of the mats with identical SED demonstrating the orthotropic influence on the SERR

3.7.2. CALCULATION OF THE CENTER LOAD WITH THE DELAMINATION VECTORS

The next step in the analysis of the model was by investigating the load-displacement behavior. The load was derived with the first Von-Karman equation, which is as following:

$$
D_{11}\frac{\partial^4 w}{\partial x^4} + 2(D_{12} + 2D_{66})\frac{\partial^4 w}{\partial x^2 \partial y^2} + D_{22}\frac{\partial^4 w}{\partial y^4}
$$
$$
= N_x\frac{\partial^2 w}{\partial x^2} + 2N_{xy}\frac{\partial^2 w}{\partial x \partial y} + N_y\frac{\partial^2 w}{\partial y^2} - p_x\frac{\partial w}{\partial x} - p_y\frac{\partial w}{\partial y} + p_z
$$
(3.17)

Where N with subscripts are the in-plane applied loads and the variable p with subscripts are the external applied pressures. Since the load can be modeled as point force at the center of the plate, the Von-Karman equation was simplified.

$$
D_{11}\frac{\partial^4 w}{\partial x^4} + 2(D_{12} + 2D_{66})\frac{\partial^4 w}{\partial x^2 \partial y^2} + D_{22}\frac{\partial^4 w}{\partial y^4}
$$
$$
= P\delta(x - x_{center})\delta(y - y_{center})
$$
(3.18)

Where δ is the Delta Dirac function that can be expressed with equation 3.19.

$$
\delta(x - x_0) = \begin{cases} 1 & \text{if } x = x_0, \\ 0 & \text{otherwise.} \end{cases}
$$
(3.19)

Due to the boundary conditions the exact load at the center is infinite. To approximate the load that is occurring in practice, the load is approached by calculating the limits as close as possible to actual center load. The values assumed for x_{center} and y_{center} is 0.01 mm. The simulation outcomes, the delamination vectors, and the displacement vector used for the simulation are then used in a small script which returns the plots in figure 3.10. The simulated load-displacement graphs demonstrate the load drops similar to measured load-displacement graphs of the experiments, illustrated in figure 3.11.

(a) Aspect Ratio development of the mat 50-50

(b) Aspect Ratio development of the mat 60-40

(c) Aspect Ratio development of the mat 70-30

(d) Aspect Ratio development of the mat 80-20
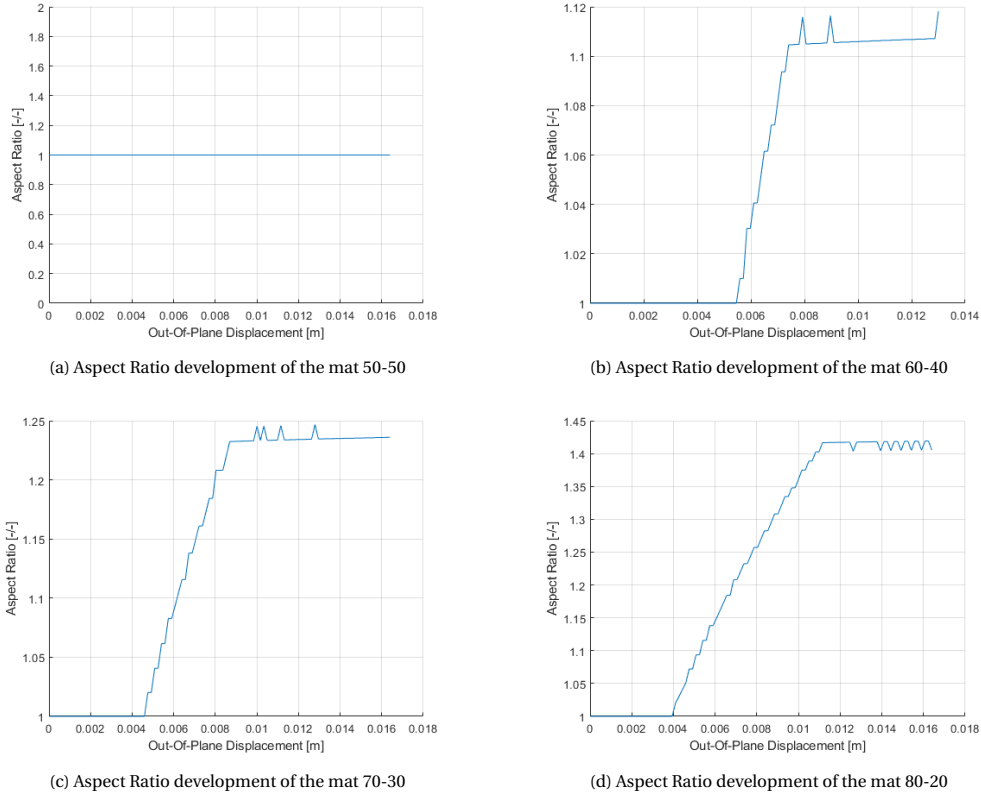
Figure 3.9: All the Aspect Ratios of the various mats with a critical SED of 7943 $[J/m^3]$

3.8. EVALUATION OF THE SERR AT THE OFFSET AND RUPTURE

With the load-displacement behavior acting accordingly the last step in finalizing the model was by calculating the SERR. Due to the complexity of the problem an exact integration required too much computational power. The determination of the SERR was therefore performed with a numerical integration scheme. The numerical integration functions by increasing the delamination size with a small fraction.

$$a_1 = (1 + \Delta)a_0 \tag{3.20a}$$
$$b_1 = (1 + \Delta)b_0 \tag{3.20b}$$

Where Δ is a very small number. For the numerical estimations of the SERR, $\Delta = 0.001$. The general numerical integration of the SERR is:

$$G = \frac{dU}{dA} = \frac{U(a_1, b_1) - U(a_0, b_0)}{\pi(a_1 b_1 - a_0 b_0)} \Big|_{w_0} \tag{3.21}$$

The SERR of transverse delamination growth can be determined in a similar manner.

$$G = \frac{U(a_1) - U(a_0)}{\pi b(a_1 - a_0)} \Big|_{w_0} \tag{3.22a}$$
$$G = \frac{U(b_1) - U(b_0)}{\pi a(b_1 - b_0)} \Big|_{w_0} \tag{3.22b}$$

To reduce the calculation time and to exclude the clamped region in the area integration, the strain energy is instead integrated over a quarter plate and multiplied by four.

$$U(a_1, b_1) = 4 \int_{-a}^{-r_c} \int_{-(b/a)\sqrt{a^2 - x^2}}^{(b/a)\sqrt{a^2 - x^2}} dU(x, y) \, dy \, dx \tag{3.23}$$

Where r_c is the radius of the clamp, which is where no energy dissipation of the material occurs. The onset SERR was determined for the material in the primary direction for the transverse delamination and for planar
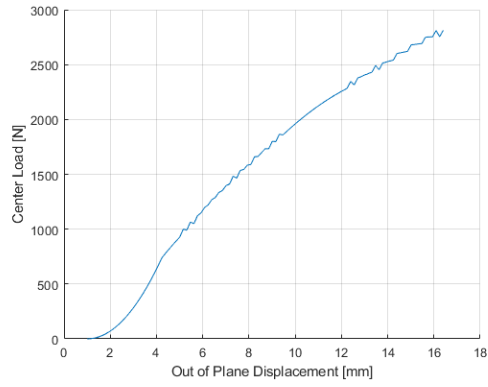
(a) Load Displacement Graph of the 50-50 Composite Mat
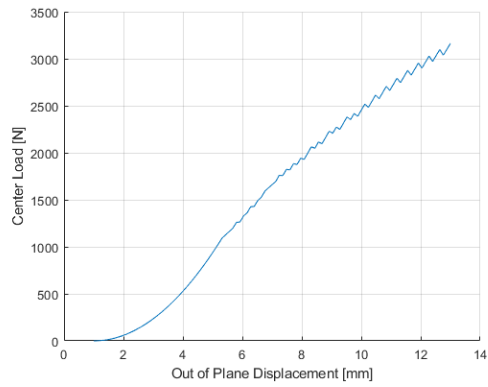
(b) Load Displacement Graph of the 60-40 Composite Mat
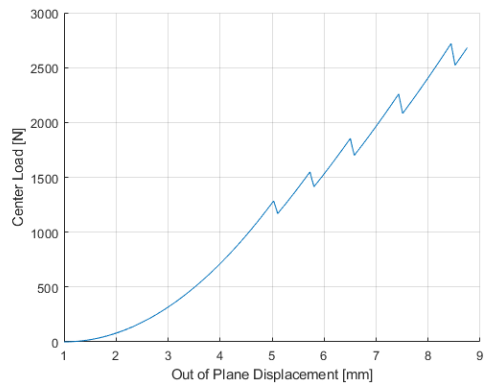
(c) Load Displacement Graph of the 70-30 Composite Mat
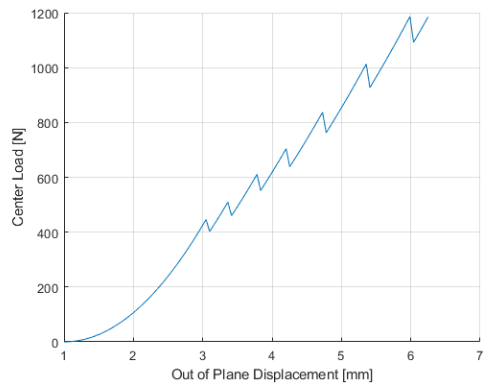
(d) Load Displacement Graph of the 80-20 Composite Mat

Figure 3.10: All the Load Displacement Graphs
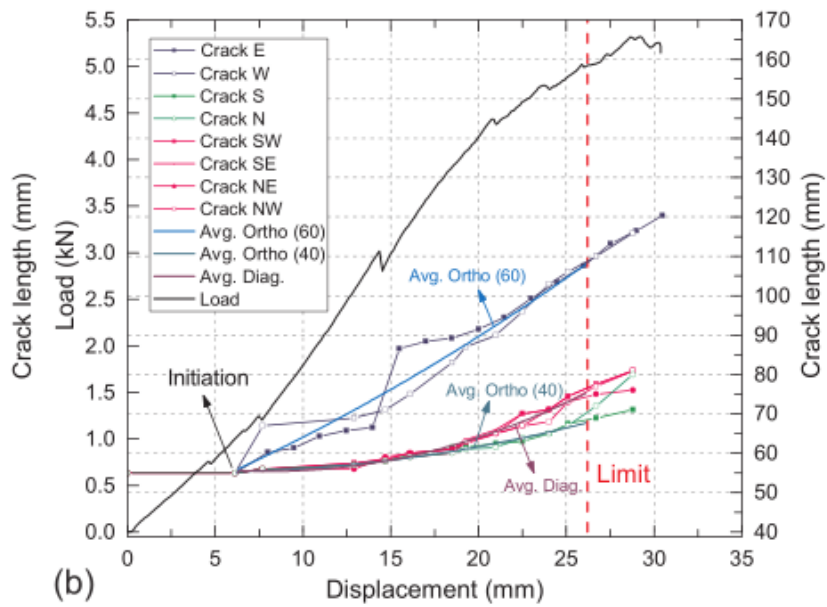
Figure 3.11: The load-displacement graph of mat 60-40 [6]

Table 3.3: The onset SERR of the various composite mats

Mat	$G_{ca}(J/m^2)$	$G_{cA}(J/m^2)$
50/50	460	187
60/40	733	292
70/30	871	345
80/20	544	214

Table 3.4: The equilibrium Strain Energy Release Rate of the various composite mats

Mat	$G_{ca}(J/m^2)$	$G_{cA}(J/m^2)$
50/50	547	384
60/40	1547	801
70/30	1470	778.9
80/20	458	289.72

delamination. Table 3.3 demonstrates that the onset SERR for transverse growth is nearly twice as great as the planar onset SERR. When the whole delamination developed into an identical SED at the boundaries in the primary and secondary direction, unstable planar delamination growth occurred. The stable transverse growth SERR was compared with the unstable planar growth SERR. The outcomes regarding the stable and unstable are presented in table 3.4. At the rupture of the experiment the SERR of the transverse growth is also about twice as great as the planar growth SERR. The assumption is that the delamination shape developed into the least resistant form, which it would be when the SED was at equilibrium.

3.9. CONCLUSION

The CLT bending model with SED criterion demonstrated accuracy when the simulated delamination ellipses are compared with the experimental delamination ellipses. The application of the SED criterion did allow to explain the point at which the delamination propagation behavior turned from stable transverse to unstable planar delamination. This change in delamination behavior was caused by the SED equilibrium in the major and minor elliptical delamination direction. The balance of the SED demonstrate that the laminate allows for the most efficient delamination growth, which creates the equilibrium delamination shape. During a planar delamination test, the SERR decreased when the displacement is increased, when no interface effects were ignored.

An investigation of the relation between the orthotropy and the SERR a simulation was performed in which the SED of all the different delamination mats were set to the same value. Based on this test it was concluded that the SERR will increase when a material is more orthotropic. This means that fiber-bridging is not the only induced effect that causes an increase in delamination resistance. With the same simulations, the load displacement plots demonstrated behavior that was monitored during the delamination tests. Load drops were monitored at the expansion of the delamination size, which is when work would be transformed into an increase of delamination area. The load values showed similarity with values measured in the delamination test.

Since the model did not account for fiber bridging effects since no quantitative experimental insights were given. The influence of fiber bridging on planar delamination behavior should therefore be further investigated while using specimen with a singular orthotropic property.

4

DESIGN OF THE EXPERIMENT

4.1. INTRODUCTION

With the insights gained from the literature study and the analytical study, an experiment was developed to measure planar delamination behavior in a CFRP specimen. An overview was given on the more common delamination test methods and a set of design requirements for the experiment were defined. The common delamination tests were then reviewed on their applicability for the novel planar delamination experiment. A specimen designed followed from the review of the common delamination tests.

Lock-in thermography and DIC were the proposed measurement methods. The method of lock-in thermography was described in Meola's research [22].The analytical study delivered insights on how delamination can be measured with DIC by applying the SED criterion. The initial setup was then designed accounting for the limitations of the equipment. Based on the failure load of the specimen design and limitations of the equipment, a set of requirements for the fixture were defined. To final part of the experimental is the structural design of the specimen fixture.

4.2. SPECIMEN DESIGN SELECTION

The current characterization tests for the delamination resistance of FRP specimens are the DCB,ELS and the ENF test. While these tests operate well in a coupon setting, not all tests can be easily translated to a planar setting. Aside from the standardized tests, many different coupon delamination experiments were considered, see figure 4.1. All the different experiments were designed for a specific delamination mode. To determine the applicability of transforming each of the tests from a coupon specimen to a plate specimen, the test methods were compared with a set of criteria. To investigate the applicability of mode II delamination tests, Davies [73] has defined a set of criteria that was used in this research as well:

- Consistency of results

- Simplicity of fixtures

- Stability of propagation

- Checks on validity

- Time needed to run tests

For the experimental setup, some of these criteria were less critical than others. For example, the time needed to perform a test was not a major important factor for a novel experimental setup. Based on the outcomes of different studies [8, 42, 73, 74], design table 4.1 was created to gain general insight in the coupon delamination tests. Not all test methods are suitable to be applied in a planar delamination test like the test methods that apply three- or four-point bending. This type of tests requires the bending load to be induced in the delamination direction, which cannot be achieved in a planar test since the delamination propagation direction is hard to determine and can also change overtime. The changing delamination propagation direction was demonstrated in the analytical study. This removes the ENF, Over-Notched Flexure (ONF), MMB , Single Leg Bending (SLB) and Over Leg Bending (OLB) as suitable test methods that are worth exploring in a planar
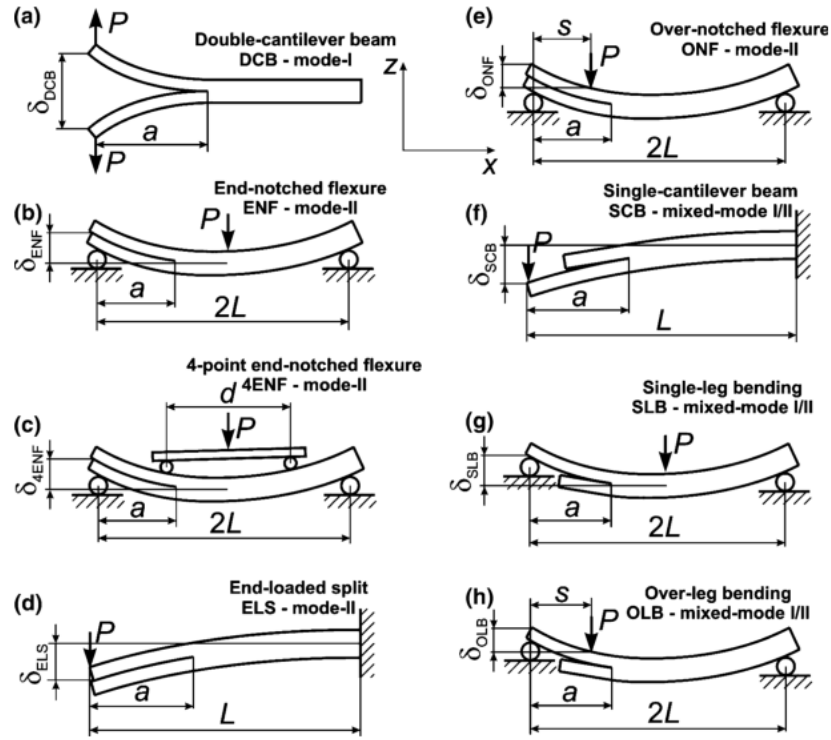
Figure 4.1: Schematic illustration of the various composite fracture specimens [8]
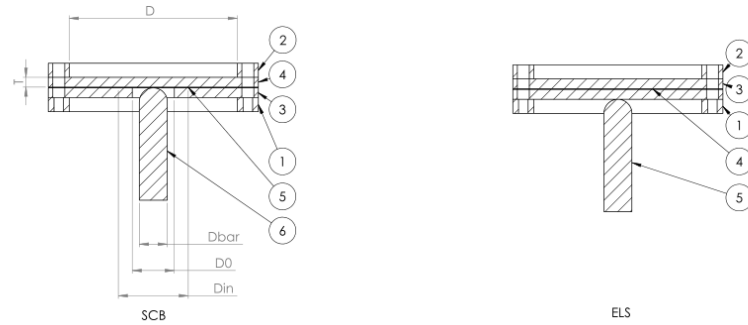
Figure 4.2: Planar SCB and ELS tests

delamination test.

The remaining coupon tests that were translated to a planar test were the the SCB and ELS test. Since the difference between these two tests are a single difference in manufacturing method, the hypothesis that the SED criterion is independent of load induction was also investigated. The design of the clamped specimen is illustrated by figure 4.2 .

4.3. VARIABLES TO MEASURE
Following from the research goals, the following effects were measured to gain meaningful insights.

- The delamination growth behavior in process

- The SED at the delamination front

- The SERR development during the experiment

With the topological experimental set-up decided, these effects were supposed to be measured while the specimen is loaded with an out-of-plane load. Optical measurement techniques were an ideal solution for

Table 4.1: Comparison Table current delamination tests

Name Test	Delamination Mode	Stability	Simplicity Fixture	Consistency Outcome
DCB	Mode I	Stable	Simple	Consistent
ENF	Mode II	Limited Stability	Simple	Consistent
ELS	Mode II	Stable	Clamping Variability	Less Consistent
ONF	Mode II	Stable	Simple	-
SLB	Mixed Mode I/II	Limited Stability	Simple	-
MMB	Mixed Mode I/II	Limited Stability	Simple	Less Consistent
SCB	Mixed Mode I/II	Limited Stability	Simple	-
OLB	Mixed Mode I/II	Stable	Simple	-

Table 4.2: Properties of the FLIR A655sc Thermal Camera

IR Resolution	640 x 480 Pixels
Thermal Sensitivity (At Room temperature)	50 mK
Accuracy	$\pm 2^o C$
Focal Length	24.6 mm
Room Temperature Range	$-15^o C$ to $50^o C$
Detector Time Constant	Typical 12 ms
Accuaracy	$\pm 2^o C$ or $\pm 2\%$ of reading
Field of View	$25^o x 19^o$
Minimum Focus Distance	0.25m

measuring the area of the specimen. Optical measurement techniques also have the benefit that they do not interfere the experiment and can easily be combined. The optical measurement techniques selected for tracking the delamination pattern are thermography and DIC. The DIC measured the displacements on the surface of the laminate. The strains of the laminate can be derived with this technique which can then be used with the constituent properties to estimate the SED according to equation 3.12. To derive the SERR, the calculation of the physical SERR is applied. This calculation required the delamination area measured, captured by lock-in thermography setup, and the load-displacement data obtained by tensile-testing machine.

4.3.1. SELECTED EQUIPMENT
With the experiment techniques defined, the available equipment in DASML was inventoried to select the necessary equipment:

- To measure the SED , 3D DIC test equipment was selected with the 5MP cameras

- To measure the delamination growth with thermography the FLIR A655SC camera was selected

- To measure the load-displacement behavior the MTS-100kN was selected

LIMITS OF THE EQUIPMENT
Thermography is mainly a qualitative tool that can give insights into the general delamination behaviour. The specifications of the thermographic camera are given in table 4.2. The specifications of the thermal camera also demonstrate the limitations of the equipment like the minimum focus distance and the resolution of the camera. Next to the limitations of the equipment inherent measurement disturbances was evaluated like the heat diffusion between the delamination crack and the measured surface. This means that the measured profile is not directly identical to that of the delamination in the material. This required a translation step between the measured heat profile to the actual delamination shape. To track the delamination area, a phase-filter is made for post-processing. Lastly external disturbances were accounted for, like the temperature variations in the laboratory. A frequency-controlled heat source was used to excite the temperature on the surface which made it possible to filter out temperature fluctuations. Table 4.2 includes all the specifications for thermography equipment.

 The DIC equipment available was the VIC 3D kit, with two 5MP cameras. For this setup a lens of 23 mm was selected to allow for a maximum area of interest. Table 4.3 includes all the specifications for DIC equipment. The system also depended on the correlation of the applied speckle pattern. The correlation parameter of

Table 4.3: Properties of the DIC camera

Resolution Camera	1920x1080
Operational Area Sizes	≤ 1mm to ≥ 50m
Resolution	1 nm

the speckle pattern was allowed to vary between 0.01 and 0.001 over the complete laminate. The size of the speckles were determined once the system was set up. The limitations described in the equipment tables were transformed in a list of criteria that the specimen and the fixture must comply with. This list of criteria is the following:

- The fixture should create a minimal distance of 40 cm so the thermography camera can accurately measure the delamination size

- The fixture should be sufficiently stiff, so that most of the measured load is measured by the load-cell of the MTS 100 kN

- The specimen and fixture width cannot be greater than 45 cm, due to the maximum width of the MTS 100 kN

- The fixture should be open to allow light on the surface that DIC method will measure

4.4. DESIGN OF THE SPECIMEN

With the equipment selected and set of limitations defined, the specimens were designed. The desired layups were selected for this setup, by limiting the orthotropy. The layups directly defined the thickness of the specimens. The surface size of the specimens were selected based on the equipment limitations. With all these parameters set, a maximum load was derived at which the specimen would fail.

LAYUPS

In the previous planar delamination research [6] a test setup was used with specimen that varied in their orthotropic properties. The analytical study discovered that with an increase of the orthotropy, the SERR would increase as well. Therefore no insights were generated on the fiber bridging effects. Specimens with different interfaces were designed to gain insight on the fiber bridging effect. To make an actual comparison between the two test outcomes, orthotropy should be avoided. The only manner to avoid the effects of orthotropic properties in specimen with various interfaces was to design quasi-isotropic layups. The interfaces that were evaluated in prior research [5, 75–77] are as following:

- the 0/0 interface, used for the current delamination standards

- the +30/-30 and +45/-45 which have been used for exploring the SERR variations at the crack front

The second condition for the layups was that they should remain symmetric and balanced after delamination. This required that the laminates had symmetry in the complete laminate as well in the delaminating parts of the laminates. This resulted in a layup design of 16 layers, reported in table 5.2.

4.4.1. QUANTITY

The quantity of test specimen were defined by the standard deviation and coefficient variance of the test standards. According to the ASTM standard of precision and bias [78], an initial set of tests are required to be performed to calculate this parameters. The purpose of this experiment was then to determine the desired amount of tests can be then defined based on an error margin. The minimum amount of tests required to achieve this goal was defined by ASTM standard for sample size determination [79]. Table 4.4 reports on the selected sample sizes.

4.4.2. AREA AND THICKNESS

The geometric design of the laminates was defined by the previous design steps. The thickness of the laminates was fixed at 16 layers of the available material. Therefore the laminate were 2.5mm thick. The area of the laminate was not fixed by prior design choices, but was limited by the span of the MTS-100 kN machine.

Table 4.4: The quantity of laminates used for tests

Type of Laminate	QS Pure Mode II	QS Mixed Mode I/II	Fatigue Mixed Mode I/II	Total
QI00	3	2	1	6
QI30	3	2	1	7
QI45	3	3	1	7
ORT15	1	0	0	1
ORT30	1	0	0	1
Total	11	8	3	21

Table 4.5: Lamina Strength Properties of M30SC-150-DT120-34

Test Condition	Strength MPa
0° Tensile	3161
0° Compression	1057
90° Tensile	29
90° Compression	123
In-Plane Shear	106.2
Interlaminar Shear	78.33

A greater specimen area would allow for a greater measurement area, which means a better tracking of the delamination area. The span of the MTS-100 kN is 530 mm. To make this experiment comparable with the previous planar experiment [6], area size was selected to be a square of 400 mm x 400 mm.

4.4.3. MAXIMUM TEST LOAD OF THE SPECIMEN

With the specimen design set, the next step was to calculate the failure load of the specimen which will limit the test cycle. The strength properties of the lamina were requested and reported in table 4.5. A knockdown factor was applied on the strength values, see table 4.6. Then the Tsai-Hill criteria were applied to determine the strength of the quasi-isotropic laminate. The results are reported in table 4.7.

The maximum load also depended on the type of bolts that were used for clamping, the distance between the edge of the laminate and the clamp holes. In section 4.5.3 , the choice for the metric thread was specified. Naik's research[80] developed a simplified method to derive the various failure loads that can occur in a FRP's.

$$F_{bearing} = \sigma_{Uc} d t_c \tag{4.1a}$$

$$F_{NetTension} = \sigma_{Ut}(w - d) t_c \tag{4.1b}$$

$$F_{ShearOut} = \tau_{Uc} 2 e t_c \tag{4.1c}$$

$$F_{CornerShear} = \frac{t_c}{2} [(w - d)\sigma_{Uc} + 2e\tau_{Uc}] \tag{4.1d}$$

Where d is the thread diameter, t_c is the plate thickness, e is the distance between the center of the thread hole and the side of the laminate and w is the width of the laminate. The outcomes of the calculations can be found in table 4.8. The bearing strength is the weakest point of the laminate design. To translate the in-plane strength to an out-of-plane load, it is assumed that the laminate is infinitely stiff to create a conservative outcome. This would mean that the center load with an apparent deflection angle can be used to create an initial outcome. Assuming that the load is evenly spread between the different bolts and transforming the in-plane load into a bearing load component. This can be calculated as following:

$$P_{max} = n F_{bear} \tan(\alpha) \tag{4.2}$$

Where n is the amount of holes in the laminate and α is the angle at failure indention. With a maximum indentation angle of 15° and 12 bolts the maximum load was determined to be 7.2 kN.

Table 4.6: Applied Knockdown Factors

Material Scatter	0.8
Barely Visible Impact Damage	0.65

Table 4.7: Table with the material loads

Failure Mode	Stress MPa
σ_{Uc}	302
σ_{Ut}	150
τ_{Uc}	150

Table 4.8: Composite Specimen Failure Loads

$F_{bearing}$ [N]	$F_{NetTension}$ [N]	$F_{ShearOut}$ [N]	$F_{CornerShear}$ [N]
2220	128760	8880	36630

4.5. FIXTURE DESIGN

With the specimen design completed, a set of requirements followed to which the fixture had to comply. Based on these design requirements, a topological design was created which was structurally investigated. Two metals were investigated in the structural analysis after which a trade off followed based on weight.

4.5.1. DESIGN REQUIREMENTS

Based on the laminate design, the fixture must guide the loads of the clamp to the load cell. This meant that the starting area of the fixture must comply with the laminate design to a fixture which fits in the clamp close to the load cell.

- The fixture should be sufficiently stiff meaning that the fixture can only take up 1% of the strain energy

- The fixture should withstand at least double the expect load, 15 kN (both yield and buckle)

- The width of the beams should be twice as thick as the metric thread size in the bottom frame

- The fixture should use the maximum available height, so that the cameras can have the greatest field of view. This is 60 cm in height.

4.5.2. TOPOLOGIC DESIGN

The topological design takes shape as a pyramid was designed with four L-beams. The shape in which the beams were designed would assure fair load distribution. At the end of the beams a frame was welded to the bottom of the pyramid. This frame was then milled to assure that the plate is level. Lastly an identical frame can then clamp with the threads that are attached to pyramid fixture. The simplicity of this fixture would allow for greater tolerances. The complete fixture, with specimen, is portrayed in figure 4.3.

4.5.3. MATERIAL CHOICE AND STRUCTURAL CALCULATIONS

As a result from the topological design, one design requirement was set for the material: the material should be weldable. Materials that are weldable and sufficiently stiff would be aluminum and steel. Two alloys were selected that are commercially available are compared with one other. The properties of these alloys can be found in table 4.9. The main failure modes that were accounted for with the clamp are buckling and yielding. Yielding failure load can be defined as following:

$$F_{yield} = \sigma_{yield} A \tag{4.3}$$

Table 4.9: Properties of workplace materials

Material	Aluminum EN AW-5083L	Stainless Steel 304L
Compressive Stiffness	71.7 GPa	193 GPa
Compressive Yield Strength	125 MPa	241 MPa
Density	2660 $\frac{kg}{m^3}$	8000 $\frac{kg}{m^3}$
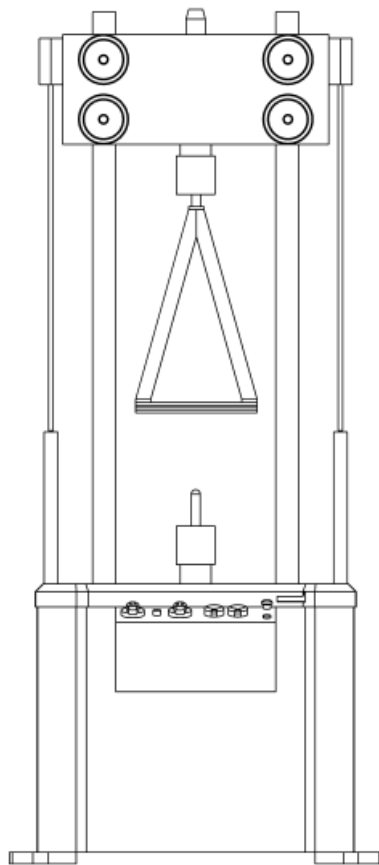
Figure 4.3: MTS 815, 100 kN machine with fixture

Table 4.10: Metric thread and Proof Load

Metric Thread 8.8	Proof Load (N)
M4	5100
M5	8230
M6	11600
M8	21200
M10	33700
M12	48900
M16	91000

Table 4.11: Properties of the fixture

Material	EN-AW-5082L
Profile	50 mm x 50 mm x 10 mm
P_{yield}	112.5 kN
P_{buckle}	188.6 kN
Weight clamp	6 kg
Load Percentage taken by clamp	0.3576%

Where A defines the surface of the profile and σ_{yield} is the compressive yield strength of the material. The buckling failure load can defined following as following:

$$P_{buck} = \frac{\pi^2 E I}{L^2} \tag{4.4}$$

Where I is the in-plane inter-polar moment, E describes the Young's Modulus and L describes the length of the beam. The geometric parameters of the L-beam were described as following:

$$A = l_{frame} b_{frame} (2 - t_{frame}) \tag{4.5a}$$

$$I = \frac{b_{frame}^3 t_{frame}}{12} + \frac{(b_{frame} - t_{frame}) t_{frame}^3}{12} \tag{4.5b}$$

Where l_{frame}, b_{frame} and t_{frame} are the length, width and thickness of the clamp frame. To determine the geometric properties , a minimum clamp thickness has to be selected. As a rule of thumb, the wall thickness of any structure should be twice as thick as the metric thread that was selected. The metric thread was selected by the desired clamp force it has to deliver. The available proof loads for the different metric threads are listed in table 4.10. The thickness of the available 'L'-profiles was the limiting factor, and M5 bolts were the biggest bolts that would comply with the rule of thumb. To assure that local stress would not destroy the clamp frame, a thickness of 10 mm was selected. To assure proper measurement of the laminate, a beam length of 635 mm was selected. This allowed the FLIR315 to measure half of the laminate. Both materials allowed for designs that can carry the load case required. The weight difference did favor the aluminum design. The minimal width of the profile was 50 mm of the aluminum profile. The calculated failure loads and design parameters are described in table 4.11.

4.6. Setup of the experiment

With the fixture and laminates designed, the last step of the experimental design is organizing the setup of the equipment. All of the considerations made here include the placement of the camera's, the manner the triggers are setup and the calibration of the equipment.

4.6.1. Setup cameras

The cameras were setup in a manner that prevents interference. The Thermographic cameras measured the heat at the bottom whereas the DIC cameras measured the strain on the top surface. In this manner interference between the optic measurements was prevented. The positions of the camera's are given in appendix B, in their respective drawings.

4.6.2. TRIGGERS

The triggers of the different cameras were connected to the software of the MTS-100kN machine. The triggers allowed synchronous measurements of the load cell (MTS-100kN) and the optical measurements. The triggers were operated by the program that is operating the tensile testing machine. The program sent a digital block signal to a relay which was connected to a voltage source. This voltage source then sent 5V DC to the thermographic camera and the DIC cameras. The thermographic camera had a set frame rate, which depends on the frequency of the heat source. The DIC camera was rearmed between individual loading steps. Before every performed test the triggers were checked to assure that the system worked accordingly.

4.6.3. DIC CALIBRATION

To calibrate the DIC setup, the cameras were aimed to the center of the laminate. The aperture of the cameras were closed to decrease the depth of field and an increased focus. This would in turn restrict the amount light entering the enter the cameras. LED lights were aimed to the measured area and tuned so that a clear focused DIC image was captured.

4.6.4. THERMOGRAPHY CALIBRATION

The thermography calibration setup was performed on either the camera and the heat source. The thermographic camera was aimed at the center of the laminate. Then temperature range was fine-tuned in the accompanying thermographic software:*ResearchIR* . The heat source was then aimed on the center of the laminate. With the support of the thermal camera, this aiming was accurate. Based on previous research [22], the frequency of the heat source was selected to track the delamination in the laminate.

$$f = \left(\frac{1.8}{p}\right)\frac{a_d}{\pi} \tag{4.6}$$

Where f is the heating frequency, p is the delamination depth of 1.25 mm and a_d is the thermal diffusion coefficient of about 0.0045 cm^2/s. With the initial heating frequency selected, the amplitude of the heat source was determined. The amplitude of the heat source was limited to not affect the mechanical properties of the laminate. The current choice for a correct amplitude is to have a peak-to-peak temperature difference of three degrees Celsius. The theoretical thermal diffusivity only gave an initial insight for the frequency. During the experiments the frequency of the heat source and measurements was altered to find the most useful setting. The tested frequencies varied between 0.05 Hz and 0.20 Hz.

5

MANUFACTURING METHOD

5.1. INTRODUCTION

With the experimental setup fully designed, the specimen were prepared for testing. Firstly the material properties and the layup design are described, to check if the specimen were compliant with the restrictions given in chapter 4. Then the manufacturing steps are described step-by-step to allow a thorough insight in the manufacturing process.

5.2. MATERIAL PROPERTIES

The selected material for the experiment was also used by previous researchers who investigated the SED criterion [3]. This material was M30SC-150-DT120-34F which is produced by Delta Tech Italy. This material is made to withstand greater transverse load-cases, which was ideal for the experiment of this research. The roll of prepreg material was 60 cm wide and 150 m long and the constitutive lamina properties are presented in table 5.1.

E_{11}	152.4 GPa
E_{22}	7.1 GPa
G_{12}	3.64 GPa
ν_{12}	0.32
ε_{ult}	2.07%
ρ	1.52 g/cm^3
t_{nom}	0.15 mm

Table 5.1: Material Properties of M30SC-150-DT120-34F [14] delivered upon request

5.3. TEST SPECIMEN DESIGN

Based from the analytical study, it was determined that the laminate was going to build up out of two quasi-isotropic layups. This laminate design required 16 layers which resulted in a thickness of 2.5 mm. This designed allowed different interfaces while it prevented extension-bending coupling. To make the system more sensitive for bending, the laminate were designed as wide as possible. Given the limitations of the prepreg-roll from which the laminate were made, while also taking the maximum width of the MTS-100 kN into account, the specimen was designed as 400mm x 400mm square. The analytical study demonstrated the effects of anisotropic bending stiffnesses will affect the delamination behavior of the specimen. The variation of bending stiffness could not be fully prevented, but was limited with the current design. To investigate if the SED criterion is independent of the load case [3], two types of test specimen were created. The laminate layups are described in table 5.2. The A-matrix ,in-plane stiffness, of the layups (table 5.3) show that no differences appear in the extension behavior the laminate. The D-matrix values, bending stiffness, of the layups (table 5.4) demonstrate the minor differences.

Name Layup	Layup
QI00	$[0, 90, -45, 45]_{2s}$
QI30	$[30, -60, -15, 75]_s // [-30, 60, -75, 15]_s$
QI45	$[45, -45, 0, 90]_s // [-45, 45, 90, 0]_s$
ORT15	$[15, 0, 0, -75]_{2s}$
ORT30	$[30, 0, 0, -60]_{2s}$

Table 5.2: All the laminate layups

A Values 10^5 [kN/m]	QI00	QI30	QI45	ORT15	ORT30
A_{11}	1.61	1.61	1.61	2.85	2.64
A_{12}	0.481	0.481	0.481	0.16	0.37
A_{16}	0	0	0	0.19	0.19
A_{22}	1.61	1.61	1.61	1.01	0.80
A_{26}	0	0	0	0.19	0.19
A_{66}	0.57	0.57	0.57	0.24	0.46

Table 5.3: All the A-matrix values of the various layups

5.4. MANUFACTURING METHOD

The manufacturing plan was separated in the various processing steps. First the a base plate was picked and adequately cleaned. Then the laminas were cut in the most efficient manner to save material. The laminate was build up and debulked after which it was cured in the the autoclave. The required materials for manufacturing are reported in table 5.5.

5.4.1. PREPARING BASE PLATE

The selected mold plate allowed production of two specimens at once. The plate was 1500 mm x 800 mm in size and 20 mm thickness. This thickness was required to withstand the pressure during the curing cycle.Before cleaning the mold plate all the remaining resin, tacky tape and other materials was removed. Then the mold plate was rinsed three times with acetone. The last step of preparing the mold plate was applying Marbocoat to the plate as release layer. Marbocoat allowed for easy removal of the laminate at the end of production. The Marbocoat was not applied on the edges of the mold plate, because tacky tape had to stick at edges for sealing the vacuum bag. Crepe tape was applied at the sides of the mold plate , see figure 5.1, to remain the sides with a coating layer.

5.4.2. CUTTING THE LAMINAS

A cutting table with grid was used to assure accurate lamina cuts. A cutting tool was applied to easily cut the lamina in the desired sizes. A 3mm thick steel plate, which had the same dimensions as the desired lamina area, was used to cut the laminas in the right orientation. A set of angles for the top two corners was drawn on the tool to assure consistent cuts, see figure 5.2. A checklist was created to assure that the correct number of laminas were cut.

D Values [Nm]	QI00	QI30	QI45	ORT15	ORT30
D_{11}	94.55	84.93	87.82	157.33	140.77
D_{12}	20.79	27.04	20.79	8.55	20.18
D_{16}	1.12	0.56	0	13.44	15.90
D_{22}	81.09	78.20	87.82	42.78	36.07
D_{26}	1.12	0.56	0	6.71	4.24
D_{66}	25.18	31.43	25.18	12.94	24.57

Table 5.4: All the D-matrix values of the various layups

Figure 5.1: The mold plate ready to be coated.
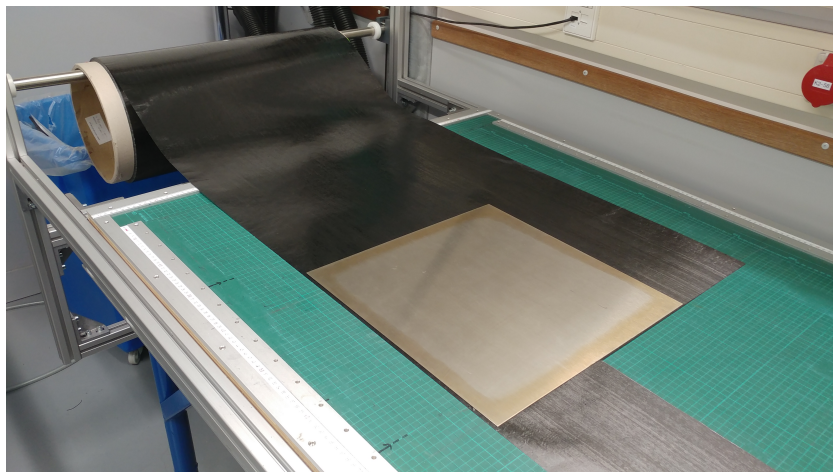
Figure 5.2: The cutting mold on top of prepreg roll.

Material	Quantity
Teflon Inserts	1 / laminate
M30SC-120DT-34F	7.8m/laminate
Vacuum Foil	Depends on mold plate size
Non-perforated release film	390mm x 390 mm / laminate
Peelply	Depends on mold plate size
Heavy Breather	Depends on mold plate size
Debulking Plastic	Depends on mold plate size (reuseable)
Vacuum Nipple	1/mold plate (reuseable)
Measuring Tape	1
Stanley Knife	1

Table 5.5: Required Materials
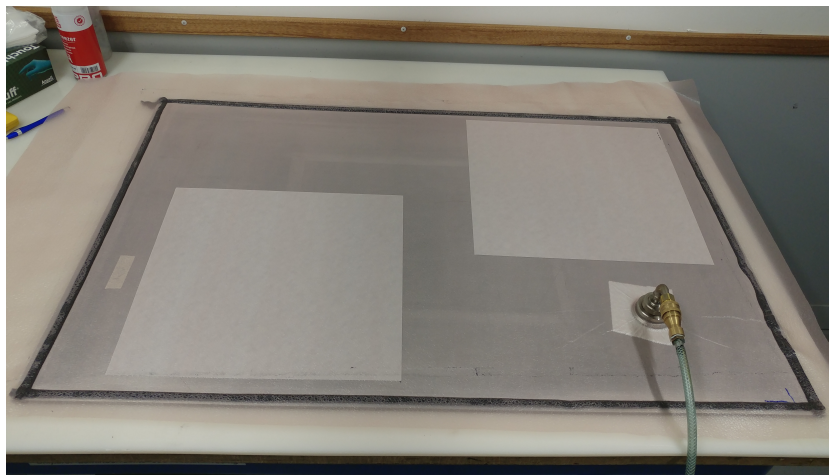
Figure 5.3: Debulking of the initial layer.

5.4.3. Building up the laminate and debulking

The prepreg has to be debulked when building up the laminate. A line of tacky tape was applied around the sides of the mold plate and debulking plastic was placed on top of the build laminas when the debulking steps started. The initial layer was directly debulked so that layer stuck on the plate. The prepreg film was kept on top of the initial lamina to prevent that the layer would stick to the debulking plastic. A hole was cut in the debulking plastic for the vacuum fitting. A small layer of breather material was placed under the vacuum fitting to allow for well distributed vacuum pressure. Then vacuum was applied for 1 minute. The complete debulking setup is illustrated in figure 5.3. After debulking the initial layer, the release film was removed and the next three layers were build up on top at once. For the second debulking step, the release film was removed from the top lamina. No more than three layers were debulked at once. After 8 layers, the Teflon insert was placed in the center of the laminate. As demonstrated in figure 5.4 , two rulers were used for the positioning of the Teflon insert.

5.4.4. Vacuum Bag and Autoclave

The complete debulking material and the tacky tape was removed. A new layer of tacky tape was applied to the sides of the mold plate. First the non-perforated release film was cut slightly smaller than the area of the laminate. A layer of breather material and vacuum foil was cut. The breather layer was cut to match the area of the plate between the tacky tape sides. The vacuum foil was cut bigger than the mold plate. A corner was drawn on the vacuum foil at the edge mold plate to indicate the location of the vacuum fitting cut out. The build up of the vacuum bag was in the following order from the laminate, 1) non-perforated release film, 2) peel-ply, 3) breather material, vacuum nipple + vacuum foil. This build up is visualized in figure 5.5. The vacuum foil was cut to match the mold plate and the sides of the vacuum foil were taped with sealant tape. Now the mold plate with vacuum bag can be placed in the autoclave, the cycles for the autoclave can be found in figure 5.6. The vacuum bag is placed under a vacuum in the autoclave during the whole curing process.
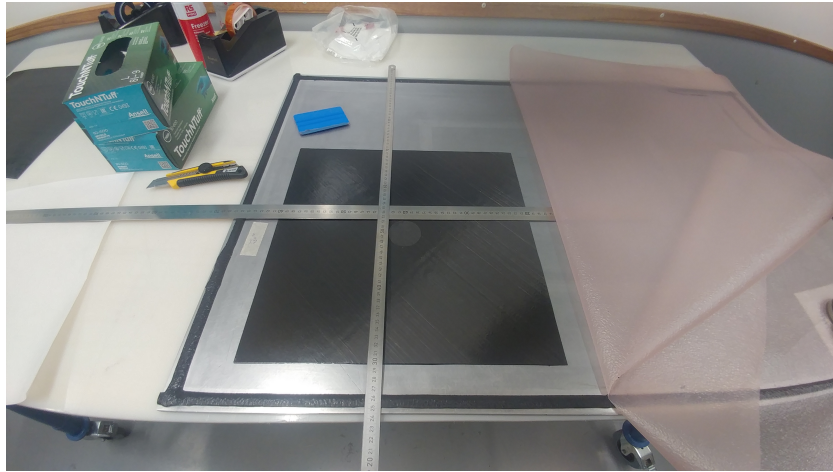
Figure 5.4: Placing the Teflon insert in the center.
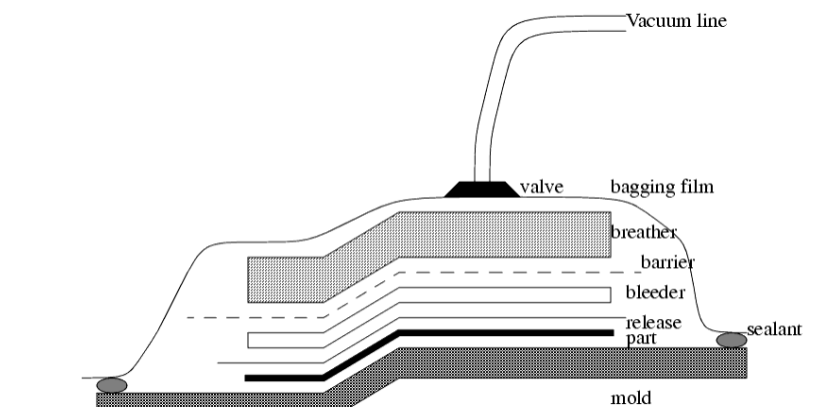
Figure 5.5: Build up of the vacuum bag.
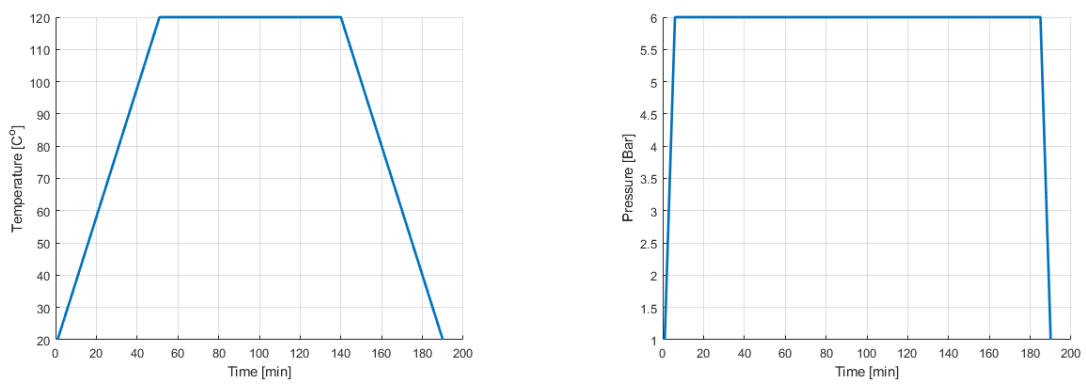
Figure 5.6: The autoclave cure cycle a) Temperature Cycle, b) Pressure Cycle
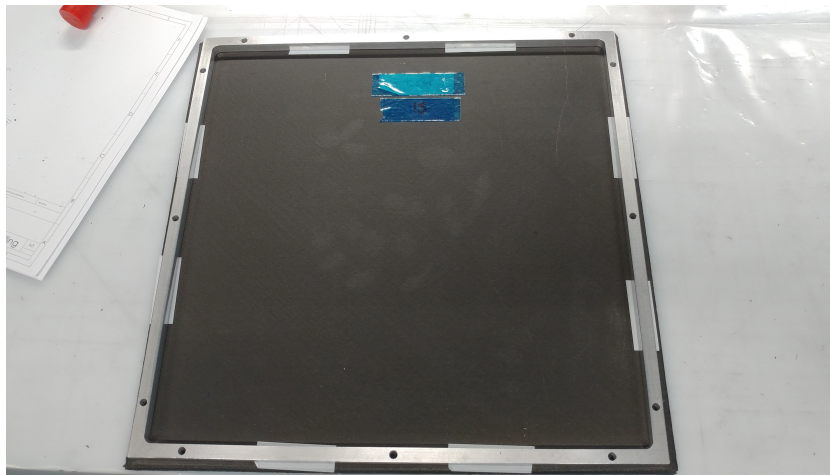
Figure 5.7: Double Tape Bottom Clamp Frame on Composite Specimen

5.5. C-SCANNING THE LAMINATES

To assure that the only initial defect in the laminate was the delamination insert at the center of the laminate, a C-scan was performed. The c-scan measurement technique can easily find pores within a composite material, however smaller damages might be missed. To make completely sure that no other defects were in the material, a reference material was used as comparison. The c-scan will also revealed the location of the delamination insert. All of the C-scans were made at GTM Advanced Structures. The C-scan results are reported in appendix A.

5.6. DRILLING LAMINATES FOR THE CLAMP

The last step in preparing the laminates for the tests was drilling holes to place the laminates in the fixture. Since the clamp frame was a flat structure, see appendix B , the laminate could be taped to the clamp frame with double-sided tape, see figure 5.7. This method assured that the composite specimen would fit in the clamp. The holes were directly drilled in the composite laminate with a 5.5 mm diameter SPF drill. The applied drill spindle speed was 650 rpm. The drill feed was not measured, but drilling was performed as slow as possible to minimize delaminations at the hole edges. After trying out the first specimens with the clamp, it was noted that pretension is apparent in the laminates due to the alignment errors of the threads on the clamp. For this reason, the laminate holes were extended with a step drill of 6 mm. The same drill spindle speed was applied.

<div style="text-align: right;">

6

</div>

QUASI STATIC TESTS

6.1. INTRODUCTION

To test the hypothesis of the planar delamination problem, an initial set of quasi-static tests were performed. The purpose of these quasi-static tests were to investigate an applicable methodology to determine the SERR in planar delamination tests. While the determination of the strain energy induced laminate has been calculated with the load-displacement behavior, the determination of the delamination area has been performed with 3 different methods: 1) thermography, 2) curvature and 3) the strain energy density criterion measured with DIC. The test outcomes were firstly investigated with a statistical analysis, then the different area determination methods were compared, and set of best practices was recommended.

6.2. EXPERIMENTAL PROCEDURE

The quasi static tests had some conditions that were universal for all the tests. These are the following:

- The laminates dimensions were 400mm x 400m x 2.50 mm

- The humidity in the laboratory was $65 \pm 5\%$

- The temperature in the laboratory was $20.5 \pm 0.5C^o$

- The displacement rate of the quasi-static tests was 1 mm/min

The experimental setup was build up out of multiple components as described in figure 6.1. For the DIC cameras the settings were automatically calibrated for any speckle pattern after an initial calibration. The infrared camera required a single calibration to make sure that the focus was on the composite specimen. The heat source had two variables that required calibration, the settings are given in the test matrix (table 6.1). Lastly the clamp load was applied with a torque wrench, which had a sensitivity of 6% for the measured torque. The DIC cameras and the thermography cameras started capturing data once the universal testing machine gave a trigger signal. The thermography camera captured an image every second, whereas the DIC image captured an image every ten seconds.

The test purpose of the planar ELS specimen was to determine the repeatability of the test. The complete statistical analysis of the ELS specimen is described in subsection 6.3. The test purpose of the planar SCB specimen was to compare the quasi-static outcomes with the SCB specimen that were tested in the fatigue tests. The last type of specimen that was tested in the quasi-static test setup is the quarter plate, specimen 14 in the test matrix. This test was performed to see the applicability of the setup for measuring multi-layer damage experiments, similar to the experiment by McElroy [81].
To determine the right test settings for measuring the delamination an initial specimen was loaded with a torque and frequency that was estimated to be close to the right settings. From this initial test it was noted that the clamping torque required to be increased, since the clamp frames displaced too much with the specimen. It can be seen in the test matrix that the settings for the thermographic measurements were altered between the tests. This was done because no clear results could be obtained with the lock-in thermography. More insights regarding the lock-in thermography measurements can be read in subsection 6.4.3.
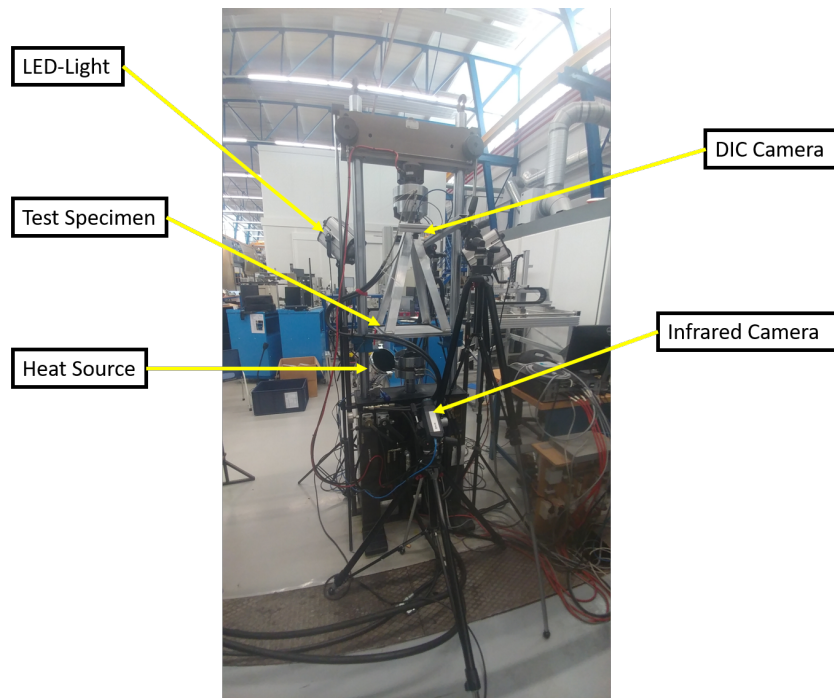
Figure 6.1: Setup of the Experimental Setup for both the Quasi Static and Fatigue Tests

Table 6.1: Test Matrix Quasi Static Tests, values with * are critical displacements

Specimen	Layup	Indenter (mm)	final δ (mm)	Frequency Heat Source (Hz)	Vpp (V)	Specimen Type
2	QI30	15	21.39*	0.02	6.5	ELS
19	QI45	15	21.17	0.0125	4.5	ELS
3	QI30	15	20.68	0.0125	5.5	ELS
5	QI30	15	21.19	0.0125	5.5	ELS
7	QI30	15	19.19	0.0125	5.5	ELS
20	ORT30	15	21.16	0.0125	5.5	ELS
21	ORT15	15	23.01	0.0125	5.5	ELS
9	QI00	15	19.7996	0.125	5.5	SCB
10	QI00	15	0.37	0.125	5.5	ELS
12	QI00	15	19.87*	0.125	5.5	ELS
15	QI45	15	20.32*	0.125	5.5	ELS
1	QI30	40/30	20.52*	0.125	5.5	SCB
8	QI00	20/30/40	19.25*	0.125	5.5	SCB
13	QI45	30	20.70	0.125	5.5	ELS
16	QI45	30	21.25	0.125*	5.5	SCB
14	QI45	40	62.501	0	0	4th
6	QI30	0	0	0	0	ELS

(a) Quasi Static ELS 0//0 Specimen

(b) Quasi Static ELS 30//-30 Specimen

(c) Quasi Static ELS 45//-45 Specimen
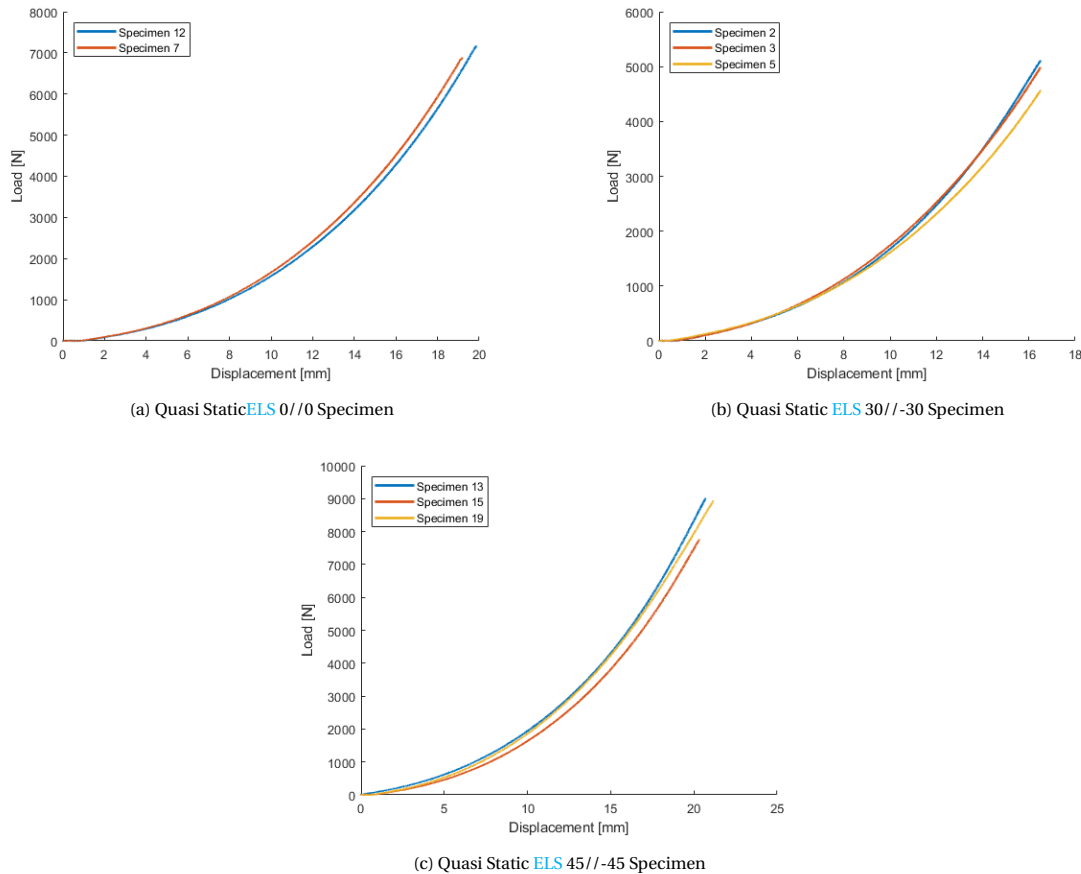
Figure 6.2: The Load Displacement graphs of the different quasi static ELS tests

6.3. STATISTICAL ANALYSIS

The first step into verifying the outcomes of the experiment was to perform a statistical analysis. Since the delamination growth was limited in the quasi-static tests, the analysis investigates the precision and bias of the induced strain energy. This was determined by the load-displacement measurements which are illustrated in figure 6.2. For the statistical analysis, only the ELS specimens were investigated, since for this type of specimen multiple tests have been performed. The load-displacement behavior was non-linear, which means that direct linear approximation will not give reasonable results. To determine strain energy, an integration scheme was applied to the results which is illustrated in figure 6.3. Every integration step approximates the strain energy by applying two shapes: 1) the block of initial load in the step and the change of displacement and 2) the quadratic growth of the load in the step. Adding up the strain energy of all the integration steps resulted in the complete strain energy. The comparison of the strain energy required a fixed maximum displacement. The displacement at which the strain energy is measured is 16.5 mm, since this is the maximum displacement of fatigue tests in chapter 7. The strain energy of the quasi-static tests was also compared with the fatigue data. The outcomes of the statistical analysis was summarized in table 6.2. With the mean and standard deviation values of the tests, normal distribution graphs can be created, see figure 6.4. The coefficient of variance of the test outcomes is relatively small with a maximum of 8.12%, when compared with a DCB test which can have a coefficient of variance greater than 10% [1]. Comparing the strain energy of this test with the SERR was performed gain an initial indication on the repeatability of the test. The number of measurements is relatively small so these results only serve as an initial indication. Following the ASTM standard for precision [82], an estimate was made for the number of tests required to gain an error margin smaller than 5%. First the initial standard deviation was used to calculate the advanced estimate σ_0.

$$\sigma_0 = \frac{\bar{s}}{c_4} \qquad (6.1)$$

$$U_n = P_1(\delta_2 - \delta_1) + 1/3(P_2 - P_1)(\delta_2 - \delta_1)$$
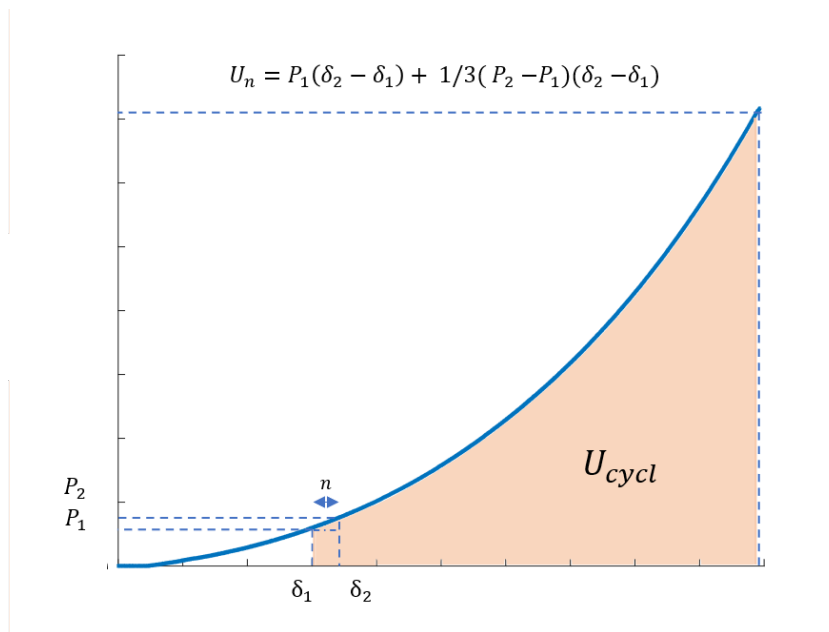
Figure 6.3: The step based calculation for determining the strain energy

Table 6.2: Statistical outcomes of the ELS Quasi Static Tests up to Displacement 16.5 mm

Laminate	Mean (J)	StD (J)	95% Confidence Limit (J)	CoV %	Performed tests	σ_0 (J)	Samples required
QI00	25.046	0.973	1.908	3.89	2	1.2169	9
QI30	26.042	1.068	2.094	4.10	3	1.2019	8
QI45	27.770	2.256	4.422	8.12	3	2.5380	30

Where $\bar{s}$ is the measured standard deviation and c_4 is the correction factor for the selected sample size. c_4 was calculated as following.

$$c_4 = \frac{n-1}{n-0.75} \tag{6.2}$$

Where n is the tested sample size. The required sample size was determined by the ASTM standard [82], which applied the following function for a normal distribution to determine the required sample size.

$$n_{req} = \left(\frac{3\sigma_0}{E}\right)^2 \tag{6.3}$$

In this function E is the maximum allowable error of the measurements. In table 6.2 the calculated required sample size was calculated with a maximum allowable error of 5% compared to the mean.

6.4. COMPARISON DELAMINATION MEASUREMENT METHODS

To measure the delamination in the planar specimen, three different methods have been performed: 1) bond state mapping with the SED criterion, 2) XY-Plane Curvature measurements and 3) the heat dissipation analyzed with lock-in thermography. The outcomes of these different delamination measurements were then qualitatively compared.
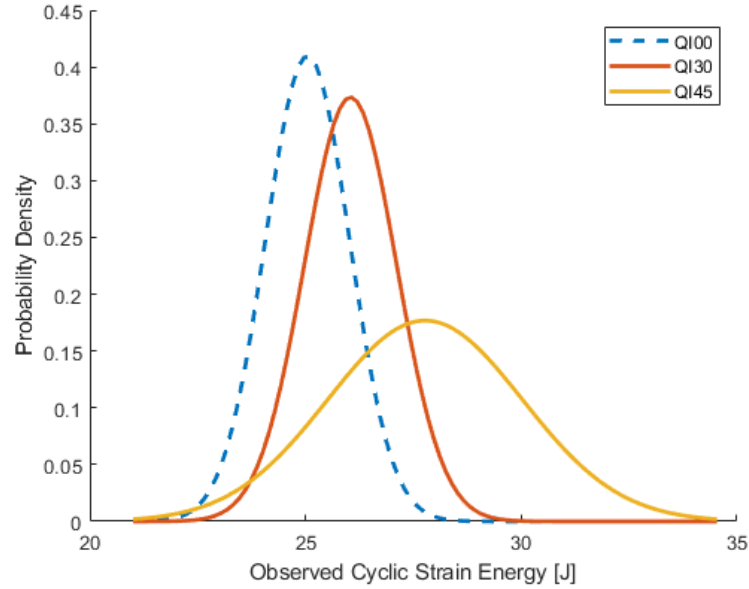
Figure 6.4: Normal Distributions of the Different ELS Specimen

6.4.1. DETERMINING DELAMINATION SIZE WITH DIC SED DATA

To derive the SED of specimen, the measured strains on the top of the surface were required to calculate to the mid-plane strains as following.

$$\varepsilon_{x0} = \varepsilon_{xtop} - \frac{h}{2}\kappa_x \tag{6.4a}$$

$$\varepsilon_{y0} = \varepsilon_{ytop} - \frac{h}{2}\kappa_y \tag{6.4b}$$

$$\gamma_{xy0} = \gamma_{xytop} - \frac{h}{2}\kappa_{xy} \tag{6.4c}$$

With the mid-plane strains derived, the average SED over the thickness of the laminate was calculated by applying CLT. This required the constituent properties of the material (table 5.3 and 5.4).

$$
\begin{aligned}
u_\rho = \frac{1}{2}\Big(&A_{11}\left(\varepsilon_{x0}\right)^2 + 2A_{12}\left(\varepsilon_{x0}\varepsilon_{y0}\right) + 2A_{16}\left(\varepsilon_{x0}\gamma_{xy0}\right) + A_{22}\left(\varepsilon_{y0}\right)^2 + 2A_{26}\left(\varepsilon_{y0}\gamma_{xy0}\right) + A_{66}\left(\gamma_{xy0}\right)^2\Big) \\
&+ \frac{1}{2}\Big(D_{11}\kappa_x^2 + 2D_{12}\kappa_x\kappa_y + 2D_{16}\kappa_x\kappa_{xy} + D_{22}\kappa_y^2 + 2D_{26}\kappa_y\kappa_{xy} + D_{66}\kappa_{xy}^2\Big)
\end{aligned}
\tag{6.5}
$$

Since there is no difference in thickness between the laminates, this normalized SED is fair enough for comparison between the laminates. The generated SED contour maps are presented in the figures 6.5,6.6 and 6.7. The initial delamination shapes cannot be found with the pure SED maps, but the patterns do demonstrate circular contours, with an exception of specimen 9,2 and 15 which were tested until their critical displacements. The SED graphs of the specimens at critical displacement demonstrated the redistribution of SED when the delamination expands. Seeing these changes by expansion demonstrated the capabilities of this method to track the delamination.

6.4.2. XY-PLANE CURVATURE DATA

The curvature data was calculated by the DIC software (*VIC3D*) with an averaging filter. The standard setting for the filter is to average over 15 frames. The outcomes of the xy-plane curvatures in the field of interest are illustrated in figure 6.8,6.9,6.10 and 6.11. The delamination was spotted by the sudden change of the xy-plane curvature. By comparing the delaminations with the white length bar, which was measured to be 10 mm, the initial delamination size of 50 mm was determined from the xy-plane curvature fields.

(a) Specimen 9

(b) Specimen 10
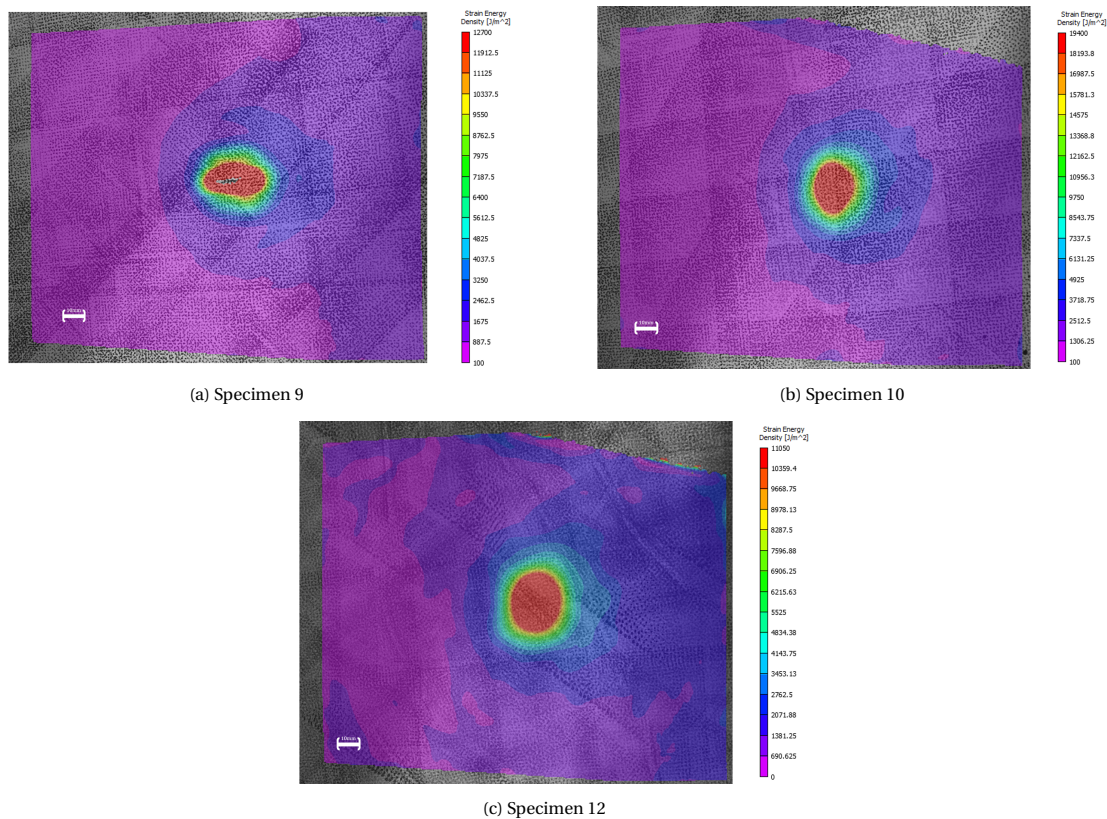
(c) Specimen 12

Figure 6.5: The SED field measurements of the ELS 0//0 Specimen at the maximum center displacement of the test

6.4.3. LOCK-IN THERMOGRAPHY

In chapter 4 thermography was proposed as potential method to measure the delamination behavior. The infrared camera was able to capture the moments when delamination occurs, which is illustrated in figure 6.12a. It was also able to spot the local failure of the planar SCB specimen, illustrated in figure 6.12b. The phase-array filter did not yield outcomes that measured the delamination size. While the phase filter was applied correctly with the applied frequency (0.125 Hz), the phase filter only returned noise during the whole process. While the technique of thermography was used to measure delamination behavior [22], more research is required to find the right settings for this measurement technique in this setup. The data of the thermographic measurements was saved and will be published for future research.

6.5. ADDITIONAL FINDINGS

During the quasi-static tests unexpected obstacles were faced and all the additional findings are reported in this section. These findings contribute to potential practical solutions for further investigation of the planar delamination behavior but deviated from the original research goal. The following topics have been further investigated: 1) the reason why delamination barely occurs in these quasi-static tests, 2) investigation on the specific radius of the indenter that was able to induce delamination in the SCB test and 3) the reproduction of the quarter plate test [81].

6.5.1. LIMITED DELAMINATION GROWTH

At a maximum load of 12 kN, most of the laminates did not delaminate in the quasi-static tests. For quasi-isotropic laminates, an onset load was derived based on the maximum interlaminar shear stress criterion[9]. Specimens that were investigated in the research for the onset load approximation[9] are circular quasi-isotropic discs, the method gave insight on the required onset load for delamination expansion. The approximation method assumed that transverse shear stress decays with a rate of $P/2\pi r t$ once the transverse peak stress is reached which is illustrated in figure 6.13. This means that the average transverse shear stress is about 1.5 times smaller than the maximum transverse shear stress. By combining these two assumptions the

(a) Specimen 2

(b) Specimen 3
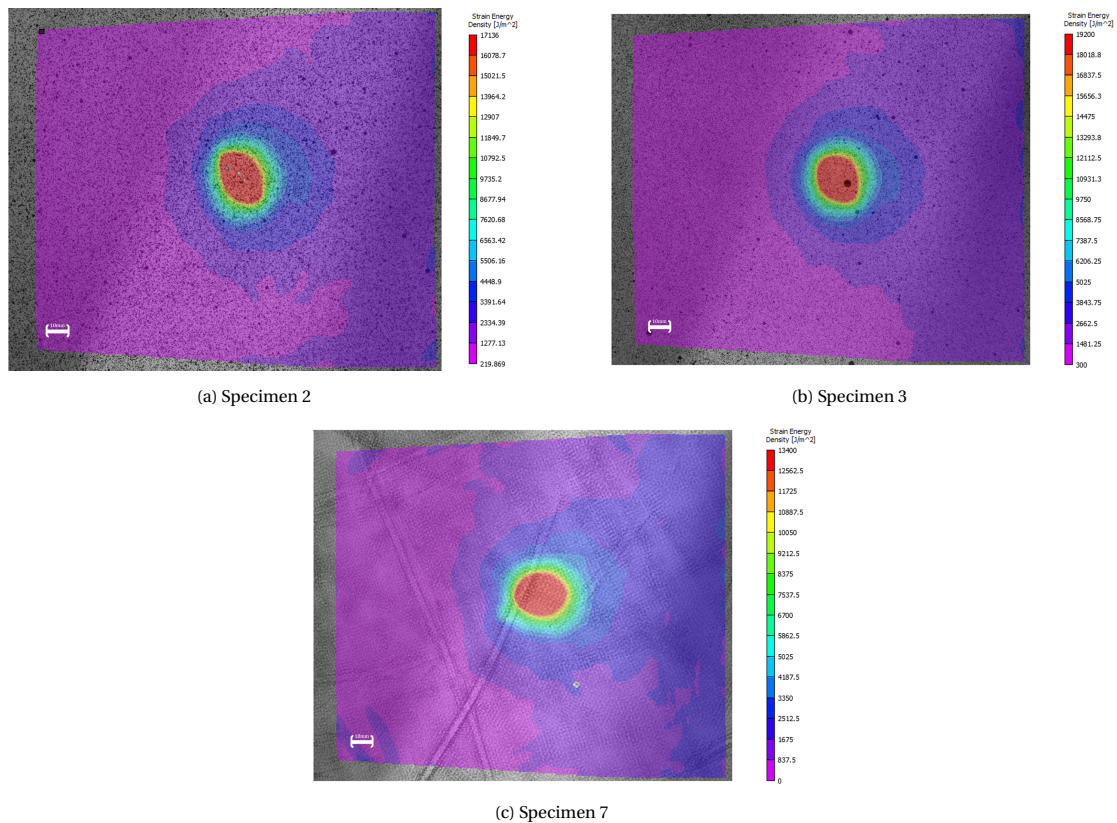
(c) Specimen 7

Figure 6.6: The SED field measurements of the ELS 30//-30 Specimen at the maximum center displacement of the test

critical load for the delamination growth in a laminate can be derived to be the following:

$$P_{crit} = A_{delam}\tau_{avg} = (2\pi a_0 t)\frac{\tau_u}{1.5} \tag{6.6}$$

With the initial delamination radius of 25 mm, thickness of the plate of 2.50 mm and a maximum interlaminar shear stress of 78.33 MPa the onset load was determined to be 20.5 kN. This load was twice as great as the anticipated load for which the test setup was designed. The clamping frame would experience plastic deformation and potentially failure when this load would be induced in future tests. The composite plates that were designed would experience fracture before the delamination expansion that would occur.

While this approximation was been fully proven, since the load of 20.5 kN was reach in the test, it would is recommended to further investigate influence of the delamination size on the delamination behavior of planar specimen. With this current setup a maximum initial delamination radius would be recommended to be 12.5 mm, which would correspond with an onset load of 11 kN which is close to the critical transverse load of the specimen.

6.5.2. Indenter Radius Analysis
With the SCB specimen, the first test caused local failure was with specimen 9. The local failure was the indenter penetrating the SCB specimen. To prevent such failure in future tests, the influence of the indenter radii was investigated. The indenters that were tested had a radius of 10 mm, 15 mm, and 20 mm. The 10 mm radius indenter demonstrated similar behavior to the initial 7.5 mm radius and was not further investigated after an initial test with specimen 8 (QI00). The 15 mm radius indenter could induce a small amount of delamination at 11 kN in specimen 8. This is at a load lower than the onset load predicted with the interlaminar shear stress approximation mentioned in subsection 6.5.1. To see if a thicker indenter could expand the delamination even further in specimen 8, a test was performed with the 20 mm indenter. The delamination did not expand further with the thicker indenter.

It became of interest to investigate if the delamination onset load would be lower with a thicker indenter. A test run was performed with the 20 mm indenter and specimen 1(QI30). At a load of 13 kN, the thicker indenter was not able to expand the delamination. To investigate if the smaller onset load was a material property

(a) Specimen 13

(b) Specimen 15
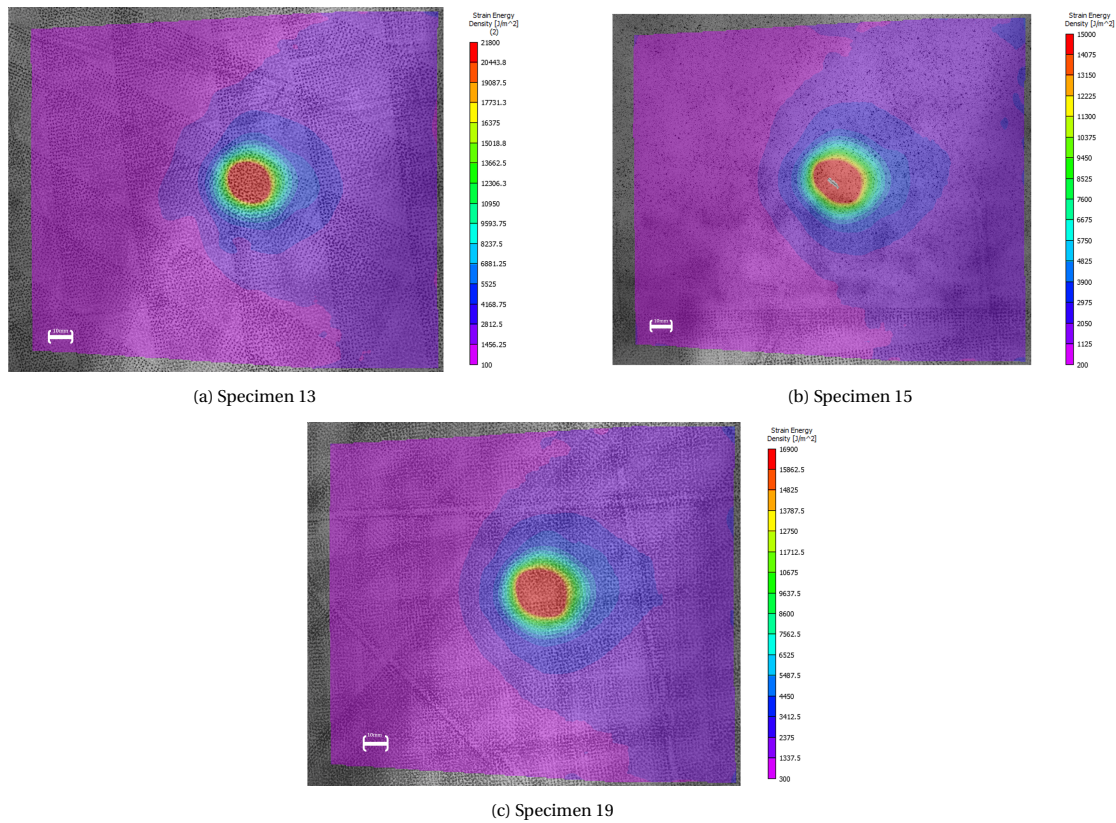
(c) Specimen 19

Figure 6.7: The SED field measurements of the ELS -45//45 Specimen at the maximum center displacement of the test

(a) Specimen 7
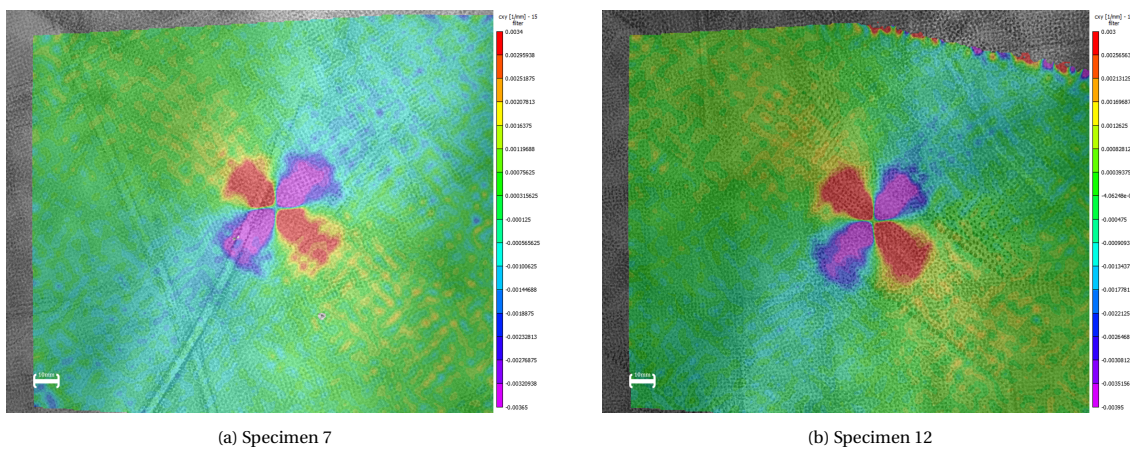
(b) Specimen 12

Figure 6.8: The curvature field measurements of the ELS 00//00 Specimen at a center displacement of 20 mm

or if it was caused by the indenter radius, the 15 mm radius indenter was tested with specimen 1 as well. At a similar load to specimen 8, the delamination expanded in specimen 1 with indenter radius of 15 mm. The SED field maps and the c-scans of specimen 1 and 8 show the delamination growth caused by the 15 mm indenter in figure 6.14. The lower delamination onset load was either caused with the indenter of 30 mm or due to the initial loading of specimen.

To figure out why this specific indenter size would cause delaminations, the delamination criteria data was extracted for specimen 1 and 8 from a line that crosses the delamination boundary in the direction of the delamination growth of specimen 1. The in-plane radius of the end point of the extracted line from the indenter was 69mm, which is a range that should measure all significant effects that can cause the delamination at a lower onset load. The results of this data extraction (figure 6.15) showed no significant difference between the 15mm and 20 mm radius indenter for the SED , xy-plane curvature and the in-plane shear stress of the

(a) Specimen 2

(b) Specimen 3
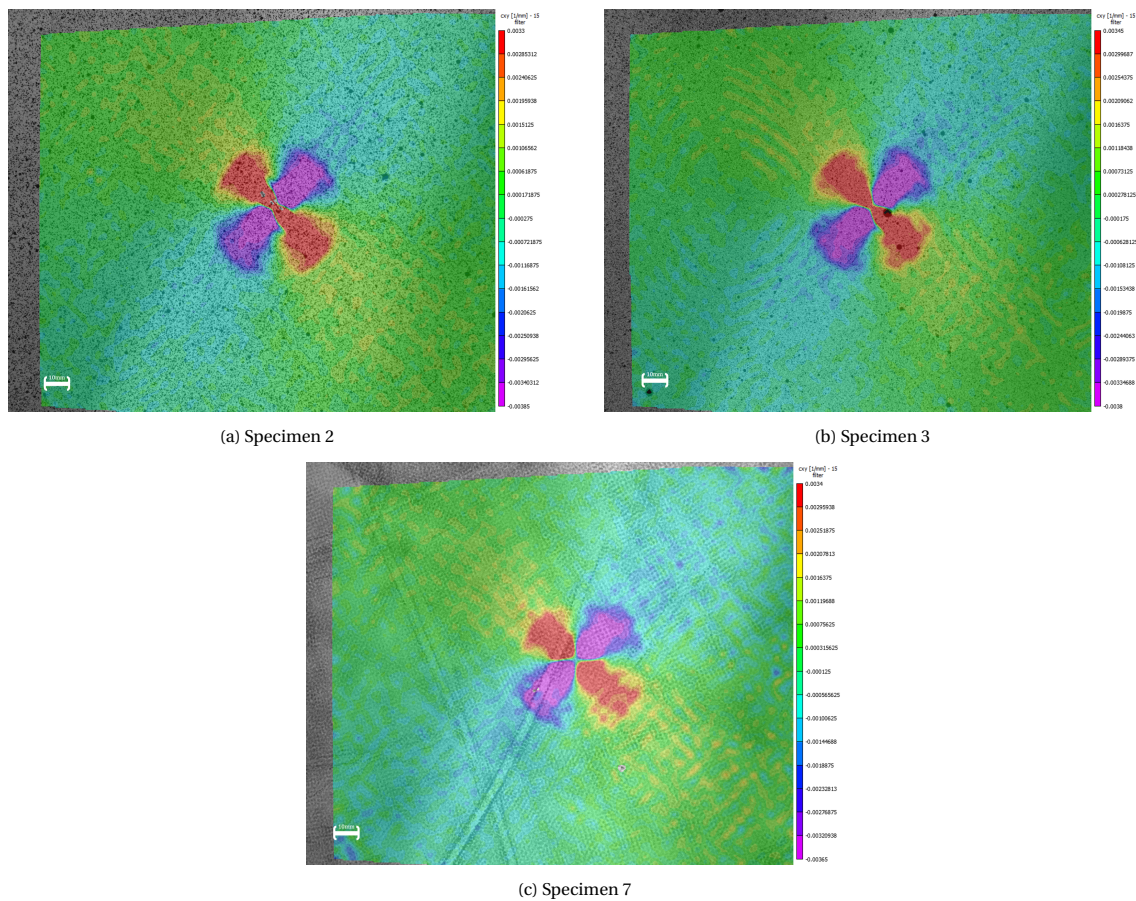
(c) Specimen 7

Figure 6.9: The curvature field measurements of the ELS 30//-30 Specimen at a center displacement of 20 mm

laminate.

The curvature is the only variable that demonstrates that the 30 mm diameter indenter would cause the delamination to grow. It was interesting that this behavior was not captured by the SED. It is recommended to explore this indenter radius effect further.

6.5.3. QUARTER PLATE

The quarter plate test was performed to investigate the applicability of the DIC methodology on the test settings designed by McElroy [81]. In their original test setup, the out-of-plane curvature was measured with the laser-reflection measurement and the delamination size was measured after the experiment with tomography. The purpose of the original test was to investigate the multi-layer delamination behavior in a plate. The outcomes of the DIC measurements and C-scan are illustrated in figure 6.16. While the DIC methodology can track the delamination, the delamination behavior was unstable and rapid. Since only a single measurement was made of the extended delamination no insights could be given on the delamination propagation behavior. The test setup tracked the delamination growth without removing the specimen out of the test setup, but delivered limited information on how the delamination jumped between different layers. Crack jumping was the primary focus of McElroy [83].

6.6. CONCLUSION

The test setup has demonstrated repeatability. The statistical analysis of the planar ELS specimen showed that the test setup demonstrates repeatable behavior. With the limited number of tests, two or three samples of each layup, a coefficient of variance is measured that is smaller than the DCB test. To gain an error margin of less than 5% with the strain energy measurements, it was calculated that about 8 tests would need to be performed,

There are improvements to be made to the current experimental design. The delamination size of the test

(a) Specimen 13

(b) Specimen 15
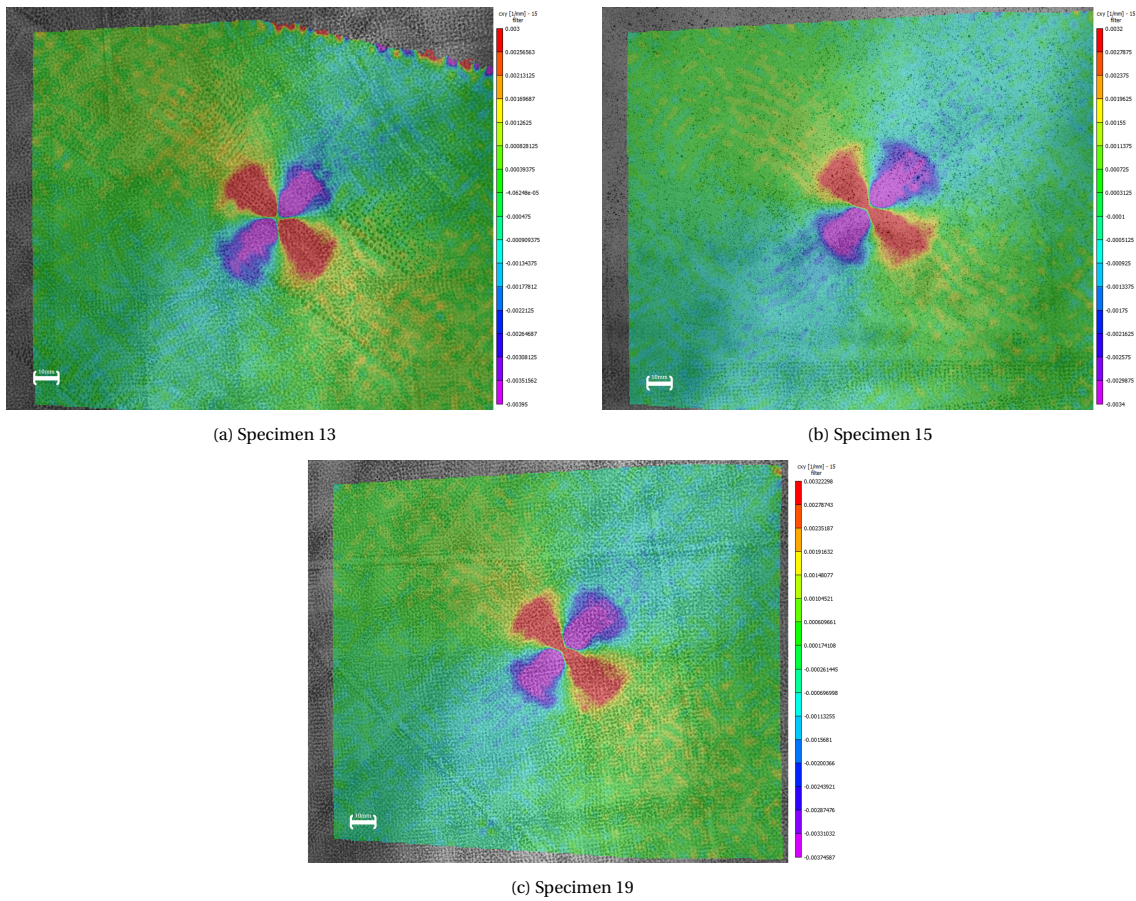
(c) Specimen 19

Figure 6.10: The curvature field measurements of the ELS -45//45 Specimen at a center displacement of 20 mm

(a) Specimen 20: ORT30

(b) Specimen 21: ORT45
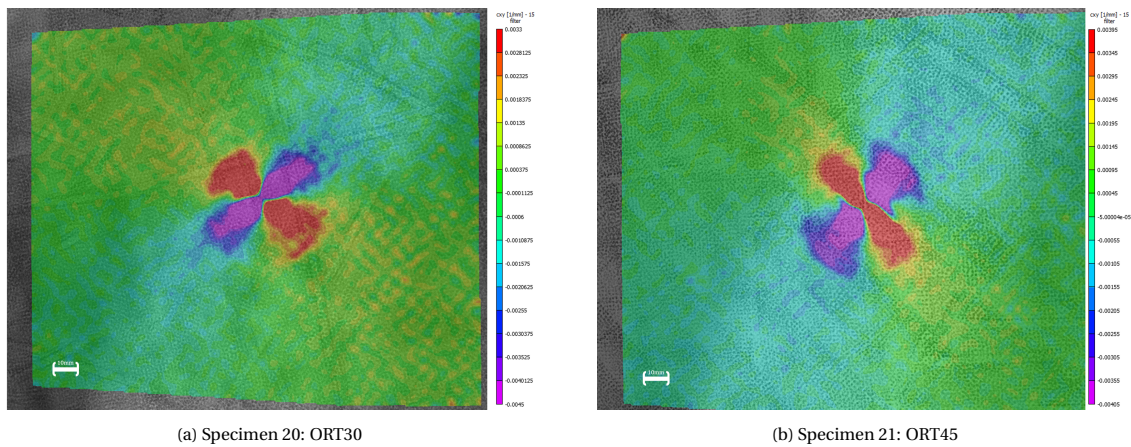
Figure 6.11: The curvature field measurements of the ELS Orthotropic Specimen at a center displacement of 20 mm

specimen should be sufficiently small, maximum radius of 12.5mm, which was approximated with the maximum shear stress criterion given in equation 6.6. New clamping frames should be produced which are both wider and thicker, to allow for greater load induction and more accurate clamping conditions. The current quasi-static tests can only be used for critical displacement determination and not for the measurement of the SERR due to the limited delamination growth in a single cycle in this setup. The SCB specimen seems to be more promising for future quasi-static delamination tests, due to the actual delamination crack growth in specimen 1 and 8.

The thermography methodology required more insight in fine-tuning the settings with the frequency-controlled

(a) Specimen 2: Delamination growth

(b) Specimen 9: Local Failure
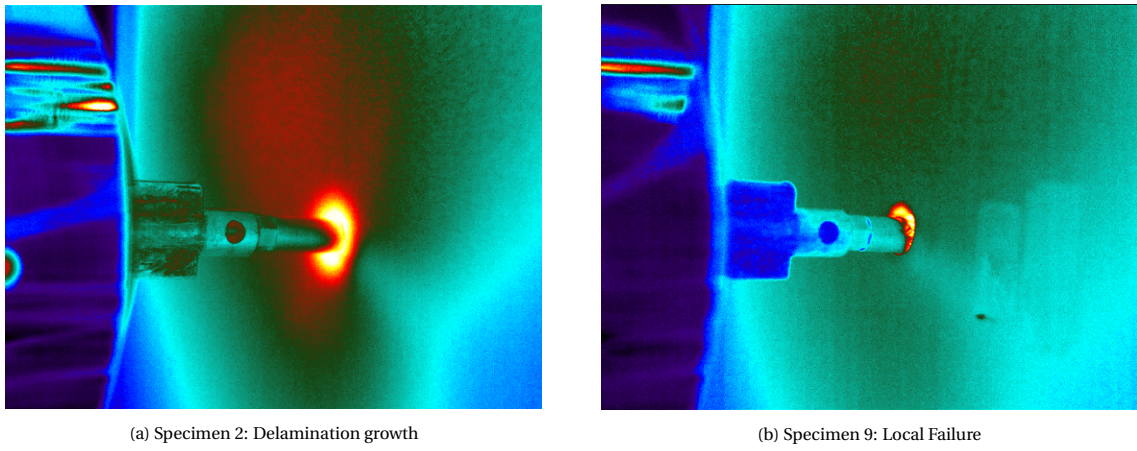
Figure 6.12: Infrared measurements at delamination and at local failure
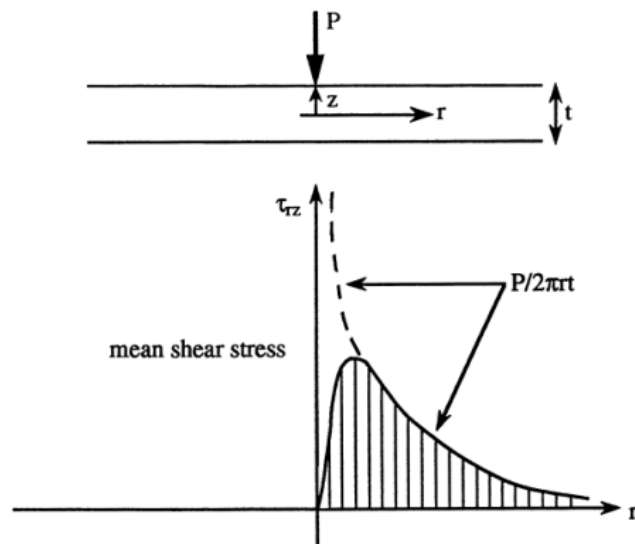
Figure 6.13: Variations in mean shear stress in the radial direction [9]

(a) Specimen 1: SED field measurement of the test with indenter radius 15 mm

(b) Specimen 1: C-scan

(c) Specimen 8: SED field measurement of the test with indenter radius 15 mm

(d) Specimen 8: C-scan
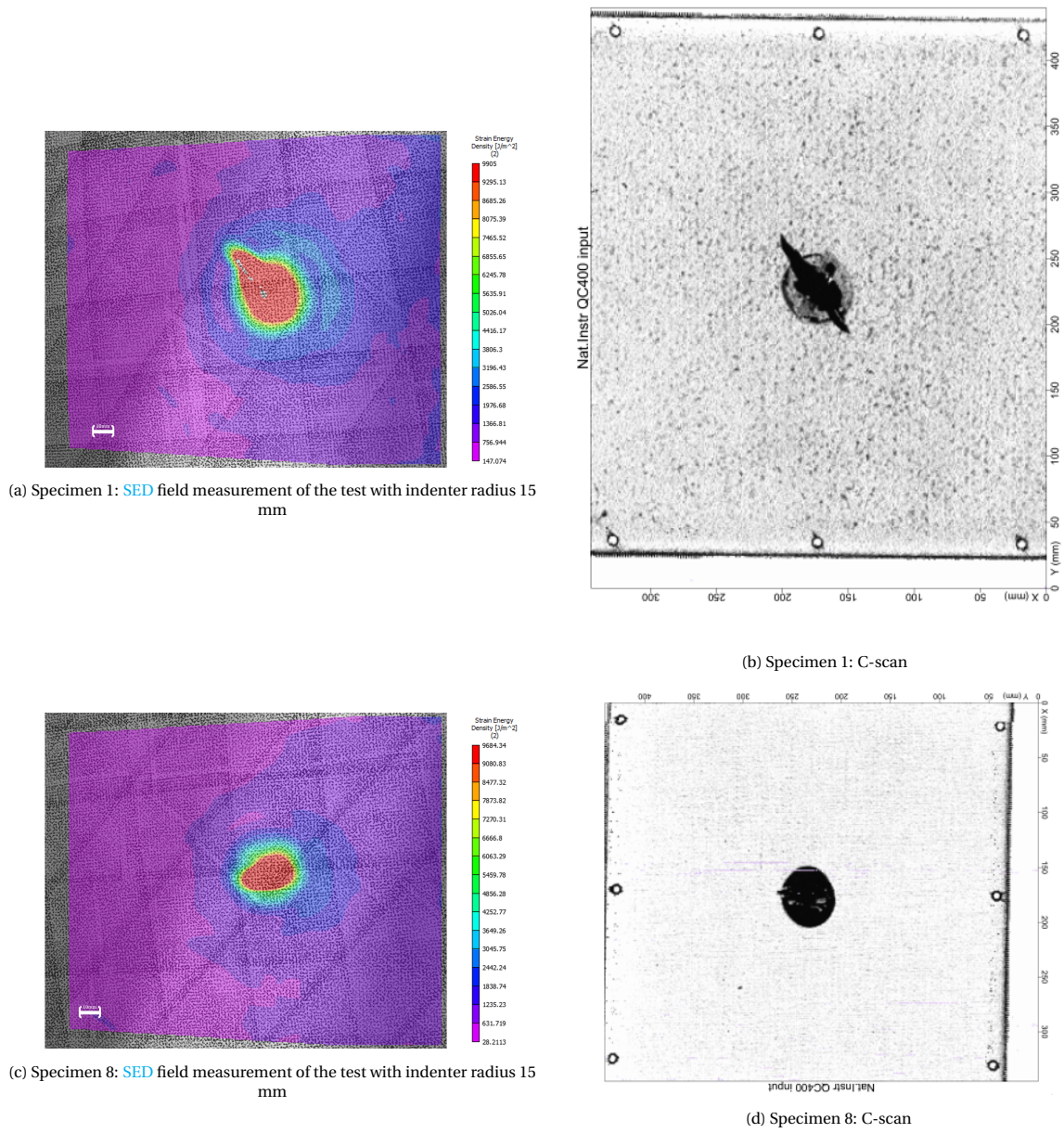
Figure 6.14: The C-scans and SED field measurements of the delaminated quasi-static planar SCB specimen

(a) The XY-Plane curvature in the radial coordinate system

(b) The SED in the radial coordinate system

(c) The in-plane shear stress in the radial coordinate system
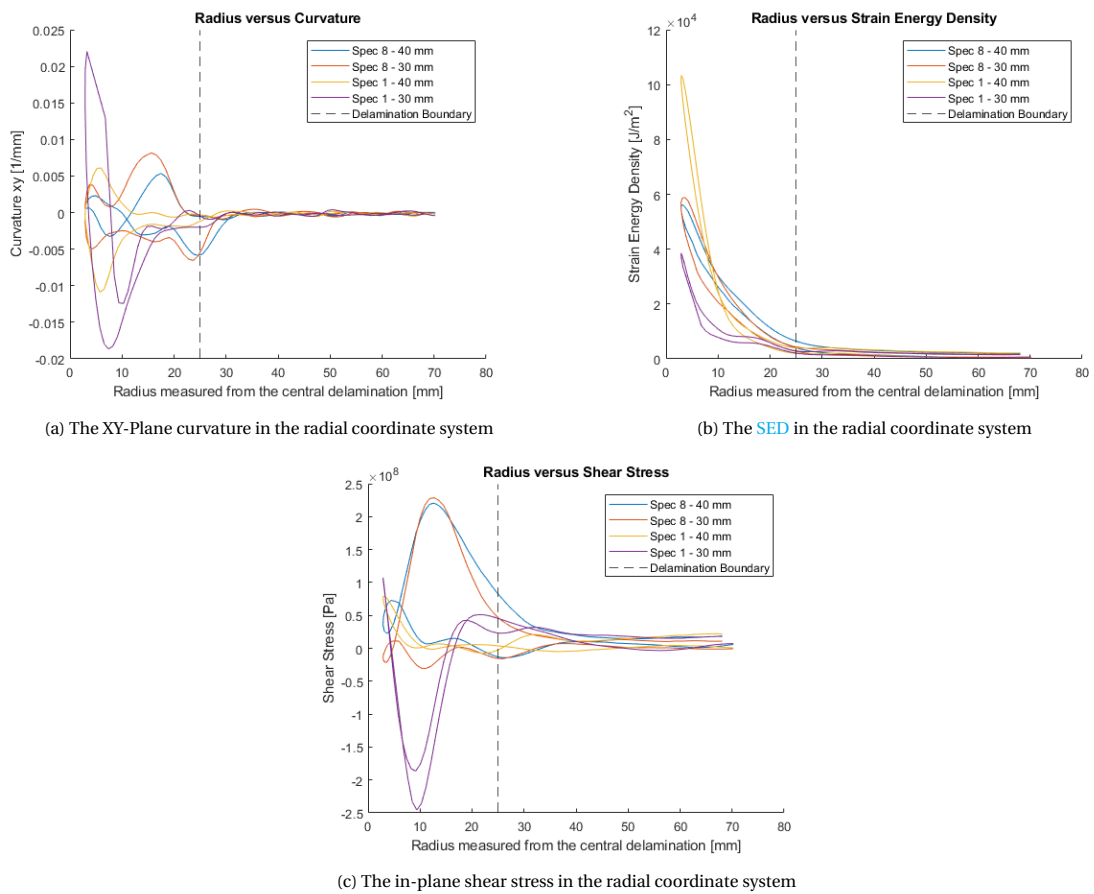
Figure 6.15: The various variable fields investigated regarding the change of indenter radius at a center displacement of 22.4 mm
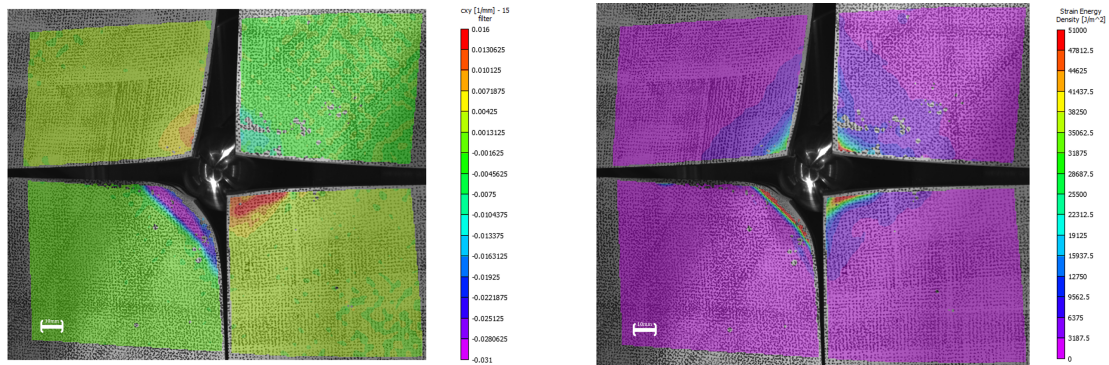
(a) The measured XY-plane curvature field

(b) The measured SED field
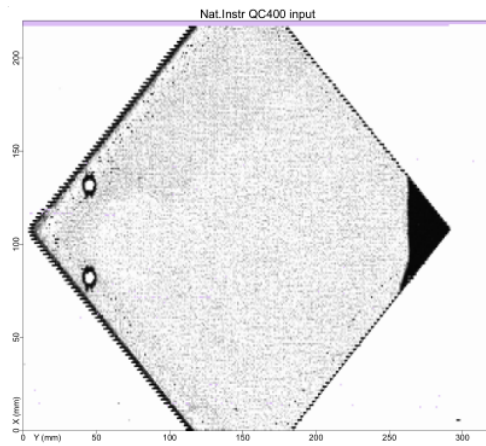
(c) The C-scan of the delamination bottom left plate

Figure 6.16: The various fields of study investigated regarding quarter plate test measured at maximum displacement

heat source and thermographic camera, to locate the delamination. This fine-tuning will require a more extensive experimental investigation than that was possible in this research.

The curvature methodology does not require an external input and delivered a clear indication for the initial delamination in the quasi-static tests.

The SED methodology currently requires the constituent properties derived through CLT. To determine the delamination size the critical SED serves as a threshold value that splits the field measurement. This delivered an area with a SED greater than the critical SED, which was the delaminated area. The image of the delamination boundary is more distorted than the curvature data predicts.

7

FATIGUE TESTS

7.1. INTRODUCTION

The quasi static tests demonstrated repeatability in chapter 6, but the delamination behavior was limited. The required out-of-plane load to expand the delamination caused fracture in the quasi-static test. Since delamination behavior occurs at lower loads in fatigue tests, this type of tests were also performed on the experimental setup. The outcomes of the fatigue tests demonstrated the progressive delamination growth behavior. To determine the physical SERR of the fatigue tests, a methodology was developed by calculating the dissipated energy into the delamination with an algorithm that was designed to track the delamination area.

7.2. EXPERIMENTAL PROCEDURE

While the quasi-static tests could not demonstrate delamination, the tests did generate insights into the repeatability of the tests and the maximum displacement that would cause fracture. Therefore, the test conditions are as following:

- The critical displacement was determined through the quasi-static tests

- The humidity in the laboratory was $65 \pm 5\%$

- The temperature in the laboratory was $20.5 \pm 0.5 C^o$

- The displacement rate of the fatigue tests was 1 mm/sec

In the test-matrix, table 7.1, all variables for the fatigue tests are provided. The critical displacement is based on the outcomes of the quasi-static SCB tests. The tests were all performed with a torque of 4 Nm, while the heat source was turned off. All the tests were performed within a day. The fatigue test with QI00 specimen, specimen 11, was the only test at which the specimen failed. The current hypothesis for this early failure is that the bending stiffness properties of the QI00 specimen is the most orthotropic, see the ratio (D11/D22) in the test matrix. This means that the load was less evenly distributed in the laminate, causing failure at the same $\delta_{max}/\delta_{crit}$ ratio. During the fatigue tests, plastic deformation occurred at the holes of the clamp frame, see figure 7.1. It was therefore recommended to increase the clamp width for future tests.

Table 7.1: Test Matrix Fatigue Tests

Specimen	Layup	Indenter diameter (mm)	Amount of Cycles	R-Ratio	$\delta_{max}/\delta_{crit}$	Type Specimen	(D11/D22)
17	QI45	30	7500	0.1	0.9	SCB	1
11	QI00	30	5	0.1	0.9	SCB	1.17
4	QI30	30	11000	0.1	0.9	SCB	1.09
18	QI45	30	10000	0.1	0.9	SCB	1

Figure 7.1: Plastic deformation caused by bearing stress in the fatigue test
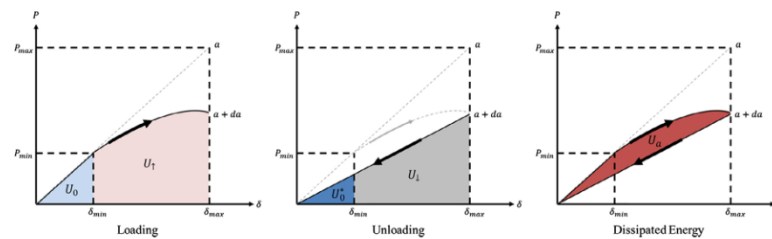
Figure 7.2: Loading and Unloading of MMB specimen [10]

7.3. CALCULATING THE CYCLIC DISSIPATED STRAIN ENERGY

During the fatigue tests, two types of load-displacement data were recorded: 1) the peak-valley data that measures the load at the maximum and minimum displacement during all the cycles and 2) the cyclic data that measures a complete loading and unloading data set once every 1000 cycles. While the cyclic data was more accurate than peak-valley data, the peak-valley data was more continuous. In this subsection a methodology was proposed that relates the change in strain energy to the loading energy and that relates the peak-valley loading energy to the cyclic loading energy. Through this methodology the change in strain energy was measured throughout the entire fatigue test.

7.3.1. RELATING CYCLIC DISSIPATED STRAIN ENERGY TO THE LOADED STRAIN ENERGY

To approach the strain energy, which is relevant for determining the strain energy release rate, a methodology should be applied that is connected to a physics-based theory. As discussed by Alderliesten [84], the dissipated cyclic work is the phenomenon that drives delamination growth in fatigue tests. As summarized by Amaral [10], the delamination was approximated with a brittle material system, where plasticity effects are negligible. Similar to what Griffith proposed [44], a single fatigue cycle under displacement controlled conditions was in written in terms of energy in figure 7.2.

$$U_0 + U_\uparrow \rightarrow U_0^* + U_\downarrow + U_a \tag{7.1}$$

Where U_0 is the monotonic strain energy which is induced in the laminate at the smallest displacement of the fatigue test. The monotonic strain energy for the performed fatigue tests is approximated with $1/2 P_{min}\delta_{min}$ to be 0.13J. This monotonic strain energy can differ between cycles which is why the monotonic energy for unloading is described as variable $\rightarrow U_0^*$. The cyclic loading and unloading strain energy are described with $U_\uparrow$ and $U_\downarrow$. The difference between the loading and unloading energy state is the dissipated energy described with variable U_a.

Every 1000 cycles during the experiment a measurement was made of the complete loading and unloading cycle in 500 steps. To calculate the cyclic loading and unloading strain energy, the load and displacement measurements of the cycles were integrated. The cyclic loading strain energy ($U_\uparrow$) of the fatigue test was then compared with the quasi-static loading energy. This relation is portrayed in figure 7.3a. This figure illustrates that the cyclic strain energy decreases over the duration of the test. Similarly, the dissipated cyclic strain energy U_a, which is determined by subtracting the return energy from the strain energy in figure 7.5a, decreases in a similar manner. Plotting these two parameters against each other, as illustrated in figure 7.4, yields a linear relationship.
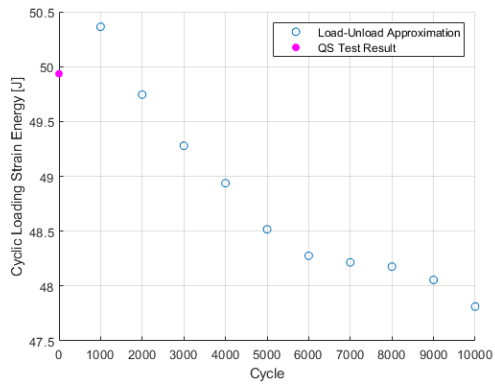
(a) The integrated cyclic strain energy with the quasi static test result
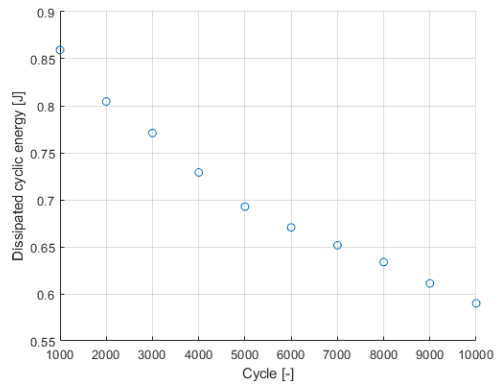
(b) Dissipated energy per cycle over the fatigue test spectrum

Figure 7.3: Outcomes of the cyclic strain energy determination
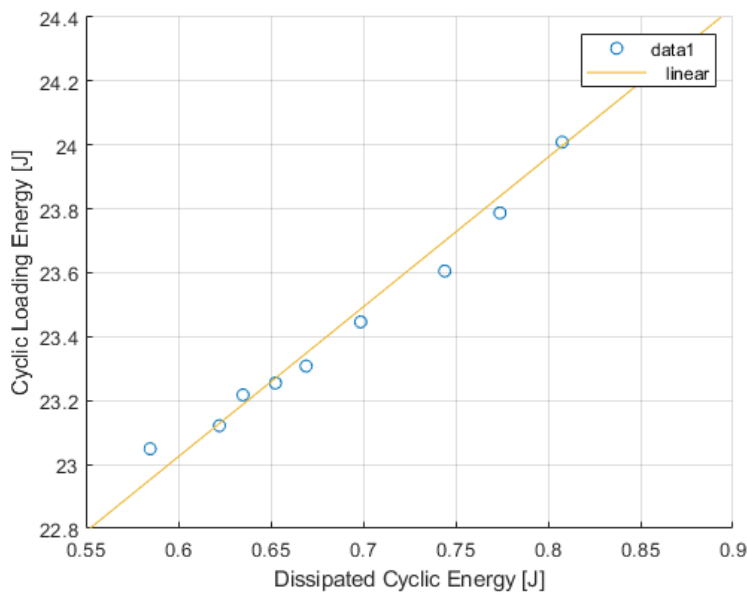
Figure 7.4: Relation between dissipated cyclic energy and loading cyclic energy

7.3.2. CALCULATING THE LOADING STRAIN ENERGY THROUGH PEAK-VALLEY DATA

The peak-valley data is the load data that was measured during the maximum and minimum displacement in a fatigue cycle. The data delivered by the peak-valley data was transformed into cyclic energy with an approximation. Both the a linear strain energy approximation (figure 7.5a) and quadratic strain energy approximation (figure 7.5b), were compared with the experimental data. The results of different approximations, figure

(a) Linear approximation [10]

(b) Quadratic approximation

(c) Comparison graph of the different approximations with the cyclic data
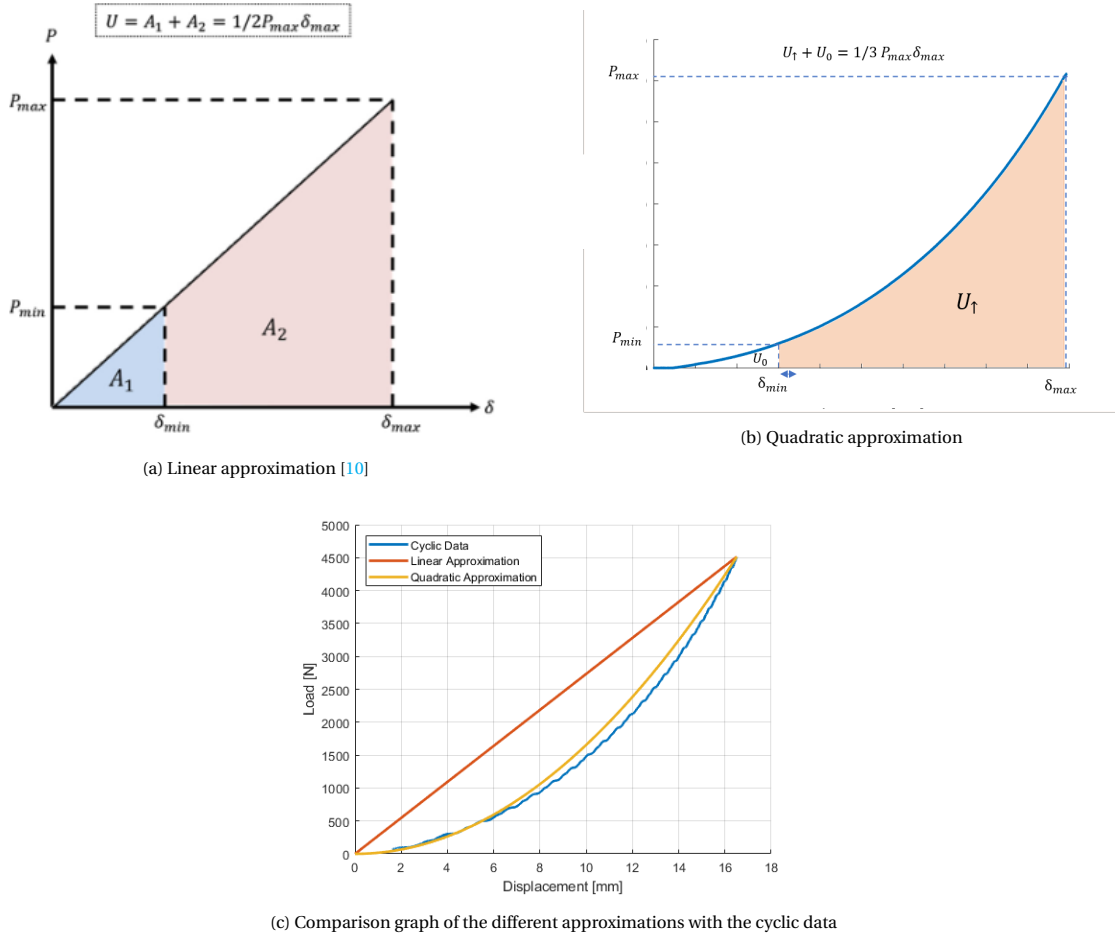
Figure 7.5: The cyclic strain energy approximations based on the peak-valley data

7.5c, was compared with the cyclic loading energy calculation of subsection 7.3.1. The quadratic approximation fitted better with the cyclic strain energy calculation and is therefore used in further analysis. The shape of both graphs is near identical, but there is a clear offset between the energy calculations. This offset was 1.79 ± 0.1 J, over the whole fatigue test of 10.000 cycles. This offset was related to the overestimation of strain energy by the quadratic approximation. By subtracting the offset of 1.79 J to the peak-valley approximation (figure 7.6) a modified peak-valley data set was created that can track the loading behavior of the laminate throughout the fatigue test.

7.3.3. DISSIPATED CYCLIC STRAIN ENERGY DETERMINED THROUGH PEAK-VALLEY DATA

In the previous subsection and figure 7.4 the relation was derived between the dissipated cyclic energy and the loading cyclic energy. Now the dissipated cyclic energy of any individual cycle was determined by combining modified peak-valley loading energy with the linear relation of the cyclic loading energy and the dissipated loading energy.

$$U_a = \frac{U_{mpv} - 20.212\text{J}}{4.687} \tag{7.2}$$

Where U_{mpv} is the modified peak-valley loading energy. The values of 20.212 J and the 4.687 resulted from the linear fit which was illustrated in figure 7.4. The offset definition of the linear function, creates insight into the
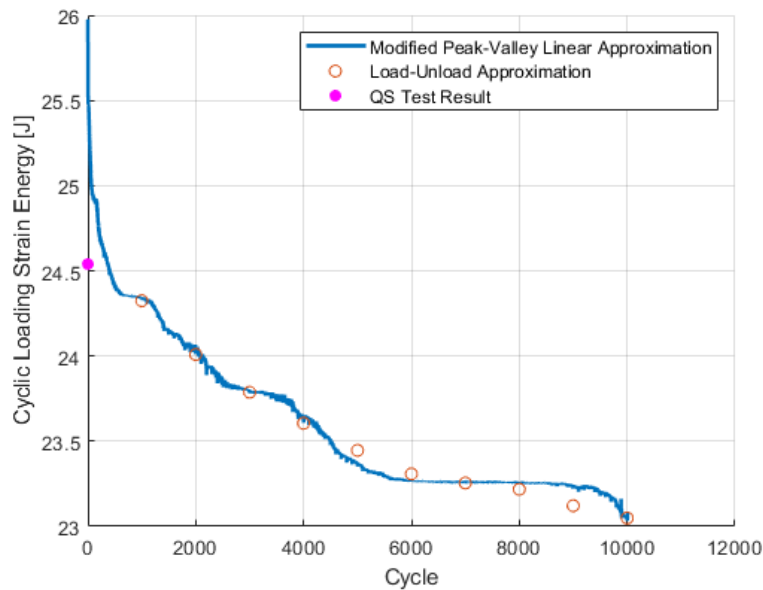
Figure 7.6: The modified peak-valley data and cyclic data to compare the cyclic loading energy

minimum required energy for opening the delamination. By adding the monotonic energy, calculated as 24 mJ with the quadratic approximation, the required minimum energy to extend the delamination was 20.35J. The resulting dissipated energy per cycle was calculated for each cycle in the fatigue test, see figure 7.7.

7.4. Determining the Delamination Area

In the quasi-static tests different methodologies for measuring the delamination area were evaluated. The most promising methodologies are the xy-plane curvature measurements and the SED-criterion field measurement. While both methodologies do seem promising, it was demonstrated that the xy-plane curvature measurement can only track the furthest extend of delamination. To track the planar delamination behavior the bond state measurement (determined through the SED criterion) was required. The best results follow when the xy-plane curvature measurement is combined with the bond state measurement since the measured SED was noisy. Both of the measurement fields are illustrated in figure 7.8. By combing both measurement techniques an algorithm was developed that can track the delamination.

7.4.1. Shape Function

The resulting planar delamination shape, plotted in figure 7.8b, had a characteristic shape. This shape is similar to the shape function applied by Koellner [11], who investigated planar delamination caused by a buckling load, illustrated in figure 7.9. To approximate the delamination area the same shape function as in Koellner's research [11] was applied. To determine the variables of the shape function, an algorithm was developed that uses both the xy-plane curvature and the SED criterion bond state map.

7.4.2. Locating delamination length and determine the critical SED through curvature data

The first step that was performed in determining the delamination area was to apply the xy-plane curvature to locate the furthest extent of the delamination. With the software that was used with the DIC measurements, *VIC-3D*, the measured coordinates were transformed into cylindrical coordinates. Initially the center of the transverse load was measured to be at the xy-coordinates (-190.38mm, 9.9473 mm). It was assumed for this analysis, that center of the delamination was at the center of the transverse load. By applying these center coordi-
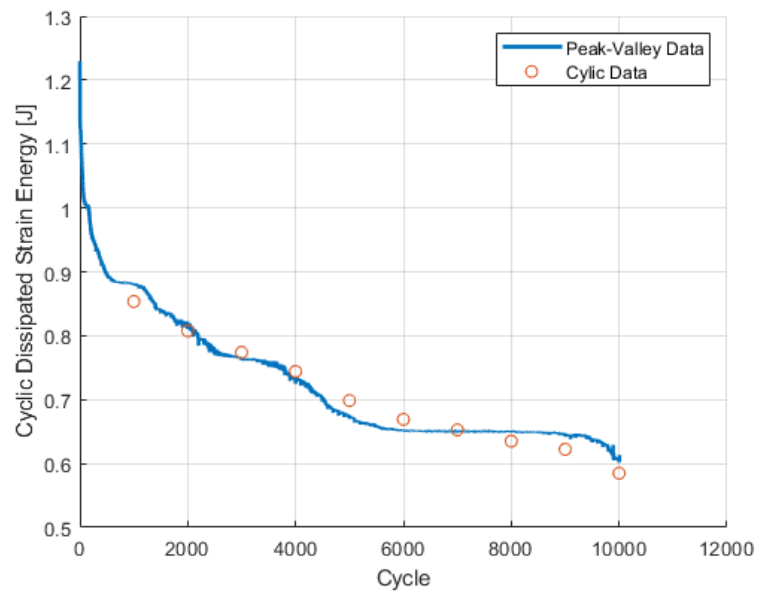
Figure 7.7: Dissipated cyclic energy calculated with Peak-Valley data

(a) The xy-plane curvature map (1/mm)

(b) The SED-criterion bond state map
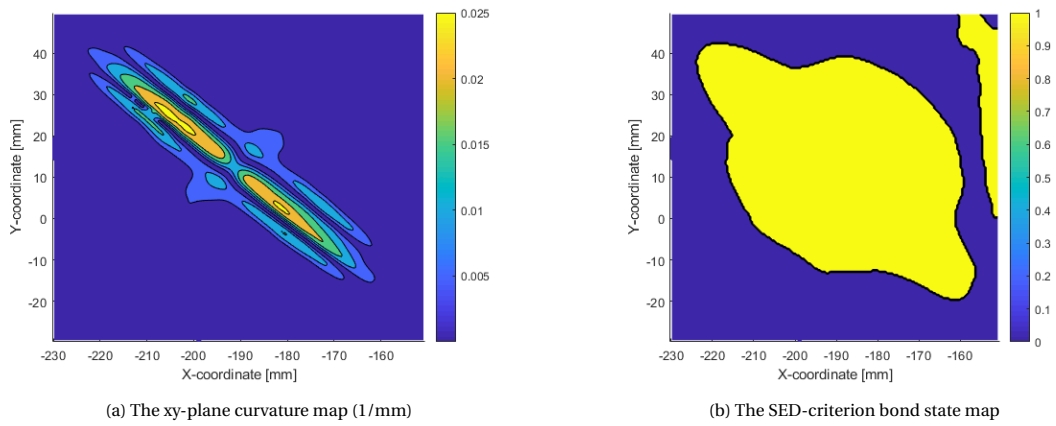
Figure 7.8: The delamination area measurements of specimen 17
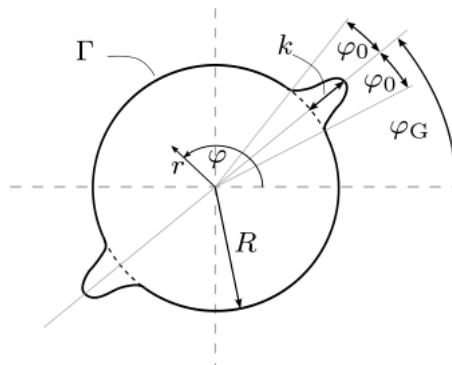
Figure 7.9: The shape function proposed by Koellner [11]

nates as X_0 and Y_0 the transformation can be performed with the functions written in equation 7.3.

$$R = \sqrt{(X - X_0)^2 + (Y - Y_0)^2} \tag{7.3a}$$

$$\phi = \arcsin\left(\frac{Y - Y_0}{R}\right) \tag{7.3b}$$

The next step was to measure the critical curvature value, which occurs at the delamination boundary. The curvature made a critical change in value at the boundary of the delamination which is seen in the contours of figure 7.8a. The curvature that was measured at the delamination boundary had a value of 0.004863 1/mm. The furthest extension of the delamination, the angle at which the delamination extends and the critical delamination in the analyzed frame were then determined as following.

$$a = k + R = \max\left(R(c_{xy} > c_{xycrit})\right) \tag{7.4a}$$

$$\phi_g = \phi(R == a) \tag{7.4b}$$

$$u_{\rho crit} = u_\rho(R == a) \tag{7.4c}$$

7.4.3. Determining the delamination width and delamination radius through the SED criterion

To determine the complete delamination shape, a bond state map is calculated by applying the critical SED criterion. A bond state map states at which point the material delaminated, with a '1', and at which points the material is still connected with a '0'. This behavior is described in equation 7.5. The resulting bond state map is illustrated in figure 7.8b. The other variables of the delamination shape function can be determined through this bond state map.

$$BS(u_\rho \geq u_{\rho c}) = 1 \tag{7.5a}$$

$$BS(u_\rho < u_{\rho c}) = 0 \tag{7.5b}$$

All the following operations have been applied to field variables of delaminated area ($BS = 1$). The next step was to determine the radius of the planar delamination growth. This was determined by the maximum delamination radius in the x-direction.

$$R_p = \max\left(R(\phi \leq \phi_g/3)\right) \tag{7.6}$$

The last part of tracking the delamination area was to calculate the width of the transverse delamination growth. This was determined by the angle at which delamination was greater than the planar delamination radius.

$$\phi_x = \min\left(\phi(R \geq R_p)\right) \tag{7.7a}$$

$$\phi_0 = \phi_g - \phi_x \tag{7.7b}$$

7.4.4. Comparison delamination area with C-scans

The bond state measurement was placed over the shape function in figure 7.10b which demonstrated that translation from bond state map to shape function operated well. The outcome of the shape function was compared with the c-scan made after the fatigue test in figure 7.10a. The measured delamination shape in the bond state graph and the c-scan matched greatly. The planar delamination is a bit cubic,see the bond-state map, and the transverse delamination growth was limited. This direct evidence proves that delamination area can be measured with the SED criterion.

7.5. Determining the Strain Energy Release Rate

The first step in determining the SERR is evaluating the delamination area measurements that have been filtered with the algorithm discussed in section 7.4. The delamination area is calculated based on the variables measured in the shape function with function 7.8.

$$A_{del} = \pi R_p^2 + \frac{1}{4} k\phi_0(8R_p + 3k) \tag{7.8}$$
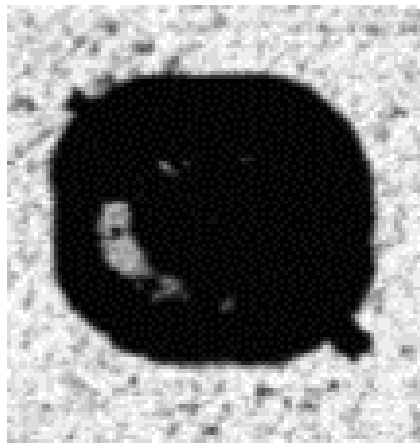
(a) Cropped c-scan made after the fatigue test
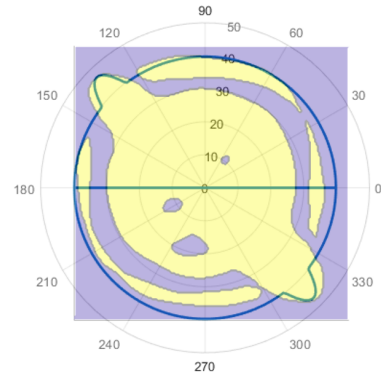
(b) The measured SED bond state graph as overlay on the shape function

Figure 7.10: The c-scan and delamination shape function fit of specimen 18

Table 7.2: Results C-scans written in delamination function variables

Specimen	k (mm)	ϕ_g (deg)	ϕ_0 (deg)	Planar Growth?
1	14	40	-	No
4	5	35	3	Yes
8	5	0	3	No
11	45	0	-	No
18	3	45	5	Yes

Figure 7.11b demonstrated that the unfiltered data made measurements that are smaller than the initial delamination radius. To make an accurate estimate, these outliers of the delamination area measurements were removed. In the beginning of the delamination process, rapid planar growth is measured up to 1400 cycles after which transverse growth follows. The planar area growth and transverse area growth are fitted with a quadratic function, figure 7.11a. The quadratic fits introduced an artifact of damped delamination growth at 1400 cycles.

For an initial insight in the SERR, the dissipated energy per cycle was plotted against the change of delamination area per cycle in figure 7.12. The plot demonstrated that the planar growth behavior was less resistant (smaller slope dU/dA) than the transverse delamination growth. This behavior is related to the greater dissipated cyclic strain energy at the start of the fatigue test. Since an overabundance of energy is available at the crack front, unstable planar delamination occurred. The physical SERR was calculated for a more thorough
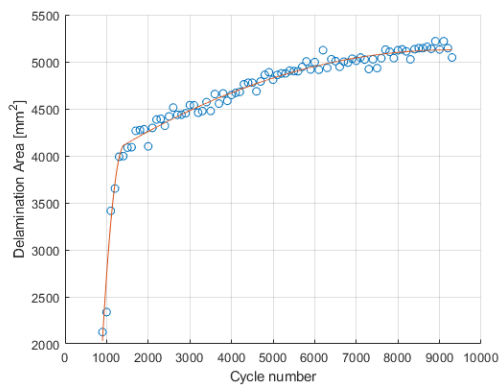
(a) The filtered delamination area measurement with 2 quadratic fits
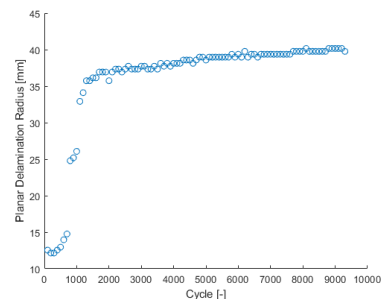
(b) Planar delamination radius development

Figure 7.11: The measured delamination area of specimen 18
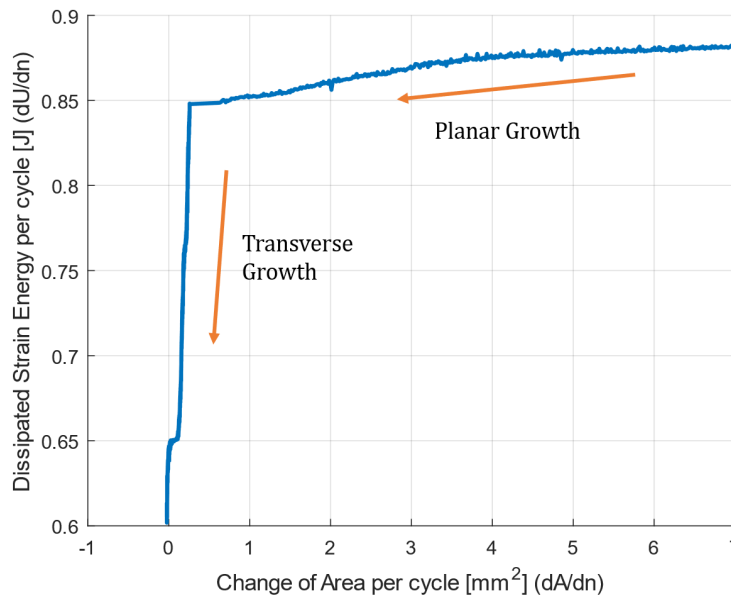
Figure 7.12: The change of strain energy versus the change of area

explanation of the resistance behavior of the laminate.

$$G_c = \frac{\partial U}{\partial A} \tag{7.9}$$

This resulted in the SERR graph in figure 7.13. The growth of the SERR turned exponential near the end of the quadratic fits. This was an artifact of the fitting method. The constant increase resistance was linked to the change of unstable planar delamination into stable transverse delamination. For comparisons between planar delamination tests, this effect should be included.

7.6. CONCLUSION

It can be concluded that the settings of the fatigue test setup are sensitive. Applying the same maximum displacement in a QI00 specimen resulted in a failed test, while the other layups were test successfully. Furthermore, the designed clamp frame offered limited stiffness which resulted in plastic deformation of the clamp and non-ideal clamped conditions for the specimen.

A methodology was developed that combines both the cyclic data and the peak-valley data of the fatigue test to determine the cyclic dissipated strain energy. This combination was possible with the linear relation between cyclic loading energy and cyclic dissipated energy. This methodology can estimate the cyclic strain energy for each individual cycle.

Based on the shape function of the delamination area, an algorithm was designed to track the delamination area throughout the fatigue test. This algorithm used the measurements of both the XY-plane curvature and the SED to estimate the planar growth behavior. The resulting delamination shape matched the c-scan.

The physical quantitative SERR that was measured during the planar delamination experiment showed that planar delamination growth was the result of the overabundance of energy at the crack front.
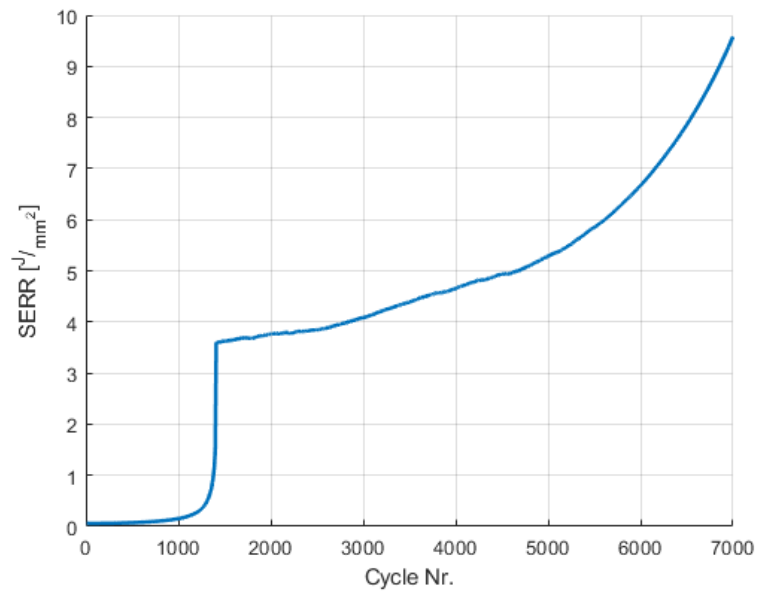
Figure 7.13: The calculated SERR of specimen 18 with an averaging filter of 10 cycles

8

COMPUTATIONAL MODEL

8.1. INTRODUCTION

The fatigue and quasi-static planar indentation experiments were performed and the outcomes differ from the initial expectations. The delamination propagation of the planar specimen was initially transverse in both the quasi-static and fatigue tests. The fatigue tests induced more delamination in the specimen before fracture and after several cycles planar like propagation occurred. Numerical model is introduced in this chapter to investigate if such planar like delamination propagation can occur in the quasi-static tests. The applicability of current mode-mixity criteria for planar delamination problems is tested through the numerical model based on VCCT.

This chapter will describe how the numerical model was developed after which a mesh convergence study was performed. The initial model behaved too stiff compared to the experiment. Different approaches were tried to identify the origin of this increased stiffness. A second model was developed with a smaller thickness, to obtain the load displacement behavior of the experiment. This model provided insights on the limitations of the current mode-mixity criteria with planar delamination problems.

8.2. SETUP NUMERICAL MODEL

The delamination characterization tests were developed to retrieve the SERRs that can be applied in numerical VCCT models[85]. This does not mean that VCCT numerical models can capture planar delamination behavior. Therefore the limitations of the mode-mixity methodology was tested for planar delamination with a VCCT numerical model . The VCCT numerical model did require an increased amount of mesh elements in the delamination direction, illustrated with ϕ_g in image 8.1. The crack direction was therefore initially derived from the experiment and the mesh was adapted.

8.2.1. SETUP PARTS

To define the delamination process of specimen, the specimen was built out of two plates that would separate. The plates were modeled as 3D extrudes. Since the problem is symmetric the plate was simplified to half a plate. The half plate length, width and thickness are 400mm, 200mm and 1.25 mm respectively. To improve
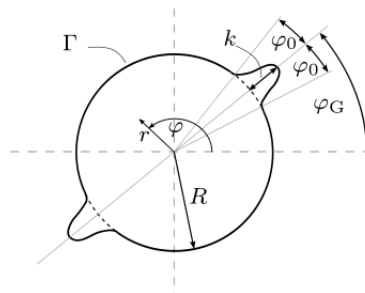
Figure 8.1: The shape function which describes the planar delamination behavior [11]

Table 8.1: Engineering Constants used for lamina properties [15]

E_x (GPa)	E_y (GPa)	E_z (GPa)	G_{xy} (GPa)	G_{xz} (GPa)	G_{yz} (GPa)	ν_{xy}	ν_{xz}	ν_{yz}
155	7.8	7.8	5.50	5.50	3.92	0.290	0.290	0.487
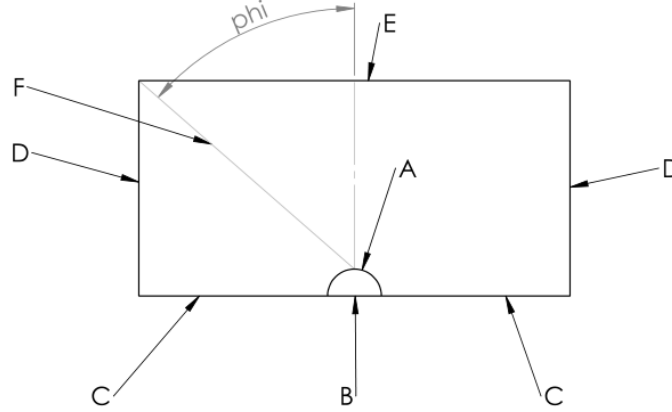
Figure 8.2: The meshing strategy of the composite plates

the mesh and to induce the initial delamination in the model, each of the plates had a partitioned surface which had a radius of 25 mm, which is defined defined by line A in figure 8.2 .

8.2.2. MATERIAL PROPERTIES
The material properties were specified through the composite module of Abaqus. First the lamina properties were initialized with engineering constants that are reported in table 8.1. Both the top and bottom plate were assigned as conventional composite shells. The composite layup of each plate was defined according to table 5.2.

8.2.3. ASSEMBLY
The bottom plate was initially added to the assembly as first instance. The bottom plate defines the coordinate system. The top plate was then added and constrained to the bottom plate with a face-to-face constraint, that directly includes a small offset. This small offset was required for the contact interactions later, this way the normal definitions of the contact can be defined by Abaqus. The bottom plate had a reference point at the point of indentation.

8.2.4. MESH STRATEGY
The mesh strategy was made to make sure that the delamination behavior can easily be simulated. This was achieved by increasing the amount of elements in the direction of the delamination growth and at the delamination boundary. To do this most efficiently the line seeds for line F and C, in figure 8.2, were biased in the direction of the initial delamination. The amount of elements that were not in the interest region were minimized. To achieve this behavior, line seeds were related to one other and extra sections for the region of interest were created. The sections and the naming conventions of the line seeds were illustrated in figure 8.2. The relations between the quantity of line seeds for the composite plate were defined according to table 8.2. The resulting meshes ,figure 8.3, demonstrated the desired node distribution for this simulation.
The type of elements that were selected for the planar delamination problem are the Abaqus SC8R, 8-node quadrilateral in-plane general-purpose continuum shell, reduced integration with hourglass control. Reduced integration with hourglass control prevents shear locking, something that would occur in models that simulate bending loads.

Table 8.2: Line Seed Relations Composite Plate related to image 8.2

Seed Line	Fraction of Seeds A
A	1
B	1/2
C	1/3
D	1/5
E	1/4
F	1
Phi	Orientation Top Layer
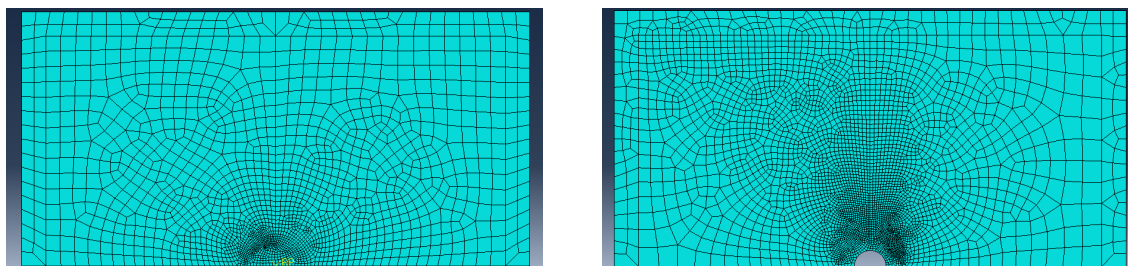
Figure 8.3: The resulting meshes of the ELS and SCB specimen of QI00

8.2.5. INTERACTION

Only a singular contact interaction was defined for this model, which is a cohesive contact between the bottom and the top plate. The surfaces allowed small-sliding contact and unstable crack growth. Unstable crack growth is efficient for computing and can be combined with linear scaling VCCT to quickly determine the displacement at which the delamination starts to grow. The bonding was limited to the bonded node set which disbonds the material at the initial delamination and at the clamped conditions, since the bond restrictions at the clamped boundary conditions caused computational problems. For the VCCT contact the classical BK-Law was applied with the properties of table 8.3. The VCCT crack layer had an out-of-plane surface thickness of 2e-5 mm. The contact interactions were defined in the first step after initialization.

8.2.6. BOUNDARY CONDITIONS

The boundary conditions at the sides of the laminate, with the exception of the side that is along the x-axis , were set to ENCASTRE to simulate the clamped conditions. At the center of the laminate, at the x-axis in figure 8.4, YSYMM conditions were applied. A reference point was placed on the plates, which would displace to induce the load in laminate. The reference point was placed on the bottom surface for the ELS specimens, while a reference point has been placed on the top surface for SCB specimens. The reference point defined the master-slave definitions of the model. For the ELS specimen, the bottom plate was the master surface (with the reference point) and the top plate was the slave surface whereas for the SCB specimen the top plate was the master surface (with the reference point) and the bottom plate was the slave surface.

8.2.7. STEP SIZE

The settings in the step determined performance of the model. The model behavior was set to be non-linear. The maximum increment size was 0.01 while the minimum increment step size was 1e-12. The initial increment was 0.001. The maximum amount of increments was set at 5000. The solver was a direct Full-Newton method which ramps linearly.

Table 8.3: The B-K law interaction properties used in the VCCT analysis [15]

$G_I(J/m^2)$	$G_I(J/m^2)$	$G_I(J/m^2)$	n	tolerance
241	971	971	1	0.2
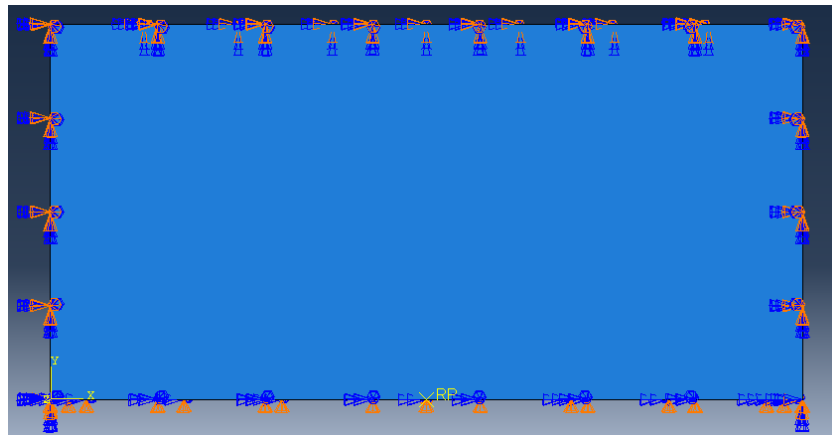
Figure 8.4: The applied boundary conditions for the assembly

Table 8.4: Mesh Convergence Properties

Amount of seeds A	Total amount of elements	Load at 25 mm (kN)	Computation Time (min)
20	1846	36.5	6
30	3828	36	15
40	9507	No Iteration at 0.0007	17

8.2.8. REQUIRED FIELD AND HISTORY OUTPUTS
The following Field Outputs were selected for the analysis of the experiment:

- BDSTAT: Bond State of the material

- E: Total Strain Components

- ENRRT: SERR

- RT: Reaction Forces

- S: Stress Components of invariants

- U: Translation and Rotations x-direction

- ELEDEN: All Energy Density Components

- SE: Section Strains and Curvatures

The following History Outputs were selected for the analysis of the experiment:

- ENRRT1: Mode I SERR

- ENRRT2: Mode II SERR

- ENRRT3: Mode III SERR

Only the ELEDEN, the U and the RT components have been used for the analysis.

8.2.9. MESH CONVERGENCE
The mesh convergences have been performed and the results are presented in table 8.4. The load at the final displacement is varying about 1.5%, while at the same time the model with the greatest number of elements could not iterate. Therefore, the model with 30 seeds has been selected to perform the delamination analysis.

8.3. Comparison with the experimental results

The initial mesh converged and the 6 different delamination models (2 type of specimen and 3 layups) were successfully completed. Three different sets of data were compared between the numerical model and the experiment. The load-displacement response was compared since this data was most accurately measured in the test setup. Then development of delamination area was investigated, which demonstrated to what extend the BK mode-mixity criterion is applicable in a planar test. The last point of investigation was the SED map produced by the numerical model.

8.3.1. Load-Displacement Data

The load displacement data is the direct response of the material and was investigated first. To determine the load displacement data of the numerical model was derived from the reaction force and displacement of the indentation node. Figure 8.5 showed that the laminate has a greater bending stiffness than the measured experimental laminates. To investigate how this difference in behavior came to be, 3 different investigations were performed.

- The number of elements near the indentation tip was greatly increased to reduce the overestimation of the indentation load. The difference between 8 and 40 seeds near the indentation tip resulted in a reduced stiffness of about 4%.

- The manner of load induction was caused by moving a central point with an indicated central displacement. This causes distortions around the central node. Instead of inducing the load with a single central node, a whole set of nodes around the area of the indenter radius was displaced instead. The combined load of this set of nodes is equal to the single node behavior, meaning that this did not cause the reduced stiffness problem.

- The issue was the application of the boundary conditions in the numerical model were stricter than the actual clamping conditions that occur in the experiment. Figure 8.6 illustrates how the clamping frame bend slightly with the specimen. It was mentioned in chapter 6 that clamping frame was not designed for the maximum load measured in the test setup. This means that the clamping frame cannot give the stiffness to maintain the clamped boundary conditions. To achieve the same displacement in the model, more force was required due to the strict boundary conditions which is why a stiffer response results from the model.

8.3.2. Delamination Area

The increased delamination area was measured by the change of the average bond state in the cohesive material. This measurement is more of a qualitative indication than a quantitative indication, since the bonds are not evenly spread over the contact interface. The change of average bond state during the simulation was then multiplied by the area of the bond state, illustrated in figure 8.7.

The delamination area is increasing way more rapidly than the quasi-static measurements. This is can be caused by the SERR mode-mixity criterion. Another reason could be that the only damage behavior that was accounted for in this model is the delamination behavior. This means that damage caused by matrix cracking, which would reduce the stiffness of the laminate and generally retards the delamination growth behavior, has not been included. The most likely cause for this overestimation of delamination is the increased stiffness of the composite plate. This means that more energy is introduced in the composite laminate and the delamination boundary, which results in more delamination.

8.3.3. SED field

The SED field that results from the numerical model is illustrated in figure 8.8. The difference in distribution of SED was the first aspect that is noticeable in the outcomes. The SED measured in the experiment (figure 6.5) demonstrates a distorted version of diamond contours which were generated by the numerical model. The quantity of the SED of this numerical model was 3 times greater than the measured SED in the experiment.

The SED development that occurs when the delamination expands does demonstrate the applicability to measure the delamination in the material with the SED. Further insight should be generated with a numerical model that applies a SED criterion.

(a) QI00

(b) QI30

(c) QI45
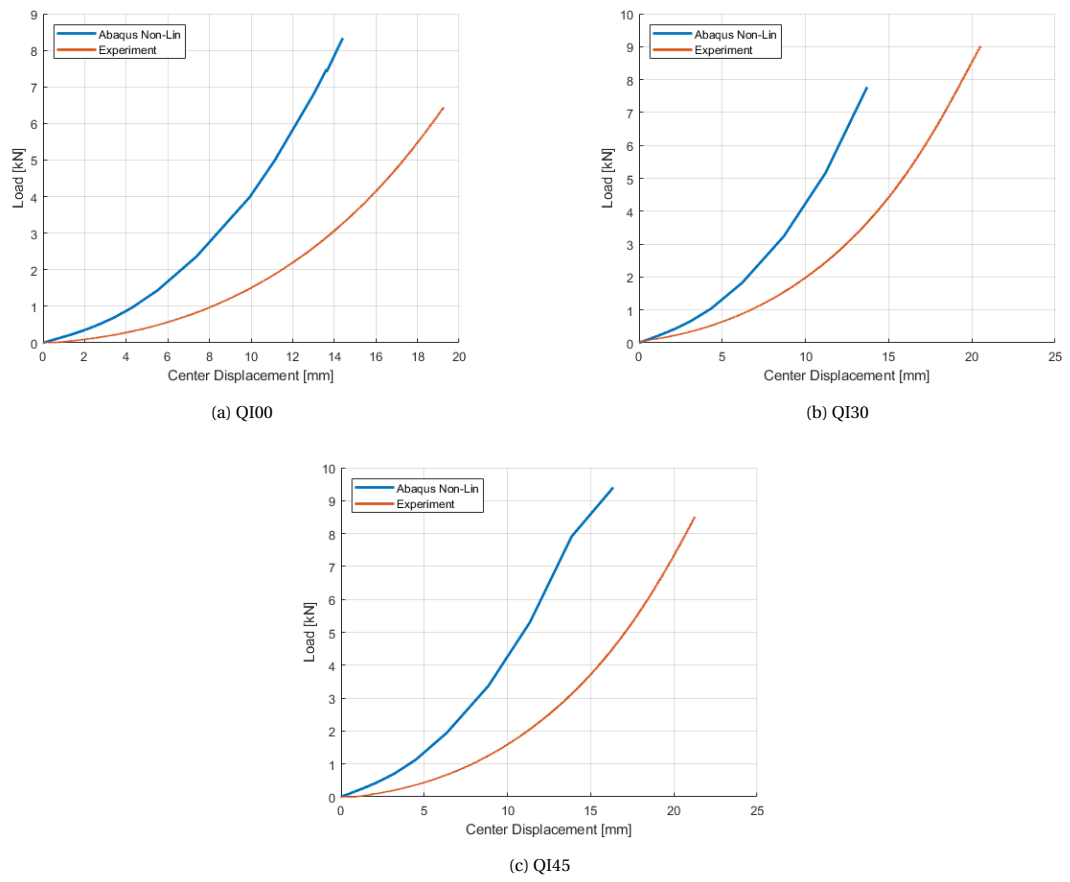
Figure 8.5: The various load displacement comparison graphs of the SCB specimen

Figure 8.6: At the peak load the clamping frame starts to elastically bend with the specimen

8.4. THICKNESS CORRECTION MODEL

To compensate for the strict boundary conditions, which did not match with the experiment, an iteration on the model was developed. This model accounted for the strict boundary conditions by reducing the thickness of the plate. The thickness reduction reduced the stiffness of the model, which means the model acted more like the experiment. Figure 8.9a shows how the stiffness drops with the reduction of the thickness of the composite plate. Initially the 2mm thick plate acted like the experiment, however at a certain displacement the stiffness diverges. Figure 8.9b shows that this overestimation happens at the incrementation step at 8 to 10 mm displacement. In figure 8.10a it is shown that from 10 mm onwards the delamination expansion continues in a planar manner. The final crack front of the simulation is portrayed in figure 8.10b, which shows that the model is not including a direct transverse delamination shape. The irregularities of the curved crack front were caused by the mesh, and should be expected in an experiment. The delamination radius at 20 mm displacement, which is the greatest displacement in the quasi-static QI00 experiment, is 38 mm. The SED field of the delaminated specimen, figure 8.11, was given a custom legend to show the SED distribution beyond the delamination. The maximum SED in the legend is set the same as critical SED measured in specimen 12. The measured 3000 J/m^2 was divided by its thickness of 2.5 mm, which delivered an experimental critical SED of 1.2 MJ/m^3. The SED pattern retrieves the same delamination radius of 38mm, which is the size of the delamination in the model. This demonstrated the that the SED criterion bond state matches actual bond state of the numerical model.

8.5. CONCLUSION

To investigate the applicability of the mode-mixity criterion, a numerical model applying this criterion was developed. Initially the load-displacement behavior was compared with the experimental data. To compensate for the difference between the strict clamping conditions of the model, versus the less strict clamping behavior of the experiment the model was remade with a smaller thickness.The load-displacement behavior of the reduced thickness model was similar to the experiment until planar delamination occurs. The matching load displacement behavior was a requirement for an accurate model. The next model should change the boundary conditions of the model to match the experiment.

The delamination behavior seems more realistic with the reduced thickness model than the actual thickness model. The SED of the reduced thickness model allowed to make delamination predictions when matched with the experimental SED. The delamination area growth was overestimated greatly with the actual thickness model and slightly overestimated with the reduced thickness model. This could be caused by the mode-mixity criterion or the lack of other damage mechanisms in the model.

(a) QI00

(b) QI30

(c) QI45
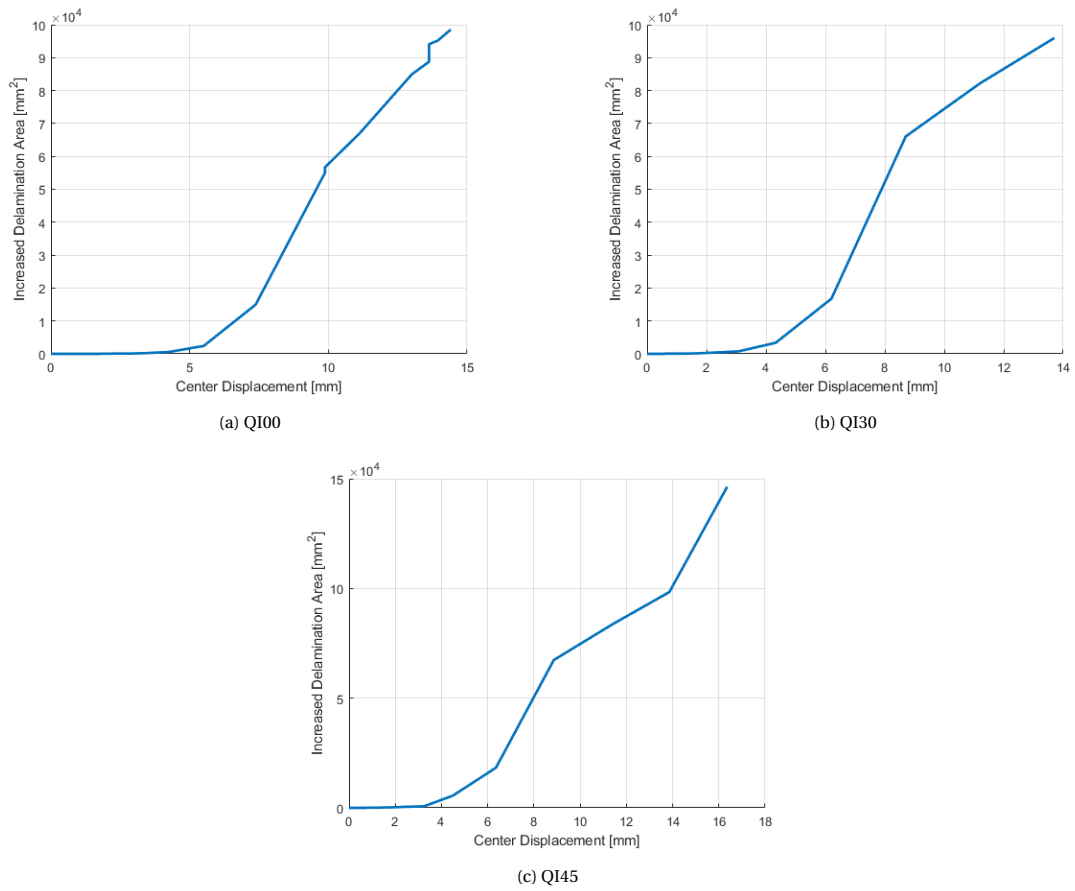
Figure 8.7: The various delamination area graphs of the SCB specimen

(a) QI00

(b) QI30

(c) QI45
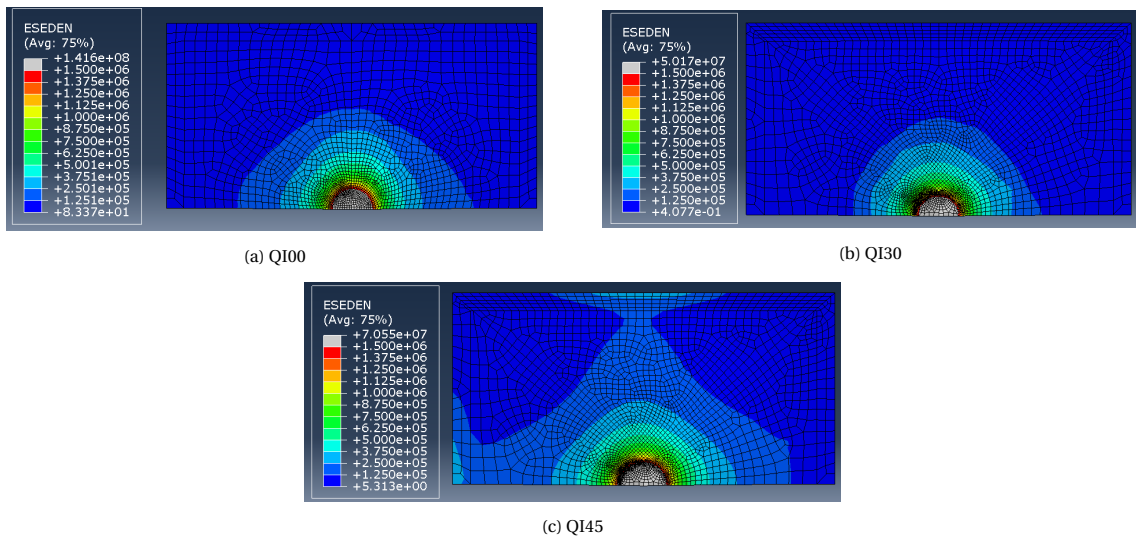
Figure 8.8: The various SED graphs of the SCB specimen at their maximal displacement
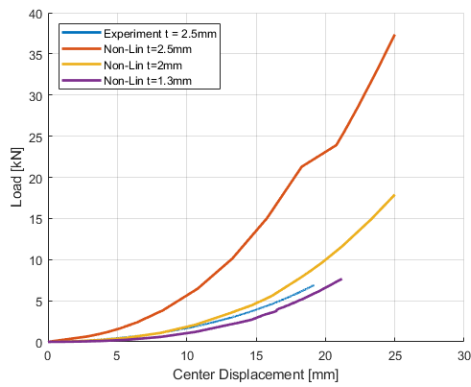
(a) The comparison between different thickness iterations with the experiment
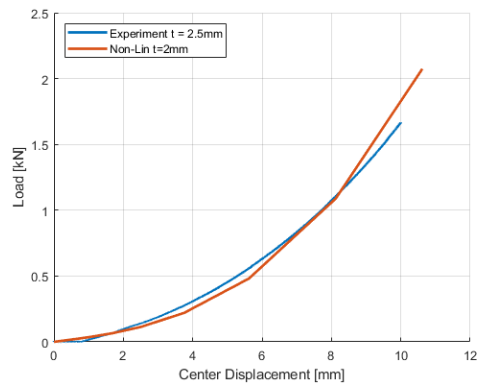
(b) Sudden overestimation of stiffness at 8mm displacement

Figure 8.9: The resulting load displacement graph when correcting model's behavior through thickness of ELS QI00
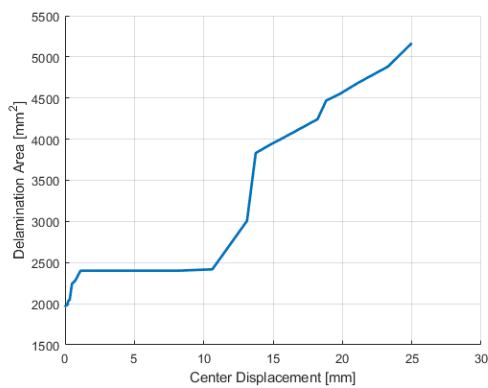
(a) The delamination growth during the quasi-static loading
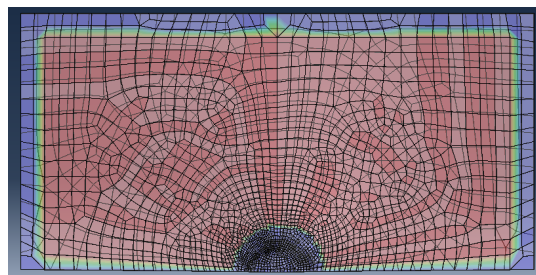
(b) The delamination shape at 20mm displacement

Figure 8.10: The delamination behavior of the ELS QI00 model with 2mm thickness
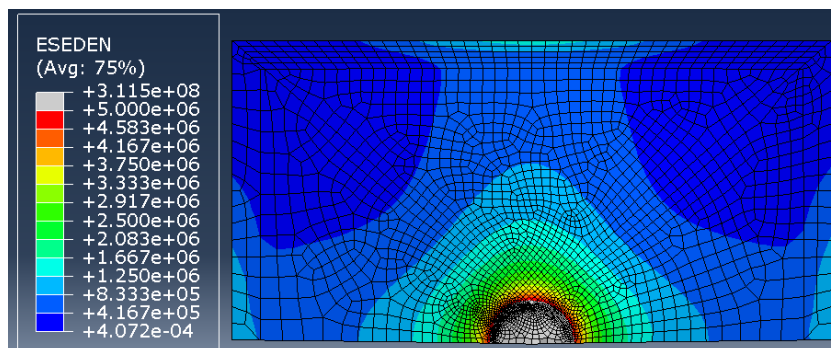
Figure 8.11: The SED field of the ELS QI00 model with 2 mm thickness at 25mm displacement

9

DISCUSSION

9.1. INTRODUCTION

Through the different studies performed in this investigation, it was demonstrated that SED that is a suitable tool for estimating planar delamination. To gain insight in why the standard SERR was not suitable for planar delamination, the discussion investigated the origins of the SERR methodology. The original papers demonstrated that the use of the standard SERR is limited to closed energy systems, which made it not suitable for the fatigue the planar delamination tests. To compare the planar delamination tests, the physical SERR is therefore applied.

Following on this discussion of the SERR, a comparison was made between the physical SERR of the analytical model with the physical SERR measured in the transverse opening load experiment [6]. The differences between the physical SERRs gave insight into the relation between constituent properties and delamination resistance.

The outcomes of the fatigue delamination experiment demonstrated similarities with the impact study on a planar specimen by Davies[12]. The relation between the indentation test and Davies' planar delamination test was investigated to relate the physical SERR to different types of delamination behavior in planar tests.

With a measurement technique that can measure the SED in an experiment, the methodology to calculate the critical SED by Daneshjoo and Amaral [3, 15, 23] with a coupon test was be tested. The assumption was that the SED is a material constant, so this value should be the same in a planar test and a coupon test.

9.2. THE APPLICATION OF THE PHYSICAL SERR

During the analysis of the fatigue outcomes, the physical SERR determined the amount of work required to expand the delamination. The reason why physical SERR was used in the analysis instead of the standard definition of SERR [1], is because the standard SERR cannot be easily measured in planar delamination tests. The development of the ASTM standard for determining the delamination resistance, and the application of the standard SERR, started with the explorative work of Kanninen et al. [86]. During this explorative work various fracture mechanics applications (e.g. SERR, SED,SIF and max stress criterion) were investigated to determine which application can characterize the delamination failure behavior in fiber reinforced composites. The proposal that followed from this investigation was: "Any element of a fibre composite ruptures when an intrinsic critical energy dissipation rate can be provided." Kaninnen et al.'s interpretation of the SERR is as driving force to propagate delamination. This interpretation of the standard SERR, results from Griffith's interpretation of the SERR, when measuring the standard SERR in a test that expands delamination slowly. The assumption that Griffith made to define the SERR as driving force, was that no extra load is induced during the delamination meaning that the experiment behaved as a closed energy system. In a closed energy system, the restriction to delamination growth, standard SERR, can be set equally to the driving energy based on the law of conservation of energy. In an open energy system, like a fatigue test, an overabundance of energy in the system will cause unstable delamination. In unstable delamination the standard SERR is not equal to the driving force in the system. The physical SERR can describe how the delamination growth propagates in unstable delamination, since it is pure relationship between the change of induced work and the change of

Table 9.1: The average Strain Energy Release Rate of Cameselle-Molares tests

Mat	$\overline{G_{cA}}(J/m^2)$	StD (J/m^2)
50/50-1	2178.7	5.908
50/50-2	1982.6	5.44
60/40-1	2608.2	5.331
60/40-2	2775.5	5.765
70/30-1	3098.2	3.597
70/30-2	3028.1	3.738

delamination area

$$\frac{\partial}{\partial A}(W - U) = 0 \tag{9.1}$$

When investigating the fatigue delamination resistance of the experiment, the physical SERR demonstrated how the resistance changes with the delamination growth behavior. This behavior provided new insights on how delamination propagation was influenced by an overabundance of energy. To gain similar insights in other planar delamination experiments, it is recommended to apply the physical SERR.

9.3. PHYSICAL SERR OUT-OF-PLANE OPENING LOAD PLANAR DELAMINA-TION EXPERIMENT

In correspondence with the author of the of the out-of-plane opening load planar delamination experiment [6], a data set was received which consisted of the load-displacement, compliance and the delamination area data measured during their experiment. The SERR was calculated from this data set.

9.3.1. CALCULATING THE SERR

The definition of the SERR that was used for analyzing the planar delamination data of the planar load opening experiment is the physical SERR. With the retrieved data, the physical SERR was calculated as following:

$$G = \frac{\partial U}{\partial A} = \frac{\partial(\frac{1}{2}ku^2)}{\partial A} = \frac{\partial(\frac{1}{2}CP^2)}{\partial A} \tag{9.2}$$

Where equation k is the transverse stiffness of the composite, u is the transverse displacement, C is the transverse compliance of the composite and P is the transverse load. The calculation was similar to the compliance calibration method [1], the only difference was that in the planar experiment the load does not remain constant when delamination growth occurs.

$$G = \frac{1}{2}\frac{P^2\partial C}{\partial A} + \frac{1}{2}\frac{C\partial P^2}{\partial A} \tag{9.3}$$

This can be simplified with the product rule which results into the following.

$$G = \frac{1}{2}\frac{P^2\partial C}{\partial A} + \frac{PC\partial P}{\partial A} \tag{9.4}$$

The calculated SERR is scattered, as illustrated in figure 9.1. To retrieve a comparable SERR the data was fitted with third order polynomial. The resulting polynomial was then plotted in the scattered and the resulting mean SERR and standard deviation were reported in table 9.1.

9.3.2. COMPARISON WITH THE PERFORMED PLANAR EXPERIMENT

Like the outcome of the fatigue experiment, the SERR is not converging to a singular value which would be common in a coupon test. The reason why this behavior was occurring is due to the constantly changing crack front. When the crack front changed, either in size or shape, the SERR will increase preventing the physical SERR from converging. This was also why it is difficult to relate the coupon SERR to the physical SERR of the test.
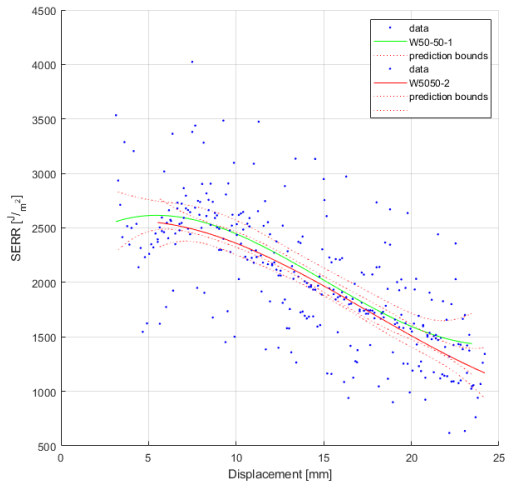
(a) Experimental Strain Energy Release Rate 50-50 Mats [6]
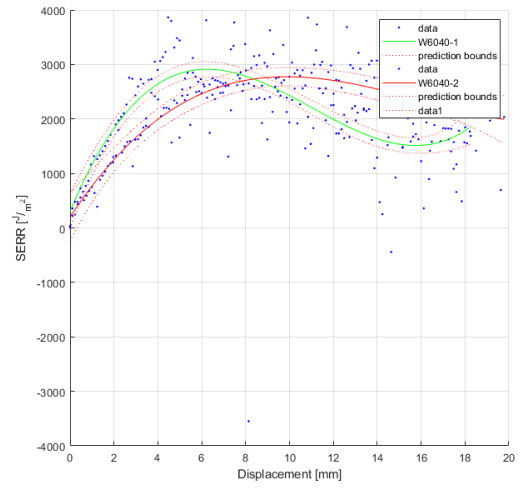
(b) Experimental Strain Energy Release Rate 60-40 Mats [6]
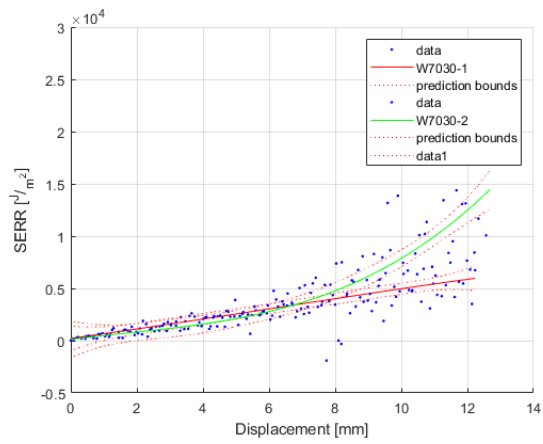
(c) Experimental Strain Energy Release Rate 70-30 Mats [6]

Figure 9.1: Planar delamination Strain Energy Release Rates with 3rd order polynomial fit

9.3.3. COMPARSION WITH THE ANALYTICAL MODEL

The SERR that results from transverse out-of-plane load opening experiment is showing similarities with the analytical model which is developed in chapter 3. The The 50-50 mat is an exception to the similarity between the two outcomes, since the SERR is only dropping in the experiment whereas the model predicted it to grow. A great fit can best be seen with the 60-40 mat, where the SERR is first slightly increasing after which it starts to drop at planar delamination growth. In the 70-30 mat experimental SERR graph, figure 9.1c , it is hard to notice how the similar behavior is occurring in the first phase of transverse growth, due to the growth of the SERR of the mat 70-30-2 near the end of the test. The magnitude of the different physical SERR's increases with the increased orthotropy of the material. This effect was predicted with SED criterion. The magnitude of these differences does differ greatly between the model and experiment, but also between two tests of the same material.

9.4. COMPARISON PLANAR DELAMINATION BY INDENTATION AND IMPACT

The research on the relationship between delamination induced through impact and indentation has been around for quite a while [24]. To further elaborate on this relationship, the outcomes of the planar delamination experiment were compared with the impact results by Davies [12]. In the study Davies investigated the relation between the impact damage area and the peak load, while also investigating the relation between the damage area and the indentation energy. The measurements were made with a drop tower, whereby an impactor, with strain gauges attached to measure the load and a grid at the side to measure the velocity, was dropped on composite specimen. The composite specimens were made as small coupons (100mm x 75 mm) and large coupons (200mm x 200mm). While the specimen width dimensions differ, the applied layup for the 2mm thick plate in Davies' study is identical to the QI00 layup tested in the current study. The results of Davies's experiment is illustrated in 9.2. The figure shows that the resulting delamination shapes match those of the fatigue results before the delamination grows more in a planar fashion. Davies did not describe the delamination size neither can this be derived from figure 9.2a. Davies described the delamination damage area in the graph that relates the impact energy with the damage area. To compare the results of Davies's experiment with the results of this experiment, the area with the cumulative dissipated strain energy is illustrated in figure 9.3. The data from this research demonstrate a direct linear relationship between the damage area and the indentation energy. Whereas in Davies' experiment, figure 9.2b shows that the relation between the impact energy and damage area grew in exponential manner at the initial delamination onset after which the growth stabilizes in a linear manner. This is the same effect, caused by the overabundance of energy at the delamination front. The initial exponential growth of Davies's experiment was linked to the initial planar delamination growth of the impact load.

The induced energy versus delamination area graphs of the quasi-static tests performed by Cameselle-Molares [6] differed from the fatigue and impact graphs. Figure 9.4 showed that for both the 50-50 mats and the 60-40 mats a linear relation directly appeared. This direct linear relationship was caused by the quasi-static test conditions, unstable planar delamination growth was therefore avoided. The exception is the 70-30 mats which display a non-linear relationship. This non-linear relationship can be linked to the fact that test was stopped earlier than the 50-50 and 60-40 mats. Only 30 joules was induced in the 70-30 mats, whereas the 60-40 and 50-50 mats were loaded up to 100 joules.

9.5. DERIVATION CRITICAL SED WITH COUPON TEST DATA

Daneshjoo [15, 23] and Amaral [3] tested coupons in a MMB test to study differences of the onset SERR in fatigue test. During their tests a method was developed to determine the critical SED with a physics-based relationship. The studies of Amaral and Daneshjoo state the critical SED should be independent of the loading condition. Therefore it is assumed to be a material constant. To investigate if the critical SED is independent of the topology of the problem, the critical SED was calculated based on Daneshjoo's coupon data of the material [23] and compared with the measured critical SED of the performed fatigue test.

The determination of the critical SED with coupon applied the following definition of SED.

$$\frac{dW}{dV} = \frac{1}{2}\left[\frac{\sigma_x^2}{E_x} + \frac{\sigma_y^2}{E_y} + \frac{\sigma_z^2}{E_z} + \frac{\tau_{xy}^2}{G_{xy}}\right] - \frac{\nu_{xy}\sigma_x\sigma_y}{E_x} - \frac{\nu_{xz}\sigma_x\sigma_z}{E_x} - \frac{\nu_{yz}\sigma_z\sigma_y}{E_y} \tag{9.5}$$
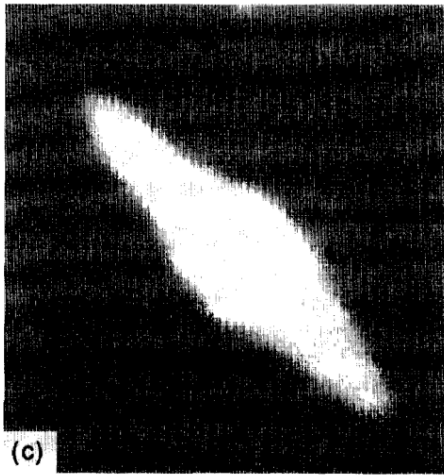
(a) C-scan of the 200mm x 200mm x 2mm clamped plate, indentation energy 9.34 J
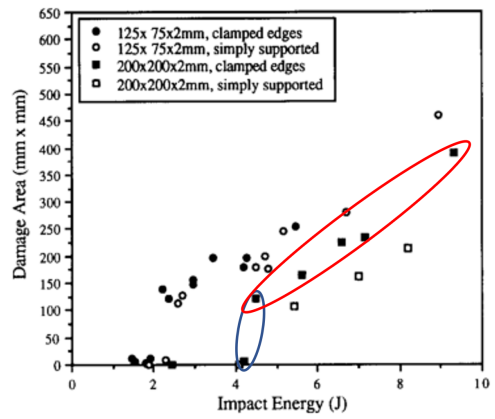
(b) The delamination area versus impact energy, red circles were added for explanatory reasons

Figure 9.2: Outcomes of Impact Study [12] of plate CFRP plate with layup $[0, 90, -45, 45]_{2s}$, indenter diameter 12.7 mm
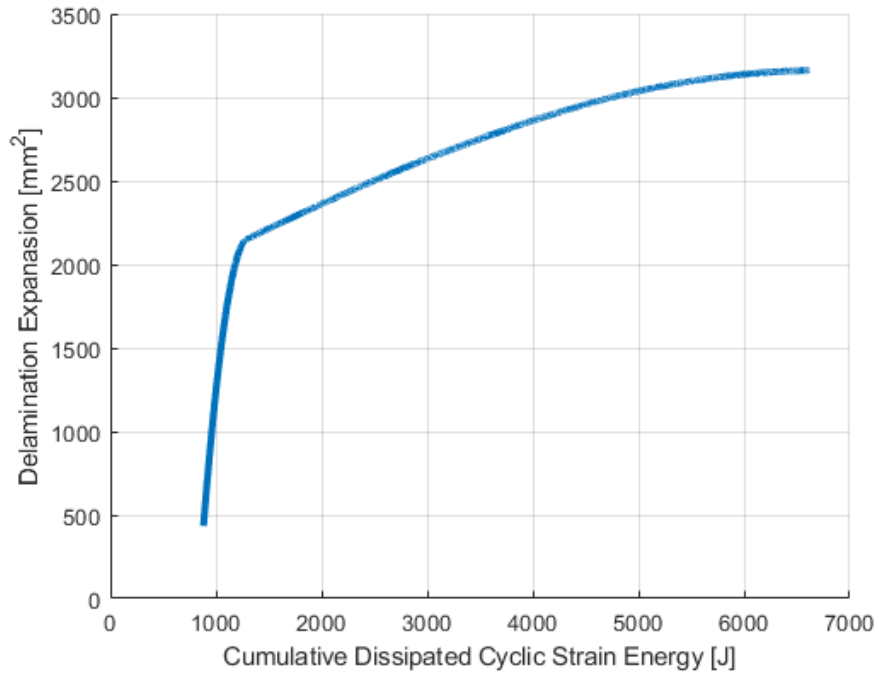
Figure 9.3: Total dissipated energy versus delamination area of Specimen 18
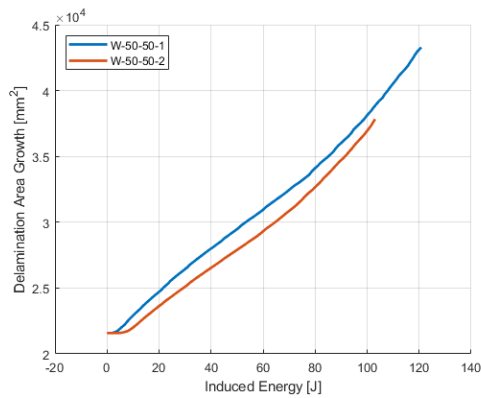
(a) 50-50 Specimen
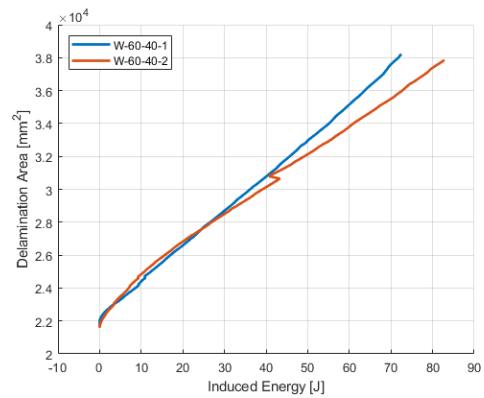
(b) 60-40 specimen
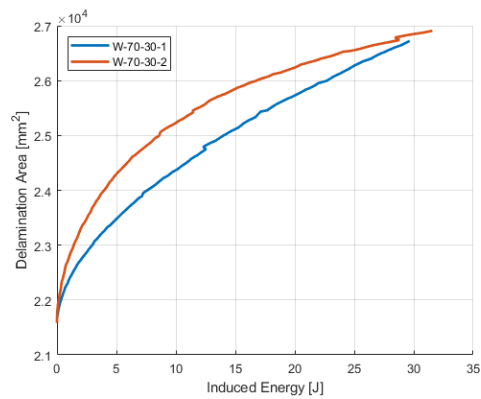
(c) 70-30 specimen

Figure 9.4: The induced energy versus delamination area graphs based of the planar delamination opening tests [6]

This definition of the SED can be rewritten with the stresses defined in terms of SIF.

$$\sigma_x = \frac{1}{\sqrt{2\pi r}} \left(K_I A_I(\theta) + K_{II} A_{II}(\theta) \right) \tag{9.6a}$$

$$\sigma_y = \frac{1}{\sqrt{2\pi r}} \left(K_I B_I(\theta) + K_{II} B_{II}(\theta) \right) \tag{9.6b}$$

$$\tau_{xy} = \frac{1}{\sqrt{2\pi r}} \left(K_I C_I(\theta) + K_{II} C_{II}(\theta) \right) \tag{9.6c}$$

$$\sigma_z = \frac{1}{\sqrt{2\pi r}} \left(K_I A_I(\theta) + K_{II} A_{II}(\theta) \right) \frac{\nu_{xz} E_z}{E_x} + \frac{1}{\sqrt{2\pi r}} \left(K_I B_I(\theta) + K_{II} B_{II}(\theta) \right) \frac{\nu_{yz} E_z}{E_y} \tag{9.6d}$$

Where the angular functions are as following.

$$A_I(\theta) = Re \left[\frac{x_1 x_2 (x_2 F_2 - x_1 F_1)}{x_1 - x_2} \right] \qquad\qquad A_{II}(\theta) = Re \left[\frac{x_2^2 F_2 - x_1^2 F_1}{x_1 - x_2} \right] \tag{9.7a}$$

$$B_1(\theta) = Re \left[\frac{x_1 F_2 - x_2 F_1}{x_1 - x_2} \right] \qquad\qquad B_{II}(\theta) = Re \left[\frac{F_2 - F_1}{x_1 - x_2} \right] \tag{9.7b}$$

$$C_I(\theta) = Re \left[\frac{x_1 x_2 (F_1 - F_2)}{x_1 - x_2} \right] \qquad\qquad C_{II}(\theta) = Re \left[\frac{x_1 F_1 - x_2 F_2}{x_1 - x_2} \right] \tag{9.7c}$$

Which allows the original SED function 9.5 to be rewritten into a simpler form.

$$\frac{dW}{dV} = \frac{1}{\pi r} \left[\frac{1}{\pi r} K_I^2 D_1 + K_{II}^2 D_2 + 2 K_I K_{II} D_3 \right] \tag{9.8}$$

Where r is the distance from the crack in the material and the SIF variables are described with K_i. The D_i are the transformation parameters which depend on the compliance behavior of the orthotropic material.

$$D_1 = \frac{1}{4} \left[\frac{A_I^2}{E_x} + \frac{B_I^2}{E_y} + \frac{C_I^2}{G_{xy}} - \frac{2 A_I B_I \nu_{xy}}{E_x} - \frac{A_I^2 \nu_{xz}^2 E_z}{E_x^2} - \frac{B_I^2 \nu_{yz}^2 E_z}{E_y^2} - \frac{2 A_I B_I \nu_{xz} \nu_{yz} E_z}{E_x E_y} \right] \tag{9.9a}$$

$$D_2 = \frac{1}{4} \left[\frac{A_{II}^2}{E_x} + \frac{B_{II}^2}{E_y} + \frac{C_{II}^2}{G_{xy}} - \frac{2 A_{II} B_{II} \nu_{xy}}{E_x} - \frac{A_{II}^2 \nu_{xz}^2 E_z}{E_x^2} - \frac{B_{II}^2 \nu_{yz}^2 E_z}{E_y^2} - \frac{2 A_{II} B_{II} \nu_{xz} \nu_{yz} E_z}{E_x E_y} \right] \tag{9.9b}$$

$$D_3 = \frac{1}{4} \left[\frac{A_I A_{II}}{E_x} + \frac{B_I B_{II}}{E_y} + \frac{C_I C_{II}}{G_{xy}} - \frac{(A_I B_{II} + A_{II} B_I) \nu_{xy}}{E_x} - \frac{A_I A_{II} \nu_{xz}^2 E_z}{E_x^2} - \frac{B_I B_{II} \nu_{yz}^2 E_z}{E_y^2} - \frac{(A_I B_{II} + A_{II} B_I) \nu_{xz} \nu_{yz} E_z}{E_x E_y} \right] \tag{9.9c}$$

The solution of this function is complex and will therefore be periodical. The critical SED will then be the amplitude of this complex solution, which can be derived from the following expression.

$$S = D_1 K_I^2 + D_2 K_{II}^2 + 2 D_3 K_I K_{II} \tag{9.10}$$

By applying this equation with the unidirectional properties of M30SC-150/DT 120-34F [23], the amplitude of the SED function was determined to be $99.27 J/m^2$. The amplitude of the SED function was not directly equal to the SED measured in the laminate.

$$\frac{dW}{dV}_c = \frac{|S|}{\pi r} \tag{9.11}$$

A correction factor of πr was applied to compare the calculated critical SED with the measured critical SED of the experiment. The r in this function describes the field affected by the local stress intensity, as illustrated in figure 9.5. For brittle failure for the delamination behavior, meaning that there was no plastic stress intensity zone. The assumption that was used to determine the correction factor is that the greatest possible elastic stress intensity zone radius was half the material thickness. Applying this value as r delivered the lowest value of critical SED, which was a conservative approximation.

$$\frac{dW}{dV}_c = \frac{2|S|}{\pi t} \tag{9.12}$$

The minimum value for the calculated critical SED was $25280 J/m^3$. The measured critical SED measured during the fatigue test of specimen 18 was $27632 J/m^3$. The measured critical SED is 9.3% greater than the
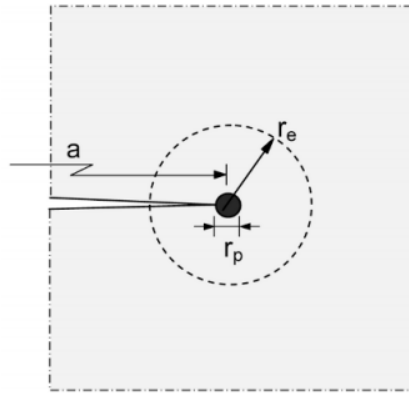
Figure 9.5: Definition of the elastic and plastic radius in a metal [13]

calculated critical SED. The difference between the calculated and measured critical SED is small, but more investigation is required to test if the assumption on the maximum radius of stress intensity affected zone is correct. Such a test can be performed by repeating the planar delamination experiment with specimen that vary in plate thickness.

10

CONCLUSION AND RECOMMENDATIONS

10.1. CONCLUSION

While the initial aim of this research was to investigate the methodology to measure planar delaminations in CFRP laminates, many new insights were obtained based on the outcomes of the experiment. The literature study aimed to investigate which responses of a material could be measured to track a delamination. The delamination growth could be measured through a theoretical criterion. Such a criterion that could describe the planar delamination growth is the SED criterion. When a criterion can be measured it can also be used to estimate planar delamination growth.

To investigate if the SED criterion could predict planar delamination growth, the planar transverse opening-load delamination experiment (Cameselle-Molares) was simulated. The simulation, that applied both CLT and the SED criterion, could predict the delamination shapes that resulted from this planar experiment. The simulation also gave insight on how the delamination propagation would change from uni-directional growth to growth in a planar manner.

To test if it is possible to measure delamination growth in a CFRP plate, three different methodologies were tested. Measuring the delamination with thermography and tracking the delamination with xy-plane curvature with DIC or creating a bond state map with the SED criterion which can also be measured with DIC. The combination of xy-plane curvature measurements with SED criterion bond state map resulted in an accurate measurement of the delamination.

The current common practice of a critical SERR was developed for the numerical VCCT method to predict delamination growth in free-edge delamination specimen. To see if this method can also predict delamination growth in a planar specimen which does not have free-edges, a numerical model was developed based on the performed quasi-static experiment. The results of this numerical demonstrated that the VCCT approach directly assumed planar growth and did not include the transverse growth behavior that observed in the quasi-static experiment. The planar delamination behavior was investigated by applying the physical SERR to see how the delamination resistance varies during the fatigue indentation experiment performed in this research, the planar transverse opening load-experiment and an impact study performed on quasi-static panels[12].

10.2. RECOMMENDATIONS

The current research has delivered on an initial answer on how planar delamination relates to the current coupon validation tests, however new questions came forward and the methodologies do require further research.

- The delamination propagation is only measured through DIC. Validation of the methodology for propagation tracking requires a second measurement technique. This measurement technique can be thermography. Passive thermography was able to measure the delamination growth. Continuous measurement of lock-in thermography does require fine-tuning of the heat source and frequency of measurements by the camera. This fine tuning should be further investigated.

- The analytical model, that investigated the transverse load opening delamination test, only included pure bending behavior. While the bending behavior does have a major influence on the delamination

94

shape that occurs in this test, the influence of the in-plane extension should also be included in the modeling process. It is therefore recommended to expand the analytical model with in-plane extension behavior.

- The numerical model that was developed for investigating the delamination area trend demonstrated the limitations of applying the SERR as delamination criteria for the planar delamination problem. The next step for predicting the delamination onset with the numerical model would require a change of the clamped boundary conditions which suits the behavior of the experiment more. With altered boundary conditions, the SED criterion should be applied as delamination criterion to see if the planar delamination trends match the experiment more.

- The relation between the SED and the quantification tests was initially developed by Daneshjoo [23]. The outcomes of this relation can be validated with DIC measurements similar to the ones made during this research.

- A correction factor was applied which depended on the assumption that stress intensity affect the material throughout the thickness, to calculate the critical SED. This assumption should be tested varying the plate thickness of the planar experiment.

- The physical SERR was applied to characterize the delamination resistance of the planar tests. The application of this theory would mean that there is a linear relation between the induced energy and the delamination growth. This relation should be explored further in future work.

BIBLIOGRAPHY

[1] *Astm standard d5528-94a - standard test method for mode i inter- laminar fracture toughness of unidirectional continuous fiber- reinforcedpolymermatrixcomposites.* (2007).

[2] *Astm standard d6671/d6671m - standard test method for mixed mode i-mode ii interlaminar fracture toughness of unidirectional fiber reinforced polymer matrix composites,* (2010).

[3] L. Amaral, R. Alderliesten, and R. Benedictus, *Towards a physics-based relationship for crack growth under different loading modes,* Engineering Fracture Mechanics **195,** 222 (2018).

[4] L. P. Canal, M. Alfano, and J. Botsis, *A multi-scale based cohesive zone model for the analysis of thickness scaling effect in fiber bridging,* Composites Science and Technology **139,** 90 (2017).

[5] J. J. Polaha, B. D. Davidson, R. C. Hudson, and A. Pieracci, *Effects of mode ratio, ply orientation and precracking on the delamination toughness of a laminated composite,* Journal of Reinforced Plastics and Composites **15,** 141 (1996).

[6] A. Cameselle-Molares, A. P. Vassilopoulos, and T. Keller, *Experimental investigation of two-dimensional delamination in GFRP laminates,* Engineering Fracture Mechanics **203,** 152 (2018).

[7] S. Guo, K.-T. Wan, and D. A. Dillard, *A bending-to-stretching analysis of the blister test in the presence of tensile residual stress,* International Journal of Solids and Structures **42,** 2771 (2005).

[8] A. Szekrényes, *Crack stability of fracture specimens used to test unidirectional fiber reinforced material,* Experimental Mechanics **50,** 473 (2009).

[9] G. Davies, P. Robinson, J. Robson, and D. Eady, *Shear driven delamination propagation in two dimensions,* Composites Part A: Applied Science and Manufacturing **28,** 757 (1997).

[10] L. Amaral, R. Alderliesten, and R. Benedictus, *Understanding mixed-mode cyclic fatigue delamination growth in unidirectional composites: An experimental approach,* Engineering Fracture Mechanics **180,** 161 (2017).

[11] A. Köllner, F. Forsbach, and C. Völlmecke, *Delamination buckling in composite plates: an analytical approach to predict delamination growth,* in *Advanced Structured Materials* (Springer International Publishing, 2019) pp. 241–255.

[12] G. Davies and X. Zhang, *Impact damage prediction in carbon composite structures,* International Journal of Impact Engineering **16,** 149 (1995).

[13] J. Schijve, *Fatigue of structures and materials* (Springer Science & Business Media, 2001).

[14] Delta-Tech, *M30sc-150-dt120-34 data collation,* (2020).

[15] Z. Daneshjoo, M. M. Shokrieh, M. Fakoor, R. Alderliesten, and D. Zarouchas, *Physics of delamination onset in unidirectional composite laminates under mixed-mode i/II loading,* Engineering Fracture Mechanics **211,** 82 (2019).

[16] E. P. Koumoulos, A.-F. Trompeta, R.-M. Santos, M. Martins, C. M. dos Santos, V. Iglesias, R. Böhm, G. Gong, A. Chiminelli, I. Verpoest, P. Kiekens, and C. A. Charitidis, *Research and development in carbon fibers and advanced high-performance composites supply chain in europe: A roadmap for challenges and the industrial uptake,* Journal of Composites Science **3,** 86 (2019).

[17] T. O'Brien, *Towards a damage tolerance philosophy for composite materials and structures,* in *Composite Materials: Testing and Design (Ninth Volume)* (ASTM, 1990) pp. 7–7–27.

[18] K. Shivakumar, *DOT/FAA/AR-08/47 - Assessment of Damage Tolerance Standard Test Methods and Development of Crack Growthand Delamination Database for Composite Structures*, Tech. Rep. (Federal Aviation Administration, 2009).

[19] *Iso 15024:2001. fibre-reinforced plastic composite-determination of mode i interlaminar fracture toughness, gic, for unidirectionally reinforced materials.* (2001).

[20] *Astm standard d7905/d7905m - standard test method for determination of the mode ii interlaminar fracture toughness of unidirectional fiber-reinforced polymer matrix composites,* (2019).

[21] *Iso 15114:2014 fibre-reinforced plastic composites determination of the mode ii fracture resistance for unidirectionally reinforced materials using the calibrated end-loaded split (c-els),* (2014).

[22] C. Meola, S. Boccardi, G. Carlomagno, N. Boffa, F. Ricci, G. Simeoli, and P. Russo, *Impact damaging of composites through online monitoring and non-destructive evaluation with infrared thermography,* NDT & E International **85**, 34 (2017).

[23] Z. Daneshjoo, L. Amaral, R. Alderliesten, M. Shokrieh, and M. Fakoor, *Development of a physics-based theory for mixed mode i/II delamination onset in orthotropic laminates,* Theoretical and Applied Fracture Mechanics **103**, 102303 (2019).

[24] P. A. Lagace, J. E. Williamson, P. W. Tsang, E. Wolf, and S. Thomas, *A preliminary proposition for a test method to measure (impact) damage resistance,* Journal of Reinforced Plastics and Composites **12**, 584 (1993).

[25] G. Davies, X. Zhang, G. Zhou, and S. Watson, *Numerical modelling of impact damage,* Composites **25**, 342 (1994).

[26] G. Schoeppner and S. Abrate, *Delamination threshold loads for low velocity impact on composite laminates,* Composites Part A: Applied Science and Manufacturing **31**, 903 (2000).

[27] F. Aymerich, F. Dore, and P. Priolo, *Simulation of multiple delaminations in impacted cross-ply laminates using a finite element model based on cohesive interface elements,* Composites Science and Technology **69**, 1699 (2009).

[28] S. Metoui, E. Pruliere, A. Ammar, and F. Dau, *A reduced model to simulate the damage in composite laminates under low velocity impact,* Computers & Structures **199**, 34 (2018).

[29] H. Chai and C. D. Babcock, *Two-dimensional modelling of compressive failure in delaminated laminates,* Journal of Composite Materials **19**, 67 (1985).

[30] B. Storåkers and B. Andersson, *Nonlinear plate theory applied to delamination in composites,* Journal of the Mechanics and Physics of Solids **36**, 689 (1988).

[31] W.-L. Yin and K. Jane, *Refined buckling and postbuckling analysis of two-dimensional delaminations—i. analysis and validation,* International Journal of Solids and Structures **29**, 591 (1992).

[32] K. Jane and W.-L. Yin, *Refined buckling and postbuckling analysis of two-dimensional delaminations—II. results for anisotropic laminates and conclusion,* International Journal of Solids and Structures **29**, 611 (1992).

[33] A. Köllner and C. Völlmecke, *Post-buckling behaviour and delamination growth characteristics of delaminated composite plates,* Composite Structures **203**, 777 (2018).

[34] K. Wang, L. Zhao, H. Hong, J. Zhang, and N. Hu, *An extended analytical model for predicting the compressive failure behaviors of composite laminate with an arbitrary elliptical delamination,* International Journal of Solids and Structures **185-186**, 439 (2020).

[35] G. Letchworth, *X-33 reusable launch vehicle demonstrator, spaceport and range,* in *AIAA SPACE 2011 Conference & Exposition* (American Institute of Aeronautics and Astronautics, 2011).

[36] M. Rinker, R. Krueger, and J. Ratcliffe, *Analysis of an aircraft honeycomb sandwich panel with circular face sheet/core disbond subjected to ground-air pressurization,* Tech. Rep. (NASA, 2013).

[37] Z. M. Chen, R. Krueger, and M. Rinker, *Face Sheet/Core Disbond Growth in Honeycomb Sandwich Panels Subjected to Ground-Air-Ground Pressurization and In-Plane Loading*, Tech. Rep. (NASA, 2015).

[38] A. Cameselle-Molares, A. P. Vassilopoulos, and T. Keller, *Two-dimensional quasi-static debonding in GFRP/balsa sandwich panels*, Composite Structures **215**, 391 (2019).

[39] A. Cameselle-Molares, A. P. Vassilopoulos, and T. Keller, *Two-dimensional fatigue debonding in GFRP/balsa sandwich panels*, International Journal of Fatigue **125**, 72 (2019).

[40] A. Cameselle-Molares, A. P. Vassilopoulos, J. Renart, A. Turon, and T. Keller, *Numerical simulation of two-dimensional in-plane crack propagation in FRP laminates*, Composite Structures **200**, 396 (2018).

[41] A. Cameselle-Molares, A. P. Vassilopoulos, J. Renart, A. Turon, and T. Keller, *Numerically-based method for fracture characterization of mode i-dominated two-dimensional delamination in FRP laminates*, Composite Structures **214**, 143 (2019).

[42] W.-X. Wang, M. Nakata, Y. Takao, and T. Matsubara, *Experimental investigation on test methods for mode II interlaminar fracture testing of carbon fiber reinforced composites*, Composites Part A: Applied Science and Manufacturing **40**, 1447 (2009).

[43] G. C. Sih, P. C. Paris, and G. R. Irwin, *On cracks in rectilinearly anisotropic bodies*, International Journal of Fracture Mechanics **1**, 189 (1965), cited By :1003.

[44] A. Griffith, *The phenomenon of rupture and flow in solids.* Phil, Trans, Roy. Soc. A221 (1921).

[45] G. Irwin, *Analysis of stresses and strains near the end of a crack traversing a plate.* American Socity of Mechanical Engineers, ASME **79**, 361 (1957), cited By :1.

[46] J. Pascoe, R. Alderliesten, and R. Benedictus, *Methods for the prediction of fatigue delamination growth in composites and adhesive bonds – a critical review*, Engineering Fracture Mechanics **112-113**, 72 (2013).

[47] J. Reeder, *An evaluation of mixed-mode delamination failure criteria*, Tech. Rep. (NASA, 1992).

[48] M. Benzeggagh and M. Kenane, *Measurement of mixed-mode delamination fracture toughness of uni-directional glass/epoxy composites with mixed-mode bending apparatus*, Composites Science and Technology **56**, 439 (1996).

[49] J. Reeder, *A bilinear failure criterion for mixed-mode delamination*, in *Eleventh Volume: Composite Materials—Testing and Design* (ASTM International, 1993) pp. 303–303–20.

[50] B. Davidson and R. Schapery, *Effect of finite width on deflection and energy release rate of an orthotropic double cantilever specimen*, Journal of Composite Materials **22**, 640 (1988).

[51] B. D. Manshadi, A. P. Vassilopoulos, and J. Botsis, *A combined experimental/numerical study of the scaling effects on mode i delamination of GFRP*, Composites Science and Technology **83**, 32 (2013).

[52] B. Davidson, *An analytical investigation of delamination front curvature in double cantilever beam specimens*, Journal of Composite Materials **24**, 1124 (1989).

[53] B. Davidson, R. Krüger, and M. König, *Effect of stacking sequence on energy release rate distributions in multidirectional dcb and enf specimens*, Engineering Fracture Mechanics **55**, 557 (1996).

[54] N. S. Choi, A. J. Kinloch, and J. G. Williams, *Delamination fracture of multidirectional carbon-fiber/epoxy composites under mode i, mode II and mixed-mode i/II loading*, Journal of Composite Materials **33**, 73 (1999).

[55] T. K. O'Brien, *Mixed-mode strain-energy-release rate effects on edge delamination of composites*, in *Effects of defects in composite materials* (ASTM International, 1984).

[56] M. L. Williams, *The continuum interpretation for fracture and adhesion*, Journal of Applied Polymer Science **13**, 29 (1969).

[57] Z. Suo and J. W. Hutchinson, *Interface crack between two elastic layers*, International Journal of Fracture **43**, 1 (1990).

[58] H. M. Jensen, *The blister test for interface toughness measurement,* Engineering Fracture Mechanics **40,** 475 (1991).

[59] H. M. Jensen, *Analysis of mode mixity in blister tests,* International Journal of Fracture **94,** 79 (1998).

[60] C. Jin, *Analysis of energy release rate and bending-to-stretching behavior in the shaft-loaded blister test,* International Journal of Solids and Structures **45,** 6485 (2008).

[61] M. Heitzmann, M. Hou, M. Veidt, and P. Falzon, *Influence of nonlinearities on the accuracy of the analytical solution for the shaft loaded blister test,* International Journal of Solids and Structures **48,** 1424 (2011).

[62] M. S. Islam and L. Tong, *Effects of initial blister radius and shaft diameter on energy release rate of metal–polymer composite coating,* International Journal of Adhesion and Adhesives **62,** 107 (2015).

[63] F. Lahuerta and R. P. L. Nijssen, *Energy dissipation in thermoset composites in mode i fatigue,* Mechanics of Advanced Materials and Structures **24,** 168 (2016).

[64] F. Lahuerta, R. Nijssen, F. van der Meer, and L. Sluys, *Infrared inspection of thick laminates during fatigue tests,* in *7th International Conference on Composites Testing and Model Identification (IMDEA), in* (2015) pp. 7–8.

[65] R. J. Greene, E. A. Patterson, and R. E. Rowlands, *Thermoelastic stress analysis,* Springer handbook of experimental solid mechanics , 743 (2008).

[66] J. Narayana Swamy, *Characterising delamination growth in composites under dynamic loading using infrared thermography: An experimental approach to use an infrared camera to monitor delamination growth in composite test samples,* Master's thesis, Delft University of Technology (2017).

[67] V. Munoz, B. Valès, M. Perrin, M. Pastor, H. Welemane, A. Cantarel, and M. Karama, *Damage detection in CFRP by coupling acoustic emission and infrared thermography,* Composites Part B: Engineering **85,** 68 (2016).

[68] S. Venkatachalam, S. M. K. Mohiddin, and H. Murthy, *Determination of damage evolution in CFRP subjected to cyclic loading using DIC,* Fatigue & Fracture of Engineering Materials & Structures **41,** 1412 (2018).

[69] Z.-X. Yang, J.-Y. Sun, Z.-H. Zhao, S.-Z. Li, and X.-T. He, *A closed-form solution of prestressed annular membrane internally-connected with rigid circular plate and transversely-loaded by central shaft,* Mathematics **8,** 521 (2020).

[70] D. Chen and L. Dai, *Delamination growth of laminated circular plates under in-plane loads and movable boundary conditions,* Communications in Nonlinear Science and Numerical Simulation **18,** 3238 (2013).

[71] D. Chen, C. Chen, Y. Fu, and L. Dai, *Growth of delamination for laminates circular plates subjected to transverse loads,* in *Volume 10: Mechanical Systems and Control, Parts A and B* (ASMEDC, 2009).

[72] J. Ye, *Structural and stress analysis: theories, tutorials and examples,* edited by T. . Francis (CRC Press, 2015).

[73] P. Davies, G. Sims, B. Blackman, A. Brunner, K. Kageyama, M. Hojo, K. Tanaka, G. Murri, C. Rousseau, B. Gieseke, and R. Martin, *Comparison of test configurations for determination of mode II interlaminar fracture toughness results from international collaborative test programme,* Plastics, Rubber and Composites **28,** 432 (1999).

[74] A. Argüelles, C. Rocandio, S. Rubiera, I. Viña, and J. Viña, *Influence of the test method on the characterization of the fatigue delamination behavior of a composite material under mixed mode i/II fracture,* Polymers **11,** 1788 (2019).

[75] A. Pereira and A. de Morais, *Mode i interlaminar fracture of carbon/epoxy multidirectional laminates,* Composites Science and Technology **64,** 2261 (2004).

[76] A. Pereira, A. de Morais, A. Marques, and P. de Castro, *Mode II interlaminar fracture of carbon/epoxy multidirectional laminates,* Composites Science and Technology **64**, 1653 (2004).

[77] X. Gong, A. Hurez, and G. Verchery, *On the determination of delamination toughness by using multidirectional DCB specimens,* Polymer Testing **29**, 658 (2010).

[78] *Astm standard e177-19:use of the terms precision and bias in astm test methods,* .

[79] *Practice for calculating sample size to estimate, with specified precision, the average for a characteristic of a lot or process,* (2017).

[80] N. K. Naik and K. S. Reddy, *Delaminated woven fabric composite plates under transverse quasi-static loading: Experimental studies,* Journal of Reinforced Plastics and Composites **21**, 869 (2002).

[81] M. McElroy, W. Jackson, R. Olsson, P. Hellström, S. Tsampas, and M. Pankow, *Interaction of delaminations and matrix cracks in a CFRP plate, part i: A test method for model validation,* Composites Part A: Applied Science and Manufacturing **103**, 314 (2017).

[82] *Astm standard e122:2017 standard practice for calculating sample size to estimate, with specified precision, the average for a characteristic of a lot or process,* (2017).

[83] M. W. McElroy, R. Gutkin, and M. Pankow, *Interaction of delaminations and matrix cracks in a CFRP plate, part II: Simulation using an enriched shell finite element model,* Composites Part A: Applied Science and Manufacturing **103**, 252 (2017).

[84] R. Alderliesten, *How proper similitude can improve our understanding of crack closure and plasticity in fatigue,* International Journal of Fatigue **82**, 263 (2016).

[85] E. Rybicki, D. Schmueser, and J. Fox, *An energy release rate approach for stable crack growth in the free-edge delamination problem,* Journal of Composite Materials **11**, 470 (1977).

[86] M. Kanninen, E. Rybicki, and H. Brinson, *A critical look at current applications of fracture mechanics to the failure of fibre-reinforced composites,* Composites **8**, 17 (1977).

A

C-Scans

Type of Laminate	C-scan number
QI00	8,9,10,11,12,13
QI30	1,2,3,4,5,6,7
QI45	14,15,16,17,18,19
ORT15	20
ORT30	21

Table A.1: The type of laminates with the corresponding c-scan numbers

(a)   (b)   (c)
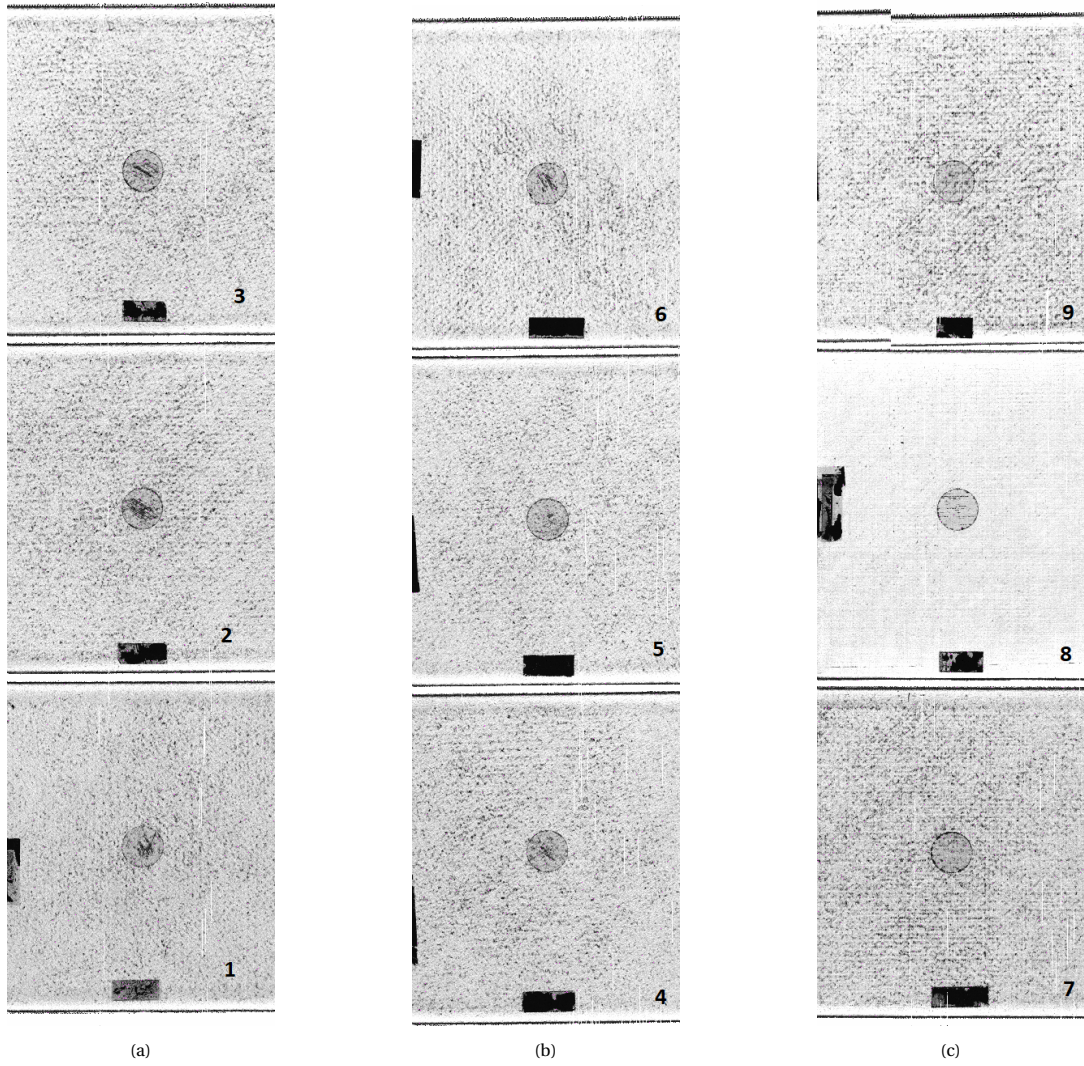
Figure A.1: First set of c-scans

(a)　　　　　　　　　　(b)　　　　　　　　　　(c)
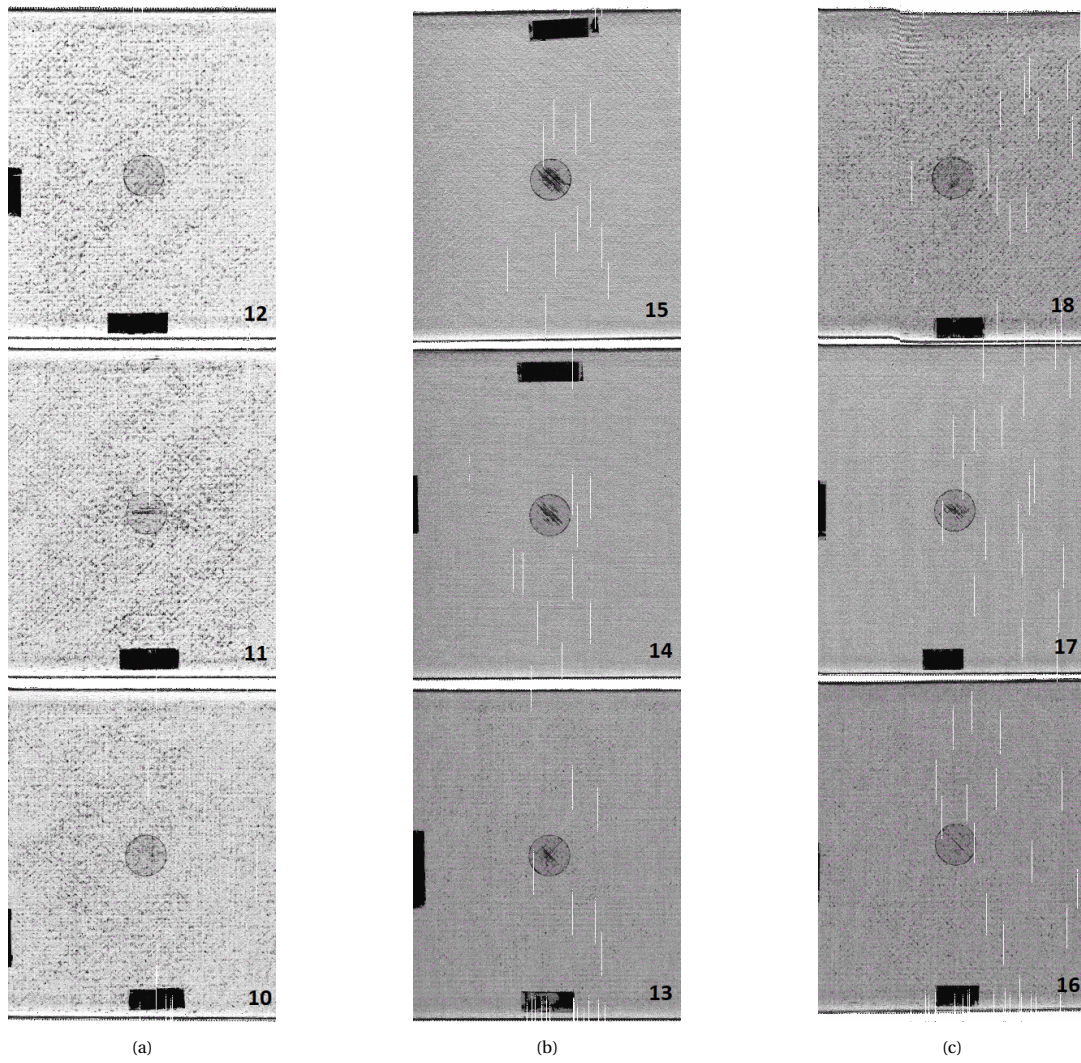
Figure A.2: Second set of c-scans
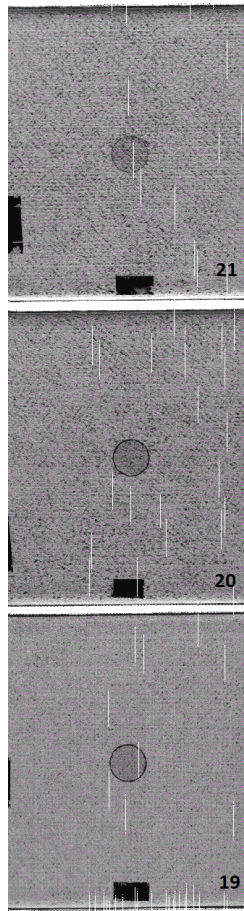
Figure A.3: Third set of c-scans

B

SCHEMATICS

□390,00
□370,00

385,00
350,00

195,00

40,00
5,00
0

12 x ⌀ 4,20 THRU ALL
M5 - 6H THRU ALL

10,00

0
5,00
40,00
195,00
350,00
385,00

635,00

10,00

195,00

654,71

25,00
20,00

Ø 6,80 ▽ 13,00
M8 - 6H ▽ 8,00

20,00
25,00

40,00
50,00
0

2 x Ø 4,20 ▽ 11,50
M5 ▽ 10,00

0
5,00
40,00
50,00

10,00

UNLESS OTHERWISE SPECIFIED: DIMENSIONS ARE IN MILLIMETERS SURFACE FINISH: TOLERANCES: LINEAR: ANGULAR:	FINISH:			DEBURR AND BREAK SHARP EDGES	DO NOT SCALE DRAWING	REVISION

	NAME	SIGNATURE	DATE			TITLE:
DRAWN						
CHK'D						
APPV'D						
MFG						
Q.A				MATERIAL: 3.3547 (EN-AW 5083)		DWG NO.

TITLE: L07-L23820 Part 1

DWG NO. ClampArm

A3

WEIGHT: 1456.99

SCALE:1:5

SHEET 1 OF 1

50,00

40,00

□ 50,00

40,00

30,00

5,00

5,00

4 x Ø 5,50 ▽ THRU

20,00

40,00

	NAME	SIGNATURE	DATE			TITLE:		
DRAWN								
CHK'D						**L07-L23820 Part 6**		
APPV'D								
MFG								
Q.A				MATERIAL:		DWG NO.		A4
				3.3545 (EN-AW 5086)		**ClampPlate**		
				WEIGHT: 127.81		SCALE:1:1	SHEET 1 OF 1	

UNLESS OTHERWISE SPECIFIED:
DIMENSIONS ARE IN MILLIMETERS
SURFACE FINISH:
TOLERANCES:
  LINEAR:
  ANGULAR:

FINISH:

DEBURR AND
BREAK SHARP
EDGES

DO NOT SCALE DRAWING

REVISION

□ 400,00

190,00

12 x Ø 6 THRU ALL

2,5

1,25

190,00

Ø25,00

A

A

SECTION A-A

M5

55,00

	NAME	SIGNATURE	DATE
DRAWN			
CHK'D			
APPV'D			
MFG			
Q.A			

TITLE:

L07-L23820 Part 5

MATERIAL:
Material <not specified>

DWG NO.

ThreadInsert

A4

WEIGHT: 1.08

SCALE:2:1

SHEET 1 OF 1

1 $\triangle$ 0

1 $\triangle$ 0
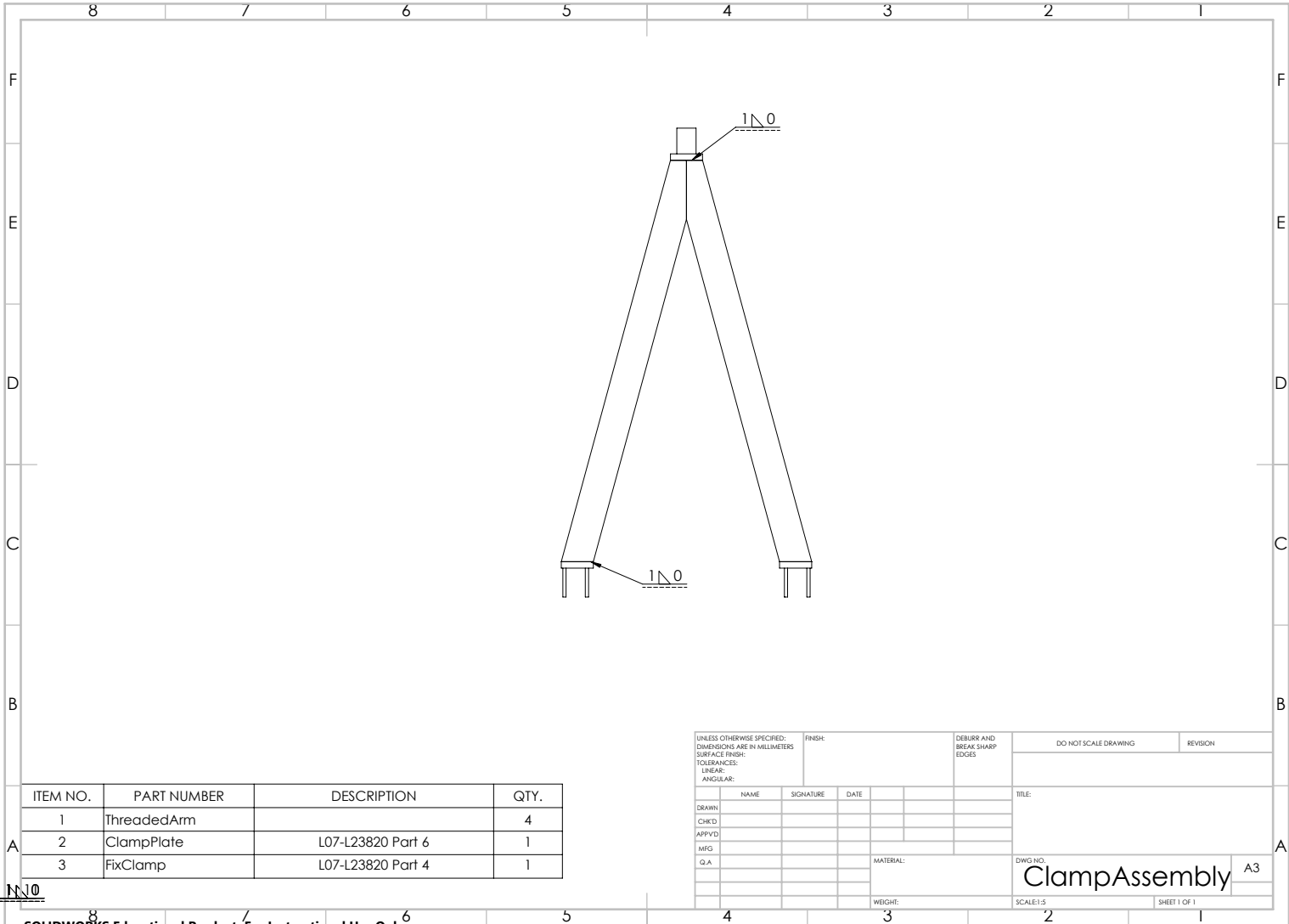
ITEM NO.	PART NUMBER	DESCRIPTION	QTY.
1	ThreadedArm		4
2	ClampPlate	L07-L23820 Part 6	1
3	FixClamp	L07-L23820 Part 4	1

N 10

UNLESS OTHERWISE SPECIFIED:	FINISH:		DEBURR AND BREAK SHARP EDGES	DO NOT SCALE DRAWING	REVISION
DIMENSIONS ARE IN MILLIMETERS SURFACE FINISH: TOLERANCES: LINEAR: ANGULAR:					

	NAME	SIGNATURE	DATE			TITLE:		
DRAWN								
CHK'D								
APPV'D								
MFG								
Q.A			MATERIAL:			DWG NO.		A3
						ClampAssembly		
			WEIGHT:			SCALE:1:5	SHEET 1 OF 1	

30°

38,3°

590,34

337,39

2109,61

2228,99

C

MATLAB CODE

Table C.1: Overview of the Matlab Code

Name Code	Purpose Code	Related to Chapter
DelaminationSimulation	To setup the complete delamination simulation of the planar DCB experiment	3
ExpandDelam	To govern the delamination propagation	3
DelaminationDirection	To calculate the delamination propagation direction	3
CalcSERR	To calculate the SERR after simulation	3
CalcLoad	To calculate the applied load after simulation	3
DrawSEDField	To plot the SED distribution	3
CycleAnalysis	To calculate the strain energy with the cyclic experiment data	7
FatigueArea	To calculate the delamination area with \{}ac{dic} data	7

Table of Contents

```
close all
clear
```

Determining the delamination behaviour of a planar problem with a pure Bending Model

```
%This is to test the hypothesis why a delamination transforms from a
%circular shape into a certain elliptical shape. The current
 hypothesis is that this behaviour depends on the flexural
%stiffness properties of the laminate. The material properties and
%mechanics is based on Cameselle-Molares Planar Delamination
 Experiment.
%The code will initialize the material properties, setup the
 displacement
%field and the determine the strain energy density functions. Then
 these
%inputs are given to the function ExpandDelam.m, which will generate
 the
%delamination length vectors as outcomes.
tic
```

Material Properties 50/50

```
E155 = 17.79e9;          %The Stiffness of the composite mat in the
 primary stiffness direction [Pa]
E255 = 17.79e9;          %The Stiffness of the composite mat in the
 secondary stiffness direction [Pa]
G1255 = 2.62e9;          %The in-plane Shear Stiffness of the composite
 mat [Pa]
v1255 = 0.19;            %Poisson's ratio of the composite mat [-/-]
tply155 = 3.33e-3;       %Thickness of the top mat [m]
tply255 = 3.53e-3;       %Thickness of the bottom mat [m]
%SED50 = 482.3232;       %Average Critical Strain Energy Density [J/
m^2]
```

```
SED50 = 3301;               %Average Critical Strain Energy Density [J/
m^2]
w55max = 32.8e-3/2;         %The maximum out-of-plane displacement of the
 experiment [m]

mat55 = [E155,E255,G1255,v1255];          %Material parameters
 vector of the mat
[A551,B551,D551] = ABD(mat55,tply155,0);   %ABD Matrix of the mat
D5511 = D551(1);                           %D11 Value of the mat [Nm]
D5512 = D551(2);                           %D12 Value of the mat [Nm]
D5516 = D551(3);                           %D16 Value of the mat [Nm]
D5522 = D551(5);                           %D22 Value of the mat [Nm]
D5526 = D551(6);                           %D26 Value of the mat [Nm]
D5566 = D551(9);                           %D66 Value of the mat [Nm]
```

Material Properties 60/40

```
E164 = 22.30e9;          %The Stiffness of the composite mat in the
 primary stiffness direction [Pa]
E264 = 14.86e9;          %The Stiffness of the composite mat in the
 secondary stiffness direction [Pa]
G1264 = 1.76e9;          %The in-plane Shear Stiffness of the composite
 mat [Pa]
v1264 = 0.23;            %Poisson's ratio of the composite mat [-/-]
tply164 = 3.05e-3;       %Thickness of the top mat [m]
tply264 = 3.06e-3;       %Thickness of the bottom mat [m]
%SED60 = 417.737;        %Average Critical Strain Energy Density [J/
m^2] SED
SED60 = 5761;            %Average Critical Strain Energy Density [J/
m^2]
w64max = 26e-3/2;        %The maximum out-of-plane displacement of the
 experiment [m]

mat64 = [E164,E264,G1264,v1264];          %Material parameters
 vector of the mat
[A641,B641,D641] = ABD(mat64,tply164,0);   %ABD Matrix of the mat
D6411 = D641(1);                           %D11 Value of the mat [Nm]
D6412 = D641(2);                           %D12 Value of the mat [Nm]
D6416 = D641(3);                           %D16 Value of the mat [Nm]
D6422 = D641(5);                           %D22 Value of the mat [Nm]
D6426 = D641(6);                           %D26 Value of the mat [Nm]
D6466 = D641(9);                           %D66 Value of the mat [Nm]
```

Material Properties 70/30

```
E173 = 24.28e9;          %The Stiffness of the composite mat in the
 primary stiffness direction [Pa]
E273 = 10.41e9;          %The Stiffness of the composite mat in the
 secondary stiffness direction [Pa]
G1273 = 2.56e9;          %The in-plane Shear Stiffness of the composite
 mat [Pa]
v1273 = 0.27;            %Poisson's ratio of the composite mat [-/-]
tply173 = 3.36e-3;       %Thickness of the top mat [m]
```

```
tply273 = 3.35e-3;        %Thickness of the bottom mat [m]
%SED70 = 587.8237;        %Average Critical Strain Energy Density [J/
m^2]
SED70 = 7943;             %Average Critical Strain Energy Density [J/
m^2]
w73max = 17.5e-3/2;       %The maximum out-of-plane displacement of the
 experiment [m]

mat73 = [E173,E273,G1273,v1273];          %Material parameters
 vector of the mat
[A731,B731,D731] = ABD(mat73,tply173,0);   %ABD Matrix of the mat
D7311 = D731(1);                           %D11 Value of the mat [Nm]
D7312 = D731(2);                           %D12 Value of the mat [Nm]
D7316 = D731(3);                           %D16 Value of the mat [Nm]
D7322 = D731(5);                           %D22 Value of the mat [Nm]
D7326 = D731(6);                           %D26 Value of the mat [Nm]
D7366 = D731(9);                           %D66 Value of the mat [Nm]
```

Material Properties 80/20

```
E182 = 27.03e9;          %The Stiffness of the composite mat in the
 primary stiffness direction [Pa]
E282 = 6.76e9;           %The Stiffness of the composite mat in the
 secondary stiffness direction [Pa]
G1282 = 2.51e9;          %The in-plane Shear Stiffness of the composite
 mat [Pa]
v1282 = 0.31;            %Poisson's ratio of the composite mat [-/-]
tply182 = 3.62e-3;       %Thickness of the top mat [m]
tply282 = 3.51e-3;       %Thickness of the bottom mat [m]
%SED80 = 686.6442;       %Average Critical Strain Energy Density [J/
m^2]
SED80 = 3075;            %Average Critical Strain Energy Density [J/
m^2]
w82max = 12.5e-3/2;      %The maximum out-of-plane displacement of the
 experiment [m]

mat82 = [E182,E282,G1282,v1282];          %Material parameters
 vector of the mat
[A821,B821,D821] = ABD(mat82,tply182,0);   %ABD Matrix of the mat
D8211 = D821(1);                           %D11 Value of the mat [Nm]
D8212 = D821(2);                           %D12 Value of the mat [Nm]
D8216 = D821(3);                           %D16 Value of the mat [Nm]
D8222 = D821(5);                           %D22 Value of the mat [Nm]
D8226 = D821(6);                           %D26 Value of the mat [Nm]
D8266 = D821(9);                           %D66 Value of the mat [Nm]
```

Setup the displacement Function

```
syms x y a b w0 rc                        %The symmetric functions
thet = atan(y/x);                         %The angle coordinate of
 the ellipse [rad]
re = ((a*b)*sqrt((x^2) + (y^2)))/sqrt(((a^2)*(y^2)) + ((b^2)*(x^2)));
  %The radius of the ellipse [m]
```

```
ac = 55e-3;                                  %The radius of the clamp
 connection [m]
w = w0*(1 - 3*((x/re)^2) + abs(2*((x/re)^3)))*(1 - 3*((y/re)^2) +
 abs(2*((y/re)^3)));    %The displacement field function [m]
wx = diff(w,x);                              %First derivative out-of-
plane displacement dw/dx [-]
wy = diff(w,y);                              %First derivative out-of-
plane displacement dw/dy [-]
wxx = diff(wx,x);                            %Second derivative out-of-
plane displacement d^2w/dx^2 [1/m]
wyy = diff(wy,y);                            %Second derivative out-of-
plane displacement d^2w/dy^2 [1/m]
wxy = diff(wx,y);                            %Second derivative out-of-
plane displacement d^2w/dxdy [1/m]
```

50/50 Mat Strain Energy Density Function

```
dU55 = (wxx^2)*D5511 + (wxx*wxy)*2*D5512 + (wxx*wxy)*4*D5516 +
 (wyy*wyy)*D5522 + (wyy*wxy)*4*D5526 + (wxy^2)*4*D5566;
dU55func = matlabFunction(dU55);               %The parameterised
 strain energy density function [J/m^3]
```

60/40 Mat Strain Energy Density Function

```
dU64 = (wxx^2)*D6411 + (wxx*wxy)*2*D6412 + (wxx*wxy)*4*D6416 +
 (wyy*wyy)*D6422 + (wyy*wxy)*4*D6426 + (wxy^2)*4*D6466;
dU64func = matlabFunction(dU64);               %The parameterised
 strain energy density function [J/m^3]
```

70/30 Mat Strain Energy Density Function

```
dU73 = (wxx^2)*D7311 + (wxx*wxy)*2*D7312 + (wxx*wxy)*4*D7316 +
 (wyy*wyy)*D7322 + (wyy*wxy)*4*D7326 + (wxy^2)*4*D7366;
dU73func = matlabFunction(dU73);               %The parameterised
 strain energy density function [J/m^3]
```

80/20 Mat Strain Energy Density Function

```
dU82 = (wxx^2)*D8211 + (wxx*wxy)*2*D8212 + (wxx*wxy)*4*D8216 +
 (wyy*wyy)*D8222 + (wyy*wxy)*4*D8226 + (wxy^2)*4*D8266;
dU82func = matlabFunction(dU82);               %The parameterised
 strain energy density function [J/m^3]
```

Determining Increments and Running the Simulation

```
n = 150;                              %The amount of increment steps [-]
a0 = 90e-3;                           %The initial primary direction
 delamination length [m]
```

```
b0 = 90e-3;                        %The initial secondary direction
 delamination length [m]
[a55,b55,thet55] = ExpandDelam(SED50,w55max,n,dU55func,a0,b0,ac);
[a64,b64,thet64] = ExpandDelam(SED60,w64max,n,dU64func,a0,b0,ac);
[a73,b73,thet73] = ExpandDelam(SED70,w73max,n,dU73func,a0,b0,ac);
[a82,b82,thet82] = ExpandDelam(SED80,w82max,n,dU82func,a0,b0,ac);

toc
```

Published with MATLAB® R2019a

```matlab
function [anew,bnew,thetav] =
 ExpandDelam(critSED,w0max,n,dUfunc,a,b,rc)
%This Function will increase the delamination size in the direction of
%maximum SED. This will occur the Strain Energy is greater than it's
 critical value.
%This means that this script has to loop until the Strain Energy
 Density is
%beneath the critical load again.
%Inputs: dUfunc     - Strain Energy Density Function [J/m^2]
%        critSED    - Critical Strain Energy Density [J/m^2]
%        w0max      - Maximum Out-of-Plane Displacement [m]
%        n          - Amount of increment steps [-]
%        a          - Initial Primary Direction Delamination Length
 [m]
%        b          - Initial Secondary Direction Delamination Length
 [m]
%        rc         - Radius of the clamp used in the experimental
 setup [m]
%Outputs:
%        anew       - Primary Direction Delamination Length Vector [m]
%        bnew       - Secondary Direction Delamination Length Vector
 [m]
%        thetav     - Critical Strain Energy Release Angle Vector
 [rad]
w0 = linspace(0,w0max,n);          %Out-of-plane displacement vector
 [m]
wn = @(w01,b,a,roff) w01/(1-(3*(2*roff/(a+b))^2)+(2*(2*roff/(a
+b))^3)); %Simulated Out-Of-Plane Displacement Value [m]
anew = zeros(1,n+1);               %Initializing Primary Direction
 Delamination Length Vector
bnew = zeros(1,n+1);               %Initializing Secondary Direction
 Delamination Length Vector
thetav = zeros(1,n+1);             %Initializing Critical Strain
 Energy Release Angle Vector
anew(1) = a;                       %Adding the Initial Primary
 Delamination Length Value [m]
bnew(1) = b;                       %Adding the Initial Secondary
 Delamination Length Value [m]
thetav(1) = 0;                     %Adding the Initial Critical
 Strain Energy Release Angle [rad]
for i = 1:n
ai = anew(i);                      %Reading this increment's primary
 delamination length [m]
bi = bnew(i);                      %Reading this increment's
 secondary delamination length [m]
wi = wn(w0(i),bi,ai,rc);           %Reading this increment's out-of-
plane displacement [m]
[mSED,theta] = DelaminationDirection(ai,bi,dUfunc,wi);     %Calculate
 the maximum strain energy density and direction in this increment
theta = max(theta);                                        %Assuring
 that a singular angle is determined [rad]
```

```matlab
    while mSED > critSED                                    %Check if
the current Strain Energy Density is greater than the criteria
        ai = ai + abs(ai*cos(theta)*0.01);                  %Grow the
delamination in the maximum direction [m]
        bi = bi + abs(bi*sin(theta)*0.01);                  %Grow the
delamination in the maximum direction [m]
        [mSED,theta] =
DelaminationDirection(ai,bi,dUfunc,wi); %Recalculate the maximum
Strain Energy Density and Direction
        theta = max(theta);
 %Resimplify the delamination direction [rad]
    end
anew(i+1) = ai;                                             %Index the
 outcome of the primary delamination length [m]
bnew(i+1) = bi;                                             %Index the
 outcome of the secondary delamination length [m]
thetav(i+1) = theta;                                        %Index the
 outcome of the delamination direction [rad]
end

end
```

Published with MATLAB® R2019a

```matlab
function [SEDCrit,theta] = DelaminationDirection(a,b,dUfunc,w0)
%This function calculates in which direction the strain energy density is
%the greatest at the delamination boundary
%Inputs: dUfunc - Strain Energy Density Function [J/m^2]
%        a      - This increment's Primary Direction Delamination
 Length [m]
%        b      - This increment's Secondary Direction Delamination
 Length [m]
%        w0     - This increment's Out-of-Plane Displacement [m]
%Outputs:
%        SEDCrit    - Critical Strain Energy Density [J/m^2]
%        theta      - Critical Strain Energy Release angle [rad]
thetv = linspace(0,pi,90);
  %The angle vector over half the ellipse spectrum [rad]
rethet = @(thet) (a*b)/sqrt((b*cos(thet))^2 + (a*sin(thet))^2);
  %The elliptical radius function [m]
SED = zeros(1,length(thetv));
  %Empty Strain Energy Density Vector
for i = 1:length(thetv)
    theti = thetv(i);
  %Selects the angle to check in this step [rad]
    rei = rethet(theti);
  %Calculates the radius of the delamination at this angle [m]
    xi = rei*cos(theti);
  %Calculates the x-coordinate of the delamination radius [m]
    yi = rei*sin(theti);
  %Calculates the y-coordinate of the delamination radius [m]
    SED(i) = dUfunc(a,b,w0,xi,yi);
  %Calculates the Strain Energy Density at this coordinate [J/m^2]
end
SEDCrit = max(SED);
  %Determines the maximum Strain Energy Density at this increment [J/
m^2]
icrit = find(SED == SEDCrit);
  %Locates the angle at which the maximum Strain Energy Density is
 apparent [rad]
theta = max(thetv(icrit));
  %Redus the angle to a singular answer [rad]
end
```

Published with MATLAB® R2019a

Table of Contents

```
%clear
```

Calc SERR Vectors%%

```
tic
```

Material Properties 50/50

```
E155 = 17.79e9;           %The Stiffness of the composite mat in the
 primary stiffness direction [Pa]
E255 = 17.79e9;           %The Stiffness of the composite mat in the
 secondary stiffness direction [Pa]
G1255 = 2.62e9;           %The in-plane Shear Stiffness of the composite
 mat [Pa]
v1255 = 0.19;             %Poisson's ratio of the composite mat [-/-]
tply155 = 3.33e-3;        %Thickness of the top mat [m]
tply255 = 3.53e-3;        %Thickness of the bottom mat [m]
w55max = 32.8e-3/2;        %The maximum out-of-plane displacement of
 the experiment [m]

mat55 = [E155,E255,G1255,v1255];          %Material parameters
 vector of the mat
[A551,B551,D551] = ABD(mat55,tply155,0);   %ABD Matrix of the mat
D5511 = D551(1);                           %D11 Value of the mat [Nm]
D5512 = D551(2);                           %D12 Value of the mat [Nm]
D5516 = D551(3);                           %D16 Value of the mat [Nm]
D5522 = D551(5);                           %D22 Value of the mat [Nm]
D5526 = D551(6);                           %D26 Value of the mat [Nm]
D5566 = D551(9);                           %D66 Value of the mat [Nm]
```

Material Properties 60/40

```
E164 = 22.30e9;          %The Stiffness of the composite mat in the
 primary stiffness direction [Pa]
E264 = 14.86e9;          %The Stiffness of the composite mat in the
 secondary stiffness direction [Pa]
G1264 = 1.76e9;          %The in-plane Shear Stiffness of the composite
 mat [Pa]
v1264 = 0.23;            %Poisson's ratio of the composite mat [-/-]
tply164 = 3.05e-3;       %Thickness of the top mat [m]
tply264 = 3.06e-3;       %Thickness of the bottom mat [m]
w64max = 26e-3/2;          %The maximum out-of-plane displacement of
 the experiment [m]

mat64 = [E164,E264,G1264,v1264];          %Material parameters
 vector of the mat
[A641,B641,D641] = ABD(mat64,tply164,0);     %ABD Matrix of the mat
D6411 = D641(1);                             %D11 Value of the mat [Nm]
D6412 = D641(2);                             %D12 Value of the mat [Nm]
D6416 = D641(3);                             %D16 Value of the mat [Nm]
D6422 = D641(5);                             %D22 Value of the mat [Nm]
D6426 = D641(6);                             %D26 Value of the mat [Nm]
D6466 = D641(9);                             %D66 Value of the mat [Nm]
```

Material Properties 70/30

```
E173 = 24.28e9;          %The Stiffness of the composite mat in the
 primary stiffness direction [Pa]
E273 = 10.41e9;          %The Stiffness of the composite mat in the
 secondary stiffness direction [Pa]
G1273 = 2.56e9;          %The in-plane Shear Stiffness of the composite
 mat [Pa]
v1273 = 0.27;            %Poisson's ratio of the composite mat [-/-]
tply173 = 3.36e-3;       %Thickness of the top mat [m]
tply273 = 3.35e-3;       %Thickness of the bottom mat [m]
w73max = 17.5e-3/2;        %The maximum out-of-plane displacement of
 the experiment [m]

mat73 = [E173,E273,G1273,v1273];          %Material parameters
 vector of the mat
[A731,B731,D731] = ABD(mat73,tply173,0);     %ABD Matrix of the mat
D7311 = D731(1);                             %D11 Value of the mat [Nm]
D7312 = D731(2);                             %D12 Value of the mat [Nm]
D7316 = D731(3);                             %D16 Value of the mat [Nm]
D7322 = D731(5);                             %D22 Value of the mat [Nm]
D7326 = D731(6);                             %D26 Value of the mat [Nm]
D7366 = D731(9);                             %D66 Value of the mat [Nm]
```

Material Properties 80/20

```
E182 = 27.03e9;          %The Stiffness of the composite mat in the
 primary stiffness direction [Pa]
```

```matlab
E282 = 6.76e9;            %The Stiffness of the composite mat in the
 secondary stiffness direction [Pa]
G1282 = 2.51e9;           %The in-plane Shear Stiffness of the composite
 mat [Pa]
v1282 = 0.31;             %Poisson's ratio of the composite mat [-/-]
tply182 = 3.62e-3;        %Thickness of the top mat [m]
tply282 = 3.51e-3;        %Thickness of the bottom mat [m]
w82max = 12.5e-3/2;        %The maximum out-of-plane displacement of
 the experiment [m]

mat82 = [E182,E282,G1282,v1282];          %Material parameters
 vector of the mat
[A821,B821,D821] = ABD(mat82,tply182,0);   %ABD Matrix of the mat
D8211 = D821(1);                           %D11 Value of the mat [Nm]
D8212 = D821(2);                           %D12 Value of the mat [Nm]
D8216 = D821(3);                           %D16 Value of the mat [Nm]
D8222 = D821(5);                           %D22 Value of the mat [Nm]
D8226 = D821(6);                           %D26 Value of the mat [Nm]
D8266 = D821(9);                           %D66 Value of the mat [Nm]
```

Setup the displacement Function

```matlab
syms x y a b w0 rc                         %The symmetric functions
thet = atan(y/x);                          %The angle coordinate of
 the ellipse [rad]
re = ((a*b)*sqrt((x^2) + (y^2)))/sqrt(((a^2)*(y^2)) + ((b^2)*(x^2)));
  %The radius of the ellipse [m]
ac = 55e-3;                                %The radius of the clamp
 connection [m]
w = w0*(1 - 3*((x/re)^2) + abs(2*((x/re)^3)))*(1 - 3*((y/re)^2) +
 abs(2*((y/re)^3)));   %The displacement field function [m]
```

For changing to clamping conditions

```matlab
avg = @(a,b) (b+a)/2;                      %The average
 delamination length
w0n = @(w0,a,b)w0/(1-(3*(ac/avg(a,b))^2)+(2*(ac/avg(a,b))^3)); %The
 altered out-of-plane displacment to place the clamp radius at the
 out-of-plane displacement height

wx = diff(w,x);                            %First derivative out-of-
plane displacement dw/dx [-]
wy = diff(w,y);                            %First derivative out-of-
plane displacement dw/dy [-]
wxx = diff(wx,x);                          %Second derivative out-of-
plane displacement d^2w/dx^2 [1/m]
wyy = diff(wy,y);                          %Second derivative out-of-
plane displacement d^2w/dy^2 [1/m]
wxy = diff(wx,y);                          %Second derivative out-of-
plane displacement d^2w/dxdy [1/m]
```

For simplifying the Von Karman Equations

wxxx = diff(wxx,x); wxxxx = diff(wxxx,x); wxxy = diff(wxx,y); wxxyy = diff(wxxy,y); wyyy = diff(wyy,y); wyyyy = diff(wyyy,y);

50/50 Mat Strain Energy and Load Function

```
dU55 = (wxx^2)*D5511 + (wxx*wxy)*2*D5512 + (wxx*wxy)*4*D5516 +
 (wyy*wyy)*D5522 + (wyy*wxy)*4*D5526 + (wxy^2)*4*D5566;
dU55func = matlabFunction(dU55);                %The parameterised
 strain energy density function [J/m^3]
P55 = matlabFunction(dU55func(a,b,w0,1e-5,1e-5));   %The parameterised
 load function [N]
load('a55.mat');
load('b55.mat');
Gc55 = DetermineSERR(dU55func,a55,a55,ac,w55max);
```

60/40 Mat

```
dU64 = (wxx^2)*D6411 + (wxx*wxy)*2*D6412 + (wxx*wxy)*4*D6416 +
 (wyy*wyy)*D6422 + (wyy*wxy)*4*D6426 + (wxy^2)*4*D6466;
dU64func = matlabFunction(dU64);                %The parameterised
 strain energy density function [J/m^3]
P64 = matlabFunction(dU64func(a,b,w0,1e-5,1e-5));   %The parameterised
 load function [N]
load('a64.mat');
load('b64.mat');
Gc64 = DetermineSERR(dU64func,a64,b64,ac,w64max);
```

70/30 Mat

```
dU73 = (wxx^2)*D7311 + (wxx*wxy)*2*D7312 + (wxx*wxy)*4*D7316 +
 (wyy*wyy)*D7322 + (wyy*wxy)*4*D7326 + (wxy^2)*4*D7366;
dU73func = matlabFunction(dU73);                %The parameterised
 strain energy density function [J/m^3]
P73 = matlabFunction(dU73func(a,b,w0,1e-5,1e-5));   %The parameterised
 load function [N]
load('a73.mat');
load('b73.mat');
Gc73 = DetermineSERR(dU73func,a73,b73,ac,w73max);
```

80/20 Mat

```
dU82 = (wxx^2)*D8211 + (wxx*wxy)*2*D8212 + (wxx*wxy)*4*D8216 +
 (wyy*wyy)*D8222 + (wyy*wxy)*4*D8226 + (wxy^2)*4*D8266;
dU82func = matlabFunction(dU82);                %The parameterised
 strain energy density function [J/m^3]
P82 = matlabFunction(dU82func(a,b,w0,1e-5,1e-5));   %The parameterised
 load function [N]
load('a82.mat');
```

```
load('b82.mat');
Gc82 = DetermineSERR(dU82func,a82,b82,ac,w82max);
toc
```

Plotting Gc mat 50/50

```
w55vec = linspace(1,(w55max*1000),length(a55));
figure
hold on
grid on
Gc55(Gc55 == 0) = nan;
%Gc55(Gc55 <= 0) = nan;
rem55 = isnan(Gc55);
Gc55 = Gc55(~rem55);
w55vec = w55vec(~rem55);
%Gc55s = smooth(Gc55);
Gc55c = fit(w55vec',Gc55','poly3','normalize','on');
plot(Gc55c,w55vec,Gc55,'predfunc')
%plot(w55vec,Gc55s);
title('SERR of 50/50 Composite Mat Simulated, 95% Confidence
 interval');
ylabel('SERR [^{J}/_{m^2}]');
xlabel('Out of Plane Displacement [mm]');
```

Plotting Gc mat 60/40

```
w64vec = linspace(1,(w64max*1000),length(a64));
figure
hold on
grid on
%Gc64(Gc64 <= 0) = nan;
Gc64(Gc64 == 0) = nan;
rem64 = isnan(Gc64);
Gc64 = Gc64(~rem64);
w64vec = w64vec(~rem64);
%Gc64s = smooth(Gc64);
Gc64c = fit(w64vec',Gc64','poly3','normalize','on');
plot(Gc64c,w64vec,Gc64,'predfunc');
%scatter(w64vec,Gc64);
title('SERR of 60/40 Composite Mat Simulated, 95% Confidence
 interval');
ylabel('SERR [^{J}/_{m^2}]');
xlabel('Out of Plane Displacement [mm]');
```

Plotting Gc mat 70/30

```
w73vec = linspace(1,(w73max*1000),length(a73));
figure
hold on
grid on
Gc73(Gc73 == 0) = nan;
%Gc73(Gc73 <= 0) = nan;
```

```matlab
%scatter(w73vec,Gc73);
rem73 = isnan(Gc73);
Gc73 = Gc73(~rem73);
w73vec = w73vec(~rem73);
%Gc73s = smooth(Gc73);
Gc73c = fit(w73vec',Gc73','poly3','normalize','on');
plot(Gc73c,w73vec,Gc73,'predfunc');
title('SERR of 70/30 Composite Mat Simulated, 95% Confidence
 interval');
ylabel('SERR [^{J}/_{m^2}]');
xlabel('Out of Plane Displacement [mm]');
```

Plotting Gc mat 80/20

```matlab
w82vec = linspace(1,(w82max*1000),length(a82));
figure
hold on
grid on
Gc82(Gc82 == 0) = nan;
rem82 = isnan(Gc82);
Gc82 = Gc82(~rem82);
w82vec = w82vec(~rem82);
Gc82c = fit(w82vec',Gc82','poly3','normalize','on');
plot(Gc82c,w82vec,Gc82,'predfunc');
title('SERR of 80/20 Composite Mat Simulated, 95% Confidence
 interval');
ylabel('SERR [^{J}/_{m^2}]');
xlabel('Out of Plane Displacement [mm]');
```

Published with MATLAB® R2019a

Table of Contents

```
%clear
```

Calc Load Displament Calculations%%

```
tic
```

Material Properties 50/50

```
E155 = 17.79e9;          %The Stiffness of the composite mat in the
 primary stiffness direction [Pa]
E255 = 17.79e9;          %The Stiffness of the composite mat in the
 secondary stiffness direction [Pa]
G1255 = 2.62e9;          %The in-plane Shear Stiffness of the composite
 mat [Pa]
v1255 = 0.19;            %Poisson's ratio of the composite mat [-/-]
tply155 = 3.33e-3;       %Thickness of the top mat [m]
tply255 = 3.53e-3;       %Thickness of the bottom mat [m]
w55max = 32.8e-3/2;       %The maximum out-of-plane displacement of
 the experiment [m]

mat55 = [E155,E255,G1255,v1255];          %Material parameters
 vector of the mat
[A551,B551,D551] = ABD(mat55,tply155,0);   %ABD Matrix of the mat
D5511 = D551(1);                           %D11 Value of the mat [Nm]
D5512 = D551(2);                           %D12 Value of the mat [Nm]
D5516 = D551(3);                           %D16 Value of the mat [Nm]
D5522 = D551(5);                           %D22 Value of the mat [Nm]
D5526 = D551(6);                           %D26 Value of the mat [Nm]
D5566 = D551(9);                           %D66 Value of the mat [Nm]
```

Material Properties 60/40

```
E164 = 22.30e9;          %The Stiffness of the composite mat in the
 primary stiffness direction [Pa]
E264 = 14.86e9;          %The Stiffness of the composite mat in the
 secondary stiffness direction [Pa]
G1264 = 1.76e9;          %The in-plane Shear Stiffness of the composite
 mat [Pa]
v1264 = 0.23;            %Poisson's ratio of the composite mat [-/-]
tply164 = 3.05e-3;       %Thickness of the top mat [m]
tply264 = 3.06e-3;       %Thickness of the bottom mat [m]
w64max = 26e-3/2;          %The maximum out-of-plane displacement of
 the experiment [m]

mat64 = [E164,E264,G1264,v1264];          %Material parameters
 vector of the mat
[A641,B641,D641] = ABD(mat64,tply164,0);    %ABD Matrix of the mat
D6411 = D641(1);                            %D11 Value of the mat [Nm]
D6412 = D641(2);                            %D12 Value of the mat [Nm]
D6416 = D641(3);                            %D16 Value of the mat [Nm]
D6422 = D641(5);                            %D22 Value of the mat [Nm]
D6426 = D641(6);                            %D26 Value of the mat [Nm]
D6466 = D641(9);                            %D66 Value of the mat [Nm]
```

Material Properties 70/30

```
E173 = 24.28e9;          %The Stiffness of the composite mat in the
 primary stiffness direction [Pa]
E273 = 10.41e9;          %The Stiffness of the composite mat in the
 secondary stiffness direction [Pa]
G1273 = 2.56e9;          %The in-plane Shear Stiffness of the composite
 mat [Pa]
v1273 = 0.27;            %Poisson's ratio of the composite mat [-/-]
tply173 = 3.36e-3;       %Thickness of the top mat [m]
tply273 = 3.35e-3;       %Thickness of the bottom mat [m]
w73max = 17.5e-3/2;        %The maximum out-of-plane displacement of
 the experiment [m]

mat73 = [E173,E273,G1273,v1273];          %Material parameters
 vector of the mat
[A731,B731,D731] = ABD(mat73,tply173,0);    %ABD Matrix of the mat
D7311 = D731(1);                            %D11 Value of the mat [Nm]
D7312 = D731(2);                            %D12 Value of the mat [Nm]
D7316 = D731(3);                            %D16 Value of the mat [Nm]
D7322 = D731(5);                            %D22 Value of the mat [Nm]
D7326 = D731(6);                            %D26 Value of the mat [Nm]
D7366 = D731(9);                            %D66 Value of the mat [Nm]
```

Material Properties 80/20

```
E182 = 27.03e9;          %The Stiffness of the composite mat in the
 primary stiffness direction [Pa]
```

```matlab
E282 = 6.76e9;              %The Stiffness of the composite mat in the
 secondary stiffness direction [Pa]
G1282 = 2.51e9;             %The in-plane Shear Stiffness of the composite
 mat [Pa]
v1282 = 0.31;               %Poisson's ratio of the composite mat [-/-]
tply182 = 3.62e-3;          %Thickness of the top mat [m]
tply282 = 3.51e-3;          %Thickness of the bottom mat [m]
w82max = 12.5e-3/2;           %The maximum out-of-plane displacement of
 the experiment [m]

mat82 = [E182,E282,G1282,v1282];           %Material parameters
 vector of the mat
[A821,B821,D821] = ABD(mat82,tply182,0);   %ABD Matrix of the mat
D8211 = D821(1);                           %D11 Value of the mat [Nm]
D8212 = D821(2);                           %D12 Value of the mat [Nm]
D8216 = D821(3);                           %D16 Value of the mat [Nm]
D8222 = D821(5);                           %D22 Value of the mat [Nm]
D8226 = D821(6);                           %D26 Value of the mat [Nm]
D8266 = D821(9);                           %D66 Value of the mat [Nm]
```

Setup the displacement Function

```matlab
syms x y a b w0 rc                         %The symmetric functions
thet = atan(y/x);                          %The angle coordinate of
 the ellipse [rad]
re = ((a*b)*sqrt((x^2) + (y^2)))/sqrt(((a^2)*(y^2)) + ((b^2)*(x^2)));
  %The radius of the ellipse [m]
ac = 55e-3;                                %The radius of the clamp
 connection [m]
w = w0*(1 - 3*((x/re)^2) + abs(2*((x/re)^3)))*(1 - 3*((y/re)^2) +
 abs(2*((y/re)^3)));    %The displacement field function [m]
```

For changing to clamping conditions

```matlab
avg = @(a,b) (b+a)/2;                        %The average
 delamination length
w0n = @(w0,a,b)w0/(1-(3*(ac/avg(a,b))^2)+(2*(ac/avg(a,b))^3)); %The
 altered out-of-plane displacment to place the clamp radius at the
 out-of-plane displacement height

wx = diff(w,x);                           %First derivative out-of-
plane displacement dw/dx [-]
wy = diff(w,y);                           %First derivative out-of-
plane displacement dw/dy [-]
wxx = diff(wx,x);                         %Second derivative out-of-
plane displacement d^2w/dx^2 [1/m]
wyy = diff(wy,y);                         %Second derivative out-of-
plane displacement d^2w/dy^2 [1/m]
wxy = diff(wx,y);                         %Second derivative out-of-
plane displacement d^2w/dxdy [1/m]
```

50/50 Mat Strain Energy and Load Function

```
dU55 = (wxx^2)*D5511 + (wxx*wxy)*2*D5512 + (wxx*wxy)*4*D5516 +
 (wyy*wyy)*D5522 + (wyy*wxy)*4*D5526 + (wxy^2)*4*D5566;
dU55func = matlabFunction(dU55);                  %The parameterised
 strain energy density function [J/m^3]
P55func = matlabFunction(dU55func(a,b,w0,1e-5,1e-5));    %The
 parameterised load function [N]
load('a55.mat');
load('b55.mat');
P55 = DetermineLoad(P55func,a55,b55,w55max,ac);
```

60/40 Mat

```
dU64 = (wxx^2)*D6411 + (wxx*wxy)*2*D6412 + (wxx*wxy)*4*D6416 +
 (wyy*wyy)*D6422 + (wyy*wxy)*4*D6426 + (wxy^2)*4*D6466;
dU64func = matlabFunction(dU64);                  %The parameterised
 strain energy density function [J/m^3]
P64func = matlabFunction(dU64func(a,b,w0,1e-5,1e-5));    %The
 parameterised load function [N]
load('a64.mat');
load('b64.mat');
P64 = DetermineLoad(P64func,a64,b64,w64max,ac);
```

70/30 Mat

```
dU73 = (wxx^2)*D7311 + (wxx*wxy)*2*D7312 + (wxx*wxy)*4*D7316 +
 (wyy*wyy)*D7322 + (wyy*wxy)*4*D7326 + (wxy^2)*4*D7366;
dU73func = matlabFunction(dU73);                  %The parameterised
 strain energy density function [J/m^3]
P73func = matlabFunction(dU73func(a,b,w0,1e-5,1e-5));    %The
 parameterised load function [N]
load('a73.mat');
load('b73.mat');
P73 = DetermineLoad(P73func,a73,b73,w73max,ac);
```

80/20 Mat

```
dU82 = (wxx^2)*D8211 + (wxx*wxy)*2*D8212 + (wxx*wxy)*4*D8216 +
 (wyy*wyy)*D8222 + (wyy*wxy)*4*D8226 + (wxy^2)*4*D8266;
dU82func = matlabFunction(dU82);                  %The parameterised
 strain energy density function [J/m^3]
P82func = matlabFunction(dU82func(a,b,w0,1e-5,1e-5));    %The
 parameterised load function [N]
load('a82.mat');
load('b82.mat');
P82 = DetermineLoad(P82func,a82,b82,w82max,ac);
toc
```

Plotting Gc mat 50/50

```matlab
w55vec = linspace(1,(w55max*1000),length(a55));
figure
hold on
grid on
plot(w55vec,P55);
title('Load of 50/50 Composite Mat Simulated');
ylabel('Center Load [N]');
xlabel('Out of Plane Displacement [mm]');
```

Plotting Gc mat 60/40

```matlab
w64vec = linspace(1,(w64max*1000),length(a64));
figure
hold on
grid on
plot(w64vec,P64);
title('Load of 60/40 Composite Mat Simulated');
ylabel('Center Load [N]');
xlabel('Out of Plane Displacement [mm]');
```

Plotting Gc mat 70/30

```matlab
w73vec = linspace(1,(w73max*1000),length(a73));
figure
hold on
grid on
plot(w73vec,P73);
title('Load of 70/30 Composite Mat Simulated');
ylabel('Center Load [N]');
xlabel('Out of Plane Displacement [mm]');
```

Plotting Gc mat 80/20

```matlab
w82vec = linspace(1,(w82max*1000),length(a82));
figure
hold on
grid on
plot(w82vec,P82);
title('Load of 80/20 Composite Mat Simulated');
ylabel('Center Load [N]');
xlabel('Out of Plane Displacement [mm]');
```

Published with MATLAB® R2019a

Table of Contents

```
close all
clear
```

Determining the delamination behaviour of a planar problem with Bending Stretching Model

This Script is made to plot the displacement field and the SED field of the current problem.

```
%THIS CODE IS WORKING PROPERLY
```

Material Properties 50/50

```
E155 = 17.79e9;
E255 = 17.79e9;
G1255 = 2.62e9;
v1255 = 0.19;
tply155 = 3.33e-3;
tply255 = 3.53e-3;

mat55 = [E155,E255,G1255,v1255];
[A551,B551,D551] = ABD(mat55,tply155,0);
D5511 = D551(1);
D5512 = D551(2);
D5516 = D551(3);
D5522 = D551(5);
D5526 = D551(6);
D5566 = D551(9);
```

```
%ABD552 = ABD(mat55,tply155,0);
```

Material Properties 60/40

```
E164 = 22.30e9;
E264 = 14.86e9;
G1264 = 1.76e9;
v1264 = 0.23;
tply164 = 3.05e-3;
tply264 = 3.06e-3;

mat64 = [E164,E264,G1264,v1264];
[A641,B641,D641] = ABD(mat64,tply164,0);
D6411 = D641(1);
D6412 = D641(2);
D6416 = D641(3);
D6422 = D641(5);
D6426 = D641(6);
D6466 = D641(9);
```

Material Properties 70/30

```
E173 = 24.28e9;
E273 = 10.41e9;
G1273 = 2.56e9;
v1273 = 0.27;
tply173 = 3.36e-3;
tply273 = 3.35e-3;

mat73 = [E173,E273,G1273,v1273];
[A731,B731,D731] = ABD(mat73,tply173,0);
D7311 = D731(1);
D7312 = D731(2);
D7316 = D731(3);
D7322 = D731(5);
D7326 = D731(6);
D7366 = D731(9);
```

Material Properties 80/20

```
E182 = 27.03e9;
E282 = 6.76e9;
G1282 = 2.51e9;
v1282 = 0.31;
tply182 = 3.62e-3;
tply282 = 3.51e-3;

mat82 = [E182,E282,G1282,v1282];
[A821,B821,D821] = ABD(mat82,tply182,0);
D8211 = D821(1);
D8212 = D821(2);
D8216 = D821(3);
```

```
D8222 = D821(5);
D8226 = D821(6);
D8266 = D821(9);
```

Central W0 value is only working for x (due to tan function issues)

```
syms x y a b w0 rc                        %The symmetric functions

b0 = 90e-3;
%b0 = 110e-3;
a0 = 90e-3;
ac = 55e-3;




re = ((a*b)*sqrt((x^2) + (y^2)))/sqrt(((a^2)*(y^2)) + ((b^2)*(x^2)));
  %The radius of the ellipse [m]
%w = w0*(1 - 3*((x/re)^2) + 2*((x/re)^3))*(1 - 3*((y/re)^2) + 2*((y/
re)^3));   %The displacement field function [m]
w = w0*(1 - 3*((x/re)^2) + abs(2*((x/re)^3)))*(1 - 3*((y/re)^2) +
 abs(2*((y/re)^3)));
```

Offset Values

```
w0551 = 5.75e-3/2;
avg551 = (b0+a0)/2;
w0n551 = w0551/(1-(3*(ac/avg551)^2)+(2*(ac/avg551)^3));
%w0n551 = w0551;

w0641 = 6.875e-3/2;
avg641 = (b0+a0)/2;
w0n641 = w0641/(1-(3*(ac/avg641)^2)+(2*(ac/avg641)^3));
%w0n641 = w0641;

w0731 = 6.185e-3/2;
avg731 = (b0+a0)/2;
w0n731 = w0731/(1-(3*(ac/avg731)^2)+(2*(ac/avg731)^3));
%w0n731 = w0731;

w0821 = 4.07e-3/2;
avg821 = (b0+a0)/2;
w0n821 = w0821/(1-(3*(ac/avg821)^2)+(2*(ac/avg821)^3));
%w0n821 = w0821;
```

Writing out the derivatives for the displacement function

```
wx = diff(w,x);                           %First derivative out-of-
plane displacement dw/dx [-]
```

```matlab
wy = diff(w,y);                          %First derivative out-of-
plane displacement dw/dy [-]
wxx = diff(wx,x);                        %Second derivative out-of-
plane displacement d^2w/dx^2 [1/m]
wyy = diff(wy,y);                        %Second derivative out-of-
plane displacement d^2w/dy^2 [1/m]
wxy = diff(wx,y);                        %Second derivative out-of-
plane displacement d^2w/dxdy [1/m]
```

50/50 Mat

```matlab
dU55 = (wxx^2)*D5511 + (wxx*wxy)*2*D5512 + (wxx*wxy)*4*D5516 +
 (wyy*wyy)*D5522 + (wyy*wxy)*4*D5526 + (wxy^2)*4*D5566;
dU55func = matlabFunction(dU55);
```

60/40 Mat

```matlab
dU64 = (wxx^2)*D6411 + (wxx*wxy)*2*D6412 + (wxx*wxy)*4*D6416 +
 (wyy*wyy)*D6422 + (wyy*wxy)*4*D6426 + (wxy^2)*4*D6466;
dU64func = matlabFunction(dU64);
```

70/30 Mat

```matlab
dU73 = (wxx^2)*D7311 + (wxx*wxy)*2*D7312 + (wxx*wxy)*4*D7316 +
 (wyy*wyy)*D7322 + (wyy*wxy)*4*D7326 + (wxy^2)*4*D7366;
dU73func = matlabFunction(dU73);
```

80/20 Mat

```matlab
dU82 = (wxx^2)*D8211 + (wxx*wxy)*2*D8212 + (wxx*wxy)*4*D8216 +
 (wyy*wyy)*D8222 + (wyy*wxy)*4*D8226 + (wxy^2)*4*D8266;
dU82func = matlabFunction(dU82);                  %The parameterised
 strain energy density function [J/m^3]
```

Setting up the angle function

```matlab
syms thet
thetv = linspace(-pi,pi,180);
rethet = (a*b)/sqrt((b*cos(thet))^2 + (a*sin(thet))^2);
refunc = matlabFunction(rethet);
```

Writing out the SED Plot 50/50 Offset

```matlab
SED55 = zeros(1,length(thetv));
for i = 1:length(thetv)
    theti = thetv(i);
    rei = refunc(a0,b0,theti);
    xi = rei*cos(theti);
    yi = rei*sin(theti);
    SED55(i) = dU55func(a0,b0,w0n551,xi,yi);
```

```matlab
    end
    figure
    hold on
    plot(thetv,SED55,'lineWidth',2);
    xlabel('Angle in [Rad]');
    ylabel('Strain Energy Density Delamination Boundary [J/m^3]');
    title('SED around the delamination boundary at the offset 50/50');
```

Writing out the SED Plot 60/40 Offset

```matlab
    SED64 = zeros(1,length(thetv));
    for i = 1:length(thetv)
        theti = thetv(i);
        rei = refunc(a0,b0,theti);
        xi = rei*cos(theti);
        yi = rei*sin(theti);
        SED64(i) = dU64func(a0,b0,w0n641,xi,yi);
    end
    figure
    hold on
    plot(thetv,SED64,'lineWidth',2);
    xlabel('Angle in [Rad]');
    ylabel('Strain Energy Density Delamination Boundary [J/m^3]');
    title('SED around the delamination boundary at the offset 60/40');
```

Writing out the SED Plot 70/30 Offset

```matlab
    SED73 = zeros(1,length(thetv));
    for i = 1:length(thetv)
        theti = thetv(i);
        rei = refunc(a0,b0,theti);
        xi = rei*cos(theti);
        yi = rei*sin(theti);
        SED73(i) = dU73func(a0,b0,w0n731,xi,yi);
    end
    figure
    hold on
    plot(thetv,SED73,'lineWidth',2);
    xlabel('Angle in [Rad]');
    ylabel('Strain Energy Density Delamination Boundary [J/m^3]');
    title('SED around the delamination boundary at the offset 70/30');
```

Writing out the SED Plot 80/20 Offset

```matlab
    SED82 = zeros(1,length(thetv));
    for i = 1:length(thetv)
        theti = thetv(i);
        rei = refunc(a0,b0,theti);
        xi = rei*cos(theti);
        yi = rei*sin(theti);
        SED82(i) = dU82func(a0,b0,w0n821,xi,yi);
    end
```

```matlab
figure
hold on
plot(thetv,SED82,'lineWidth',2);
xlabel('Angle in [Rad]');
ylabel('Strain Energy Density Delamination Boundary [J/m^3]');
title('SED around the delamination boundary at the offset 80/20');
```

Published with MATLAB® R2019a

Table of Contents

```
clear
```

Fatigue Analysis with Cyclic Data

```
%This code calculates the cyclic strain energy at an interval measured
 by
%the MTS machine. The cyclic strain energy is the loaded energy - the
%unloaded energy.
```

Load Data

```
load('Specimen4-Cyclic.mat')
cycles4 = Specimen4Cyclic.Cycle;                              %Loads
 the cycle number vector
displacement4 = abs(Specimen4Cyclic.AxialDisplacement);      %Loads
 the displacement vector [mm]
load4 = abs(Specimen4Cyclic.AxialForce);                     %Loads
 the force vector       [N]

load('Specimen17-Cyclic.mat')
cycles17 = Specimen17Cyclic.Cycle;
  %Loads the cycle number vector
displacement17 = abs(Specimen17Cyclic.AxialDisplacement);
  %Loads the displacement vector [mm]
load17 = abs(Specimen17Cyclic.AxialForce);
  %Loads the force vector       [N]

load('Specimen18-Cyclic.mat')
cycles18 = Specimen18Cyclic.Cycle;
  %Loads the cycle number vector
displacement18 = abs(Specimen18Cyclic.AxialDisplacement);
  %Loads the displacement vector [mm]
load18 = abs(Specimen18Cyclic.AxialForce);
  %Loads the force vector       [N]
```

Locate the different cycles that will be integrated

```
n4 = unique(cycles4);
   %Locates all the cycles that have been investigated
n4(isnan(n4)) = [];
   %Removes all the Nan-values from the unique matrix

n17 = unique(cycles17);
   %Locates all the cycles that have been investigated
n17(isnan(n17)) = [];
   %Removes all the Nan-values from the unique matrix

n18 = unique(cycles18);
   %Locates all the cycles that have been investigated
n18(isnan(n18)) = [];
   %Removes all the Nan-values from the unique matrix
```

Create Empty Strain Energy Vectors

```
U4 = zeros(1,length(n4));
   %Creates an empty Strain Energy Matrix [mJ]
U17 = zeros(1,length(n17));
   %Creates an empty Strain Energy Matrix [mJ]
U18 = zeros(1,length(n18));
   %Creates an empty Strain Energy Matrix [mJ]
```

Calculate the Cyclic Strain Energy

```
for i = 1:length(n4)
    Ucum = 0;
   %Empties the cumalitive Energy Matrix   [mJ]
    current = n4(i);
   %Searches for the current cycle data
    filt = cycles4 == current;
   %Logical vector that filters the current cyclic data
    Pcur = load4(filt);                                    %This
 Cycle's load vector           [N]
    dcur = displacement4(filt);                            %This
 Cycle's displacement vector    [mm]
    ncur = length(Pcur);
   %Obtains the amount of data points in this cycle
    for j = 1:(ncur-1)
        if rem(i,2) == 0
        Uj = Pcur(j)*(dcur(j+1)-dcur(j)) + (1/3)*((Pcur(j+1)*dcur(j+1))-
(Pcur(j)*dcur(j)));      %Integral that estimates the strain energy
 [mJ]
        else
        Uj = Pcur(j+1)*(dcur(j)-dcur(j+1)) + (1/3)*((Pcur(j)*dcur(j))-
(Pcur(j+1)*dcur(j+1)));      %Integral that estimates the strain energy
 [mJ]
```

```matlab
        end
        Ucum = Ucum + Uj;                              %Adds
 this step's data to the cumilative energy [mJ]
    end
    U4(i) = Ucum;                                    %Saves
 this cycle's strain energy [mJ]
end

for i = 1:length(n17)
    Ucum = 0;
  %Empties the cumalitive Energy Matrix   [mJ]
    current = n17(i);
  %Searches for the current cycle data
    filt = cycles17 == current;
  %Logical vector that filters the current cyclic data
    Pcur = load17(filt);                                  %This
 Cycle's load vector              [N]
    dcur = displacement17(filt);                          %This
 Cycle's displacement vector    [mm]
    ncur = length(Pcur);
  %Obtains the amount of data points in this cycle
    for j = 1:(ncur-1)
        if rem(i,2) == 0
        Uj = Pcur(j)*(dcur(j+1)-dcur(j)) + (1/3)*((Pcur(j+1)*dcur(j+1))-
(Pcur(j)*dcur(j)));     %Integral that estimates the strain energy
 [mJ]
        else
        Uj = Pcur(j+1)*(dcur(j)-dcur(j+1)) + (1/3)*((Pcur(j)*dcur(j))-
(Pcur(j+1)*dcur(j+1)));     %Integral that estimates the strain energy
 [mJ]
        end
        Ucum = Ucum + Uj;                              %Adds
 this step's data to the cumilative energy [mJ]
    end
    U17(i) = Ucum;
  %Saves this cycle's strain energy [mJ]
end

for i = 1:length(n18)
    Ucum = 0;
  %Empties the cumalitive Energy Matrix   [mJ]
    current = n18(i);
  %Searches for the current cycle data
    filt = cycles18 == current;
  %Logical vector that filters the current cyclic data
    Pcur = load18(filt);                                  %This
 Cycle's load vector              [N]
    dcur = displacement18(filt);                          %This
 Cycle's displacement vector    [mm]
    ncur = length(Pcur);
  %Obtains the amount of data points in this cycle
    for j = 1:(ncur-1)
        if rem(i,2) == 0
```

```matlab
        Uj = Pcur(j)*(dcur(j+1)-dcur(j)) + (1/3)*((Pcur(j+1)*dcur(j+1))-
(Pcur(j)*dcur(j)));       %Integral that estimates the strain energy
 [mJ]
      else
        Uj = Pcur(j+1)*(dcur(j)-dcur(j+1)) + (1/3)*((Pcur(j)*dcur(j))-
(Pcur(j+1)*dcur(j+1)));       %Integral that estimates the strain energy
 [mJ]
      end
      Ucum = Ucum + Uj;                                       %Adds
 this step's data to the cumilative energy [mJ]
    end
    U18(i) = Ucum;
  %Saves this cycle's strain energy [mJ]
end
```

Calculate the change in Strain Energy

```matlab
dU4 = zeros(1,length(U4)/2);
  %Creates an empty delta U vector [mJ]
dU17 = zeros(1,length(U17)/2);
  %Creates an empty delta U vector [mJ]
dU18 = zeros(1,length(U18)/2);
  %Creates an empty delta U vector [mJ]
for k = 1:length(dU4)
    l = k*2;
    dU4(k) = U4(l)-U4(l-1);
  %Calculates the change in Strain Energy (Load - Unload) [mJ]
end

%U17 has incomplete data! Will be compared with 18
for k = 1:length(dU17)
    l = k*2;
    dU17(k) = U17(l)-U17(l-1);
  %Calculates the change in Strain Energy (Load - Unload) [mJ]
end

for k = 1:length(dU18)
    l = k*2;
    dU18(k) = U18(l)-U18(l-1);
  %Calculates the change in Strain Energy (Load - Unload) [mJ]
end
```

Published with MATLAB® R2019a

Table of Contents

```
function [kv,phigv,phi0v,Av] =
 FatigueArea(SEDCrit,TableName,FrameStart,FrameEnd)
%This function calculates the delamination area measured through the
 SED
%Inputs:
%       -SEDCrit : The Critical Strain Energy Density Value [J/m^2]
%       -Tablename: The start of the name of the csv files as a string
%                   When you place your csv files in a different
 folder,
%                   add this to the name
%       -FrameStart: The first measured Frame number as an integer
%       -FrameEnd: The last measured Frame number as an integer
%Outputs:
%       -kv:    Vector with all the k-values [mm]
%       -phigv:  Vector with all the phig angles [rad]
%       -phi0v: Vector with all the phi0 angles [rad]
%       -Av:    Vector with all the area values [mm^2]
kv = zeros(1,(FrameEnd));    %Creates an emtpy vector for the k-values
phigv = zeros(1,(FrameEnd)); %Creates an emtpy vector for the phig-
values
phi0v = zeros(1,(FrameEnd)); %Creates an emtpy vector for the phi0-
values
Av = zeros(1,(FrameEnd));    %Creates an empty vector for the area
 values [mm^2]
for  i = FrameStart:FrameEnd
```

Read the Data

```
if i < 10
    char = "0" + i;
else
    char = i;
end
fullName = TableName + char + "_0.csv";
```

```matlab
T = readtable(fullName);                %Reads the table files
SED = T.StrainEnergyDensity_J_m_2_;      %Reads the Strain Energy
 Density of the current frame [J/m^2]
XFrame = T.X_mm_;                        %Reads the X-coordinates [mm]
YFrame = T.Y_mm_;                        %Reads the Y-coordinates [mm]
AngleFrame = T.Angle_rad_;               %Reads the angular coordinates
 [rad]
RadiusFrame = T.Radius_mm_;              %Reads the radii [mm]
```

Find the Center X/Y Coordinates

```matlab
X0 = mean(XFrame(~isnan(XFrame)));       %Removes the Nan values and
 calculates the mean x-coordinate [mm]
Y0 = mean(YFrame(~isnan(YFrame)));       %Removes the Nan values and
 calculates the mean y-coordinate [mm]
```

First Filter for Frame Data - SED Criterion

```matlab
filt = SED > SEDCrit;                    %Creates a logical array that
 will filter the data based on the SED-Criterion
X2 = XFrame(filt) - X0;                  %Filters the X-frame data and
 places the center at the center of the delamination [mm]
Y2 = YFrame(filt) - Y0;                  %Filters the Y-frame data and
 places the center at the center of the delamination [mm]
Phi2 = AngleFrame(filt);                 %Filters the angle data [rad]
Rho2 = RadiusFrame(filt);                %Filters the radii data [mm]
```

Find the current center delamination

```matlab
a = 1;
Rcur = max(Rho2(abs(X2)<a));
```

Second Filter for Frame Data - Symmetry Criterion 1

```matlab
%This step can be avoided if the angle phi is determined with phi =
%acos(x/r)
%Currently it is calculated with asin(y/r)
filt2 = X2 < abs(min(X2));               %Creates a logical array that
 will filter data based on Symmetry criterion
X3 = X2(filt2);                          %Final Filter that will be
 used for the X-frame [mm]
Y3 = Y2(filt2);                          %Final Filter that will be
 used for the X-frame [mm]
Phi3 = Phi2(filt2);                      %Final Filter that will be
 used for the X-frame [mm]
Rho3 = Rho2(filt2);                      %Final Filter that will be
 used for the X-frame [mm]
```

Third Filter for Frame Data - Symmetry Criterion 2

```
%This can easily filtered by only investigating the negative angles
 when
%phi = acos(x/r)
%Currently postive angles are investigated with phi = asin(x/r);
filt3 = Phi3 > 0;
Phi4 = Phi3(filt3);
Rho4 = Rho3(filt3);
```

Determining the k and phi g parameters

```
k = max(Rho4);                  %Finds the maximum extended radius of the
 delamiantion
phig = Phi4(Rho4 == k);         %Finds the angle phi g for the
 delamination model
```

Determining phi 0

```
b = 1;                          %Noise Factor
filt4 = Rho4 > Rcur*b;          %Removes all the measured points of the
 radius smaller than 30 mm (noise x-data ruin this measurement a
 little bit)
Phi5 = Phi4(filt4);
filt5 = Phi5 > (phig/2);        %Removes all the noise angles, which would
 imply a pure ellipse
Phi6 = Phi5(filt5);
phix = min(Phi6);               %Finds the angle at which the delamination
 width starts
phi0 = phig-phix;               %Determines the parameter phi0 that will
 be used for area determination
```

Calculating Area

```
A = Rcur*pi + (1/4)*k*phi0*(8*Rcur + 3*k);  %Calculation of current
 delamination area [mm^2]
```

Saving the data

```
kv(i) = k;
phigv(i) = phig;
phi0v(i) = phi0;
Av(i) = A;

end
end
```

Published with MATLAB® R2019a